Fracture Mechanics Prevention: Comprehensive Approach-based Modelling?

Mariana Kuffová[1], Pavel Nečas[2]

[1] Mechanical Engineering Department
Armed Forces Academy of General Milan Rastislav Stefanik
Demanova 393, 031 06 Liptovsky Mikulas 6, Slovakia
e-mail: mariana.kuffova@aos.sk

[2] Armed Forces Academy of General Milan Rastislav Stefanik
Vice-Rector for Science, Demanova 393, 031 06 Liptovsky Mikulas 6, Slovakia
e-mail: pavel.necas@aos.sk

Abstract: The paper presented focuses on fatigue crack growth observation in the microstructure of magnesium alloy AZ 91D using finite element software ADINA. ADINA offers a wide range of capabilities based on reliable and efficient finite element procedures. For this reason, ADINA is often chosen for applications where reliability and safety is of critical importance in different industries such as biomedical, automotive, nuclear, forming, civil engineering, hi-tech and others, e.g., in the dynamic analysis of bridge structures – earthquake analysis ,in biomedical applications, in the design of nuclear reactors or in studies on safety. This work shows efficiency and good correlation between experimental and numerical results and verifies this program for its utilization in the field of fatigue endurance determination and evaluation.

Keywords: microstructure; modelling and simulation; material fatigue; experiments; cracks and defects; reliability and personnel security

1 Introduction

The fatigue of metallic structural components is a widespread failure in different industrial branches. The fatigue process is very sensitive to a great amount of both external and internal factors that, with each of them on its own but especially when acting simultaneously, can affect the fatigue resistance of materials, parts and constructions. Fatigue tests can be performed in various experimental conditions at different loading frequencies. We have all come across examples of materials fatigue failure, whether it is the broken rail which caused trains to be delayed or the broken shaft which caused the car crash. The importance of fatigue is tied foremost to the safety of persons, whose lives depend on the reliability of a given device's operation.

Cracks initiate and propagate from pre-existing flaws, material defects, or design features (fatter holes or sharp corners). In fact, most fatigue is widespread, as hundreds or even thousands of cracks are manifested in cyclic loading. The net effect of numerous fatigue cracks located in the same general area is that they synergistically interact reducing the structure's residual strength. However, the single-crack concept is still important, because ultimately, catastrophic failure can occur when a single crack goes critical and in the process envelops other adjacent cracks in a zippering effect [1].

Two basic methods are employed to predict and determine potential fatigue locations. The first is a full-scale fatigue testing, which is performed during the development process. These tests are employed to ascertain what the expected durability is. Fatigue tests, in particular, are very expensive, since they are labour-intensive and require a lot of computer analysis. Decreasing expenses as well as increasing efficiency of mechanical design processes and providing operational lifetime durability of parts and machineries allow us to make progress in the field of the utilization of the computational technologies and the application of numerical methods when solving a huge amount of mechanical engineering praxes' problems. Nowadays we have several commercial programs at our disposal which allow us to solve the crack propagation. Many authors have dealt with influence of the crack growth on the functionality of the particular parts from global point of view. Available simulation programs for the simulation of fatigue crack growth can be generally divided into numerical and analytical ones. The numerical programs (FRANC/FAM, FRANC3D, ADAPCRACK3D, CRACK-TRACER, ZENCRACK) are able to predict the crack path in arbitrary 2-D or 3-D structures by using the finite element or boundary element method, the mesh-less method or the material point method. The lifetime is calculated mostly by using linear damage accumulation. However, they are often very time consuming. On the other hand, analytical programs (NASGRO, ESACRACK, AFGROW) are very fast because no model has to be built, no meshing has to be done and the analysis is very rapid. But in many cases the analytical solutions for a number of selected problems do not match the actual geometry and boundary conditions very well [1, 2, 3, 4]. ADINA is finite element software suitable for solving a large variety of problems. According to the available papers, this software has been used for static as well as dynamic analysis for instance, a composite material structure [5] and sealing ring [6] were analyzed. The composite structure was subjected to static pull conditions and stresses in the vicinity of quasi rigid inclusions, which were bonded into the base material, were investigated. The sealing ring was analyzed for undesired vibrations which occurred after it was subjected to pressure impulse load. ADINA is thus fully capable of solving fracture mechanics problems in general with large amount of options in stack under various loading conditions or thermal conditions utilizing a wide variety of material models. There is also the ability to model rupture criteria and thus it is possible to model material damage caused by cavities or impurities and its progression under cyclical load or under creep conditions. Our task was to verify

the FEM ADINA for fatigue crack growth observation and its correlation with experimental results.

Magnesium and its alloys are fascinating materials for practice. Magnesium's main advantage is its lowest specific weight out of every metal used for structural purposes, the declining availability and rising prices of raw materials, as well as the subsiding supply of metals in the world scale. The mechanical properties of pure magnesium are not favourable. It has low strength and ductility due to its crystalline structure. However, through alloying we can obtain important structural materials. Suitable alloying partially eliminates the occurrence of casting defects and considerably increases strength, toughness, resistance to corrosion and castability [7].

The outstanding features of commercially used magnesium alloys are their low specific weight, good castability, machinability and weldability in protective atmosphere. The drawbacks, which restrict their wider employment, are low modulus of elasticity, limited resistance to creeping at higher temperatures, high shrinkage during hardening and mainly by the low resistance to corrosion arising from their high chemical reactivity [8, 9].

2 Methodology of Simulation

Finite element software ADINA, which was used, offers two different numerical methods for the observation of the fatigue crack propagation: the line contour method and the virtual crack extension method. The model and simulation was in 2-D which is why we used the virtual crack extension method which is more suitable, efficient and easier because it uses only one analysis.

2.1 Virtual Crack Extension Method

The virtual crack extension method evaluates the J-integral for a given body using the difference of the total potential energy between two configurations with slightly different cracks. The basic idea is shown in Fig. 1. This method requires only one finite element analysis. The total potential energy variation is calculated using a "virtual material shift" (zone I in Fig. 1) obtained by shifting the nodes of a domain that includes at least one of the crack front nodes.

The equivalence between the J-integral and the ratio of the total potential energy variance to the crack area increases, but this only holds for linear elastic analysis and elasto-plastic analysis when the deformation theory of plasticity is applicable. In the following, the "energy release rate" refers to the ratio of the total potential energy variation to the crack area increase. The virtual crack extension method is used in ADINA to calculate the generalized expression of the energy release rate including the effects of thermal loads, pressure loads on the faces of the crack and inertia forces.

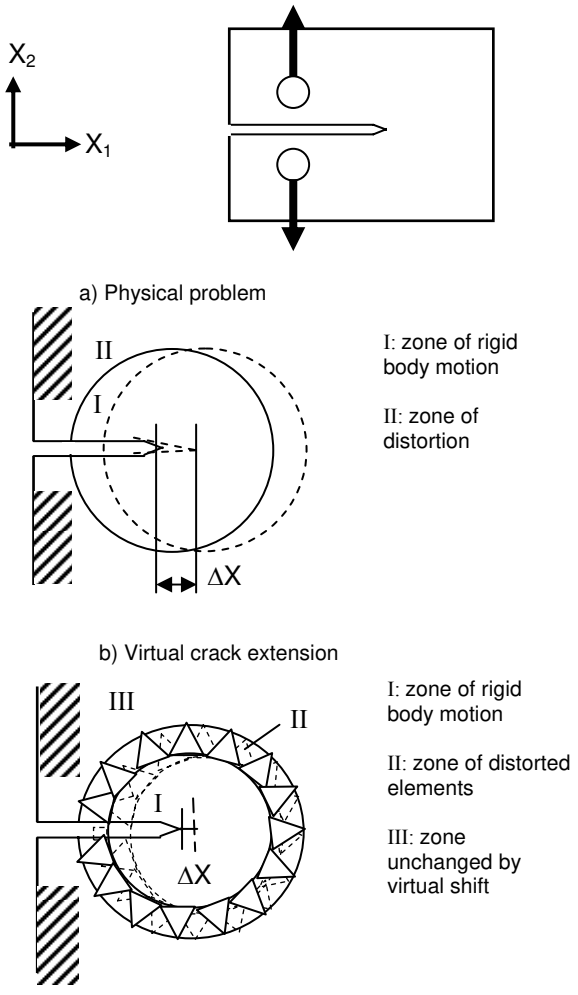

Figure 1

The virtual crack extension method in 2D analysis

According to Figure 1, the expression of the energy release rate is:

$$G = \frac{1}{A_c}\int_V \left(\left(\sigma_{ij}\frac{\delta u_j}{\delta x_k} - W\delta_{ik} \right)\frac{\delta \Delta X_k}{\delta x_j} - f_i \frac{\delta u_j}{x_j}\Delta X_j \right) dV - \frac{1}{A_c}\int_S t_i \frac{\delta u_i}{\delta x_j}\Delta X_j dS \text{ wit}$$

h: V- volume of the cracked body, S- surface of the cracked body, ΔX_k-components of virtual crack extension vector, A_c-increase in crack area, δ_{ij}-Kronecker delta, f_i-components of the body force vector, t_i-components of the surface traction vector, W- $\int_0^{\varepsilon_{ij}} \sigma_{ij} d\varepsilon_{ij}$.

Initial strains are included in the computation of the energy release rate.

2.1.1 Virtual Material Shift

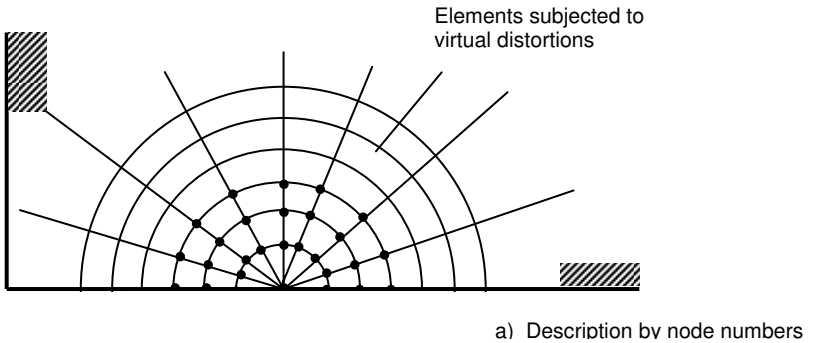

Figure 2
Description of the virtual material shift in ADINA

In order to describe a virtual material shift, a specified domain simply connected to the crack tip node must be selected (Fig. 2). The nodes inside this domain are subjected to a virtual shift in order to obtain the virtual configuration of the finite element mesh. In ADINA, each virtual shift domain can be described using node numbers, element numbers, or ring numbers (Fig. 2). It is important to verify that the virtual shift domains are simply connected. If a virtual shift domain does not contain at least one crack tip node, the fracture mechanics calculations are not performed. Several virtual shift domains can be defined simultaneously in one analysis. Only the distorted elements (zone II in Fig. 2), between the undeformed zone I and the rigid body motion zone III, contribute to the energy release rate. Therefore, the choice of the location of zone II in the finite element model will determine the accuracy of the result. It is recommended that several virtual material shifts of increasing size be used to evaluate the value of the energy release rate. Each virtual shift should enclose the next smaller virtual shift. The virtual shift size should increase equally in all directions from the plane perpendicular to the crack front.

A virtual vector is defined by its components in the global Cartesian system. An automatic calculation of the virtual vector can be requested for a given virtual material shift: in this case, the crack propagation area has been defined and the first two nodes on the generation line corresponding to the crack tip node associated with the virtual material shift are used to calculate the virtual vector. The length of the virtual vector is 1/100 of the length of the vector formed by the two nodes. It is recommended that this option be used when a crack propagation analysis is performed.

For a symmetric specimen and loading, the virtual vector lies in the plane of the crack. For an asymmetric specimen and/or loading, the virtual vector direction is usually unknown in advance, because the direction of future cracking is not usually in the plane of the crack [10].

3 Experimental Material

Magnesium alloy AZ 91D is the most commonly used magnesium alloy. Its main advantage is its lowest specific weight out of every metal used for structural purposes, and its good castability, machinability and weldability in a protective atmosphere. Drawbacks which restrict its wider employment are its low modulus of elasticity, its limited resistance to creeping at higher temperatures, its high shrinkage during hardening and, most of all, its low resistance to corrosion arising from their high chemical reactivity [10, 11]. The low specific weight and the ability to absorb vibrations make the alloys suitable for applications in the automobile, aviation and rocket industries as well as in telecommunication and instrumentation.

The mechanical properties are shown in Table 1 the microstructure and material curve are in Figs. 3 and 4.

Table 1
Mechanical properties of Mg – alloy AZ 91D

	Rm [MPa]	**A_5 [%]**	**Z [%]**	**$HB_{2.5/62.5/30}$**
AZ 91D	223	8.0	0.5	64.2

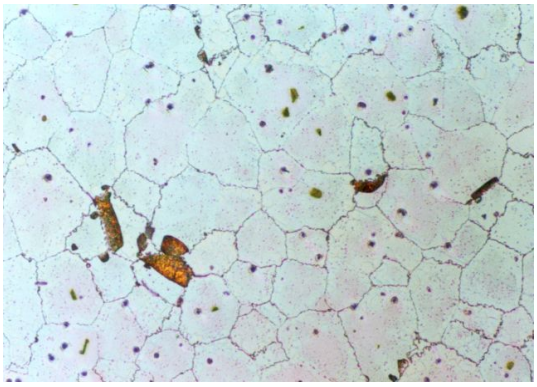

Figure 3
Microstructure of Mg – alloy AZ91D, mag. 100 x, etch. 5 %H_2MoO_4

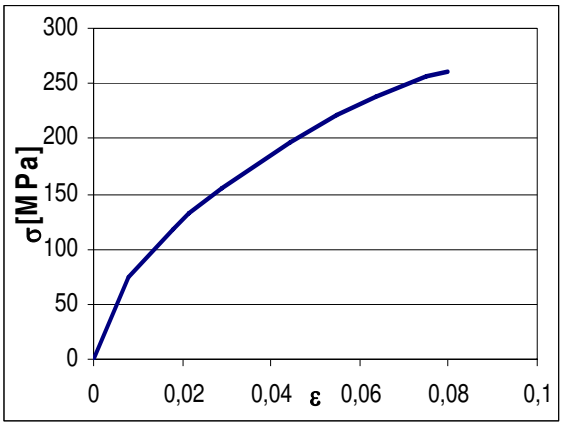

Figure 4
Resistance curve of AZ 91D

4 Numerical Part

The microstructure of the material represented by tightly packed grains was modelled by using the finite-element software ADINA in accordance with the microstructure shown in Fig. 3. The geometry of each grain was modelled by Pro/Engineer software and was exported as a plain surface in IGES file to ADINA, where a 2D analysis was performed. For the sake of analysis, each surface representing individual grain of the microstructure was discretised using a finite element mesh (Fig. 5). In this case quadratic elements were used, which means that unknown quantities have been approximated by a polynomial of the second order inside of each element. Due to large gradients in the secondary fields, it is necessary to use very fine discretisation in the vicinity of the crack to achieve reasonable accuracy. Each element has prescribed its own material properties. A multi-linear plastic material model was used in the simulation. The properties of the alloy were obtained experimentally as a dependence of the displacement of the specimen on the applied force. The values were then recalculated to a relation of strain ε and effective stress σ (Fig. 4) according to known dimensions of the specimen. Afterwards, the stress-strain curve was imported into ADINA and applied on each element. The analysis was performed by using large deformations and large displacements incorporated into the mathematical model.

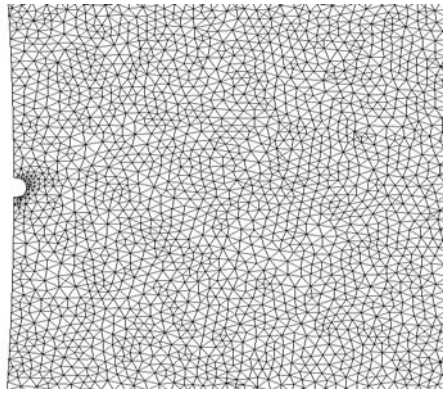

Figure 5
Mesh in the surrounding of the stress concentrator

Each grain was considered a standalone body and contact conditions between each pair of grains were implemented. In the microstructure model a stress concentrator was made (Fig. 6). On the boundaries, a cyclic load with amplitude 30 MPa and with frequency 25 Hz was applied, which was identical to experimental fatigue tests. These are standard loading conditions for examining the fatigue resistance of the material.

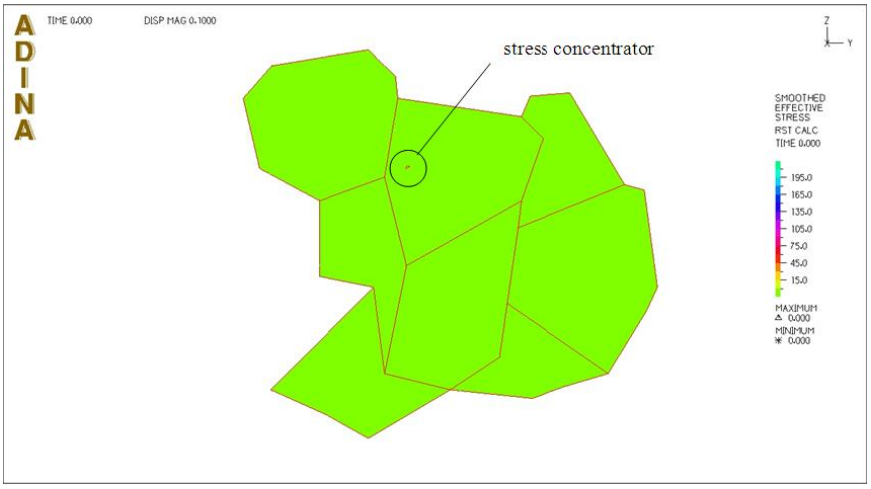

Figure 6

Model of microstructure with primary stress concentrator before applied load

A plastic zone (Fig. 7) is created in the vicinity of the crack tip in which a plastic strain is accumulated due to cyclic loading.

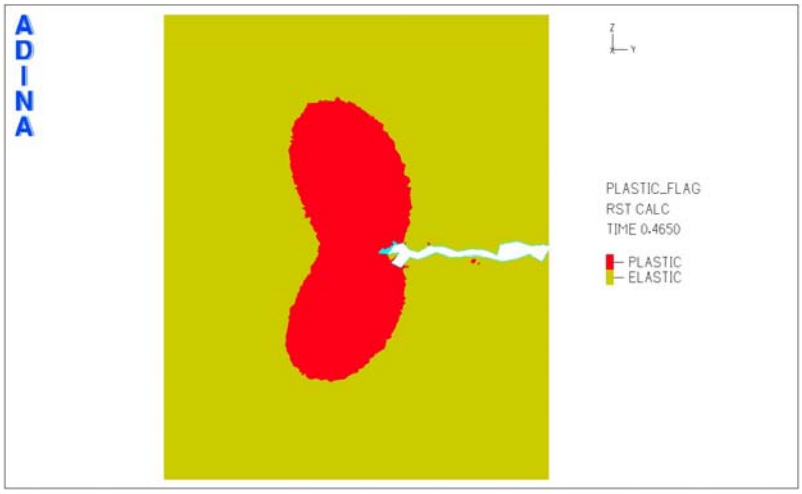

Figure 7

Plastic zone at the fatigue crack tip

The deformation process at the crack tip depends significantly on the mechanical properties of the material and on the environment in which the loading occurs. The limited plastic deformation, the equal values of intensity factor and the equal coefficients of asymmetry of the cycle do not guarantee the same magnitude and form of plastic zone ahead of the crack tip.

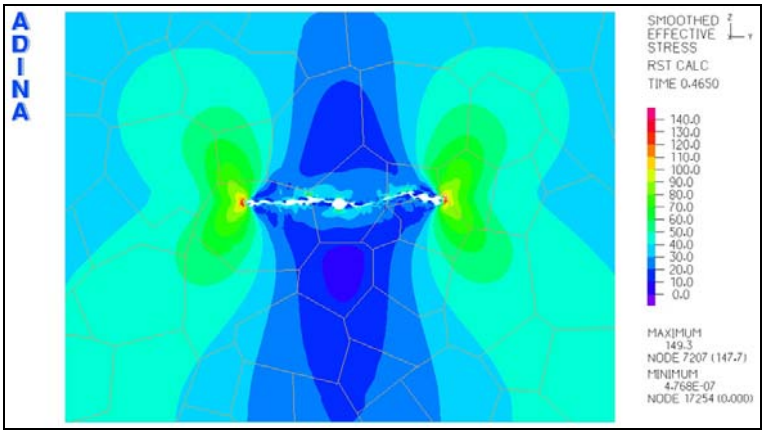

Figure 8
Fatigue crack path

The load amplitude by which the propagation of micro-failure occurs is fully dependent on the non-homogeneity of the material. The aim of the simulation was to observe the failure propagation in the microstructure (Fig. 8). A redistribution of stress was influenced by the cyclical nature of the applied load. Even though the stress is applied on the structure in a uniform manner, it does not act in the same way on each grain in the structure. Most of the stresses are cumulated in the region with certain non-homogeneity in the microstructure. In that case it was a notch and the highest stress was at the tip of crack.

5 Discussion of Results

Fatigue crack growth is generally divided into three regimes: near-threshold (stage I, low fatigue crack growth rate, single shear, large influence of structure, large influence of closured stress, the plastic zone at the fatigue crack tip is usually smaller than the average grain size), validity of the Paris law (stage II, medium fatigue crack growth rate, growing, little influence of structure, little influence of closured stress, the plastic zone at the fatigue crack tip is usually bigger than the average grain size) and rapid fatigue, when the crack increases its growth rate till final fracture. The first two areas are significant for the optimal selection of construction materials and for a qualified proposal of component and construction.

After a cyclic load was applied to the microstructure model, the crack started to grow at the stress concentrator. The formation of fatigue cracks always takes place at the free surface of cyclically loaded pieces, at points of concentration of cyclic plastic deformation. At these points one can find notches of different types and origin, as well as inclusion, precipitates and imperfections of the working surface. Fatigue cracks are formed due to the not -entirely -reversible plastic deformation.

The stress concentrator (Fig. 6) was artificially made and presented the inclusion or cast defect (Fig. 3). The structure of the material (Fig. 3) was classified as a structure with patchy polyedric grains of phase δ (grain size 1-2) and with areas of imperishable lamellar precipitate. Black points documented the occurrence of cast defects – cavities. These imperfections are considered to be stress concentrators.

The crack path in Fig. 8 is the result of a series of mechanisms associated with different stages of fatigue crack growth. The propagation started in a single grain and continued through several grains in stage I. A stage I crack growth, occurring predominantly by single slip bands (in the direction of maximum shear stress in front of the crack tip) in the direction of the primary slip system, developed because the local plastic zone (Fig. 7) became smaller than the average grain size. The crack is extraordinary effective stress and strain concentrator, together with the microstructural material parameters, the strain field at the crack tip control crack behaviour in a loaded body. The plastic zone (plastic deformed region of material at fatigue crack tip) differs markedly from the matrice structure. Its dimension is tens to hundreds of μm.

Under continuous cyclic loading, the primal crack became interconnected and penetrated deeply into the piece. Many micro-cracks grow only to a depth of several tens of microns and then stop. After the depth of penetration increased, the crack gradually inclined towards the direction perpendicular to the vector of the main stress, and a plastic zone appeared at the tip of the crack. The said processes could be aligned with the first stage of the propagation of the fatigue cracks, in which the crack spread in the crystallographic orientation. In the second stage, the crack spread in a non-crystallographic way. The length of the crack, corresponding to the transition from the first to the second stage of propagation, depended on the type of material and on the loading amplitude. The speed of propagation of the crack was low in the first stage, and the number of cycles necessary for its termination was small in comparison with the second stage of propagation of the crack. The first stage of the propagation of the cracks does not manifest itself for pieces with constructional, technological or metallurgical notches.

Then, the additional slip bands were activated and the crack grew in alternating glide planes perpendicular to the direction of maximum normal stress – stage II. Non-crystallographic propagation in the second stage was controlled by normal stress, while in both stages, at the usual temperatures of loading, the crack propagated in a trans-crystalline manner. The second stage of crack propagation terminates after having caused such a reduction of the carrying cross section of the piece that this would have failed by overloading.

The numerical simulation of fatigue crack growth in magnesium alloy AZ91D by ADINA was compared to experimental observation of fatigue crack trajectory (Fig. 9). Despite the elimination of the lamellar precipitate on the grain boundaries the primal fatigue crack grew transcrystalographicaly through the grains [12]. Both pictures (Figs. 8 and 9) show good correlation.

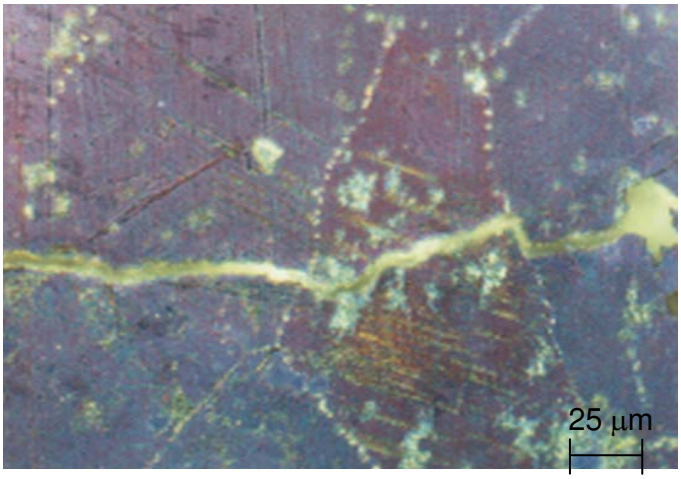

Figure 9
Transcrystallic growth of fatigue crack

Conclusions

The problems of crack propagation in the micro-scale are considerably demanding on the model accuracy. Many of the effects are manifested at the atomic scale and by using the continuum mechanics it is possible to study these effects only under the certain optimal conditions or according to the output of experimental results or other special methods.

The FEM software ADINA enables us to observe the growth of fatigue damage and crack propagation in a model as well as to observe the distribution of stress fields. It enables us to elaborate on the stress state inside of the material, based on which it is possible to predict the direction of crack propagation.

The aim of the paper was not only to simulate or model a fatigue process of a material to the final failure of the structure. Rather, the principle of the damage creation in micro-volume should be observed closely, as well as the influence of stress distribution on the fatigue crack propagation. It can be seen that even for small loads, small micro-cracks and micro-damage can be spread in the micro-structure, which causes changes inside the material. This, of course, does not necessarily mean that it will lead to a final crack which will imminently cause a failure. The direction of the crack propagation is highly dependent on the stress distribution in the structure and vice versa, which means that the crack propagation, its direction and its peed are governed by the principle of the minimum energy in the system.

References

[1] Carpenter, M.: Managing the Fleet: Materials Degradation and its Effect on Aging Aircraft. AMPTIAC, 5 (2001), No. 4, pp. 1-20

[2] Charoenphan, S., Plesha, M. E., Bank, L. C.: Simulation of Crack Growth in Composite Material Shell Structures. Int. J. Numer. Meth. Engng, 60 (2004), pp. 2399-2417

[3] Ural, A., Wawrzynek, P. A., Ingraffea, A. R.: Simulating Fatigue Crack Growth in Spiral Bevel Pinion NASA Glenn Research Center: Cleveland OH, 2003

[4] Nguyen, O., Repetto, E.A., Ortiz, M., Radovitzky, R. A.: A Cohesive Model of Fatigue Crack Growth. Int. Journal of Fracture 110 (2001), pp. 351-369

[5] Štiavnický, M., Kápolka, P.: Modelling of Polymer Composites Reinforced by Carbon Nano Tubes, in Proceedings of 23rd Danubia-Adria Symposium on Experimental Methods in Solid Mechanics, Podbanské, Slovak Republic, September 26-29, 2006, pp. 35-39

[6] Štiavnický, M., Kápolka, P.: The Static and Dynamic Analysis of the Sealing Ring, in Proceedings of 8th intern. Conference Armament and Technics of Ground Forces, Liptovský Mikuláš, Slovakia, November 30, 2005, pp. 135-140

[7] Ptáček, L.: Structure and Technological Properties of Magnesium Alloy AZ80. In Proceedings of 5th Intern. Metalog. Symposium METSYMPO 1999, Rajecké Teplice, Slovakia, 1999, p. 53

[8] Mrva, P., Kottfer, D.: Influence of Thermal Spray Coatings on the Thermal Endurance of Magnesium Alloy ML-5. Acta Polytechnica Hungarica 6 (2009) No. 2, pp. 71-75, ISSN 1785-8860

[9] Kottfer, D., Pešek, L., Mrva, P., Zubko, P.: Hardness Evaluation of a Tungsten Film Deposited by Plasma Enhanced CVD Technique. Acta Metallurgica Slovaca 10 (2004), No. 1, pp. 630-634, ISSN 1335-1532

[10] ADINA Verification Manual, report ARD 06-10, ADINA R&D, Inc., 2006

[11] Ptáček, L., Ustohal, V.: Magnesium Alloys and Their Applications. In Proceedings Metal 98, Ostrava, Czech Republic, 1998, p. 45

[12] Kuffová, M.: Fatigue Crack Growth in Construction Materials of Air Transportation. In Proceedings of 7th Inter. Scient. Conference New Development Trends in Aeronautics. Košice, Slovakia, September 6-8, 2006

Unicast Position-based Routing Protocols for Ad-Hoc Networks

Miss Laiha Mat Kiah

Department of Computer System and Technology
Faculty of Computer Science and Information Technology
University of Malaya
50603 Kuala Lumpur, Malaysia
misslaiha@um.edu.my

Liana Khamis Qabajeh

Faculty of Computer Science and Information Technology, University of Malaya,
58200 Kuala Lumpur, Malaysia
liana_tamimi@ppu.edu

Mohammad Moustafa Qabajeh

Department of Electrical and Computer Engineering, IIUM
58200 Kuala Lumpur, Malaysia
m_qabajeh@yahoo.com

Abstract: Wireless Ad-Hoc networks are collections of nodes that communicate without any fixed infrastructure. A critical problem in Ad-Hoc networks is finding an efficient and correct route between a source and a destination. The need for scalable and efficient protocols, along with the recent availability of small, inexpensive low-power positioning instruments justify adopting position-based routing protocols in mobile Ad-Hoc networks. This paper presents an overview of the existing Ad-Hoc routing protocols that make forwarding decisions based on the geographical position of a packet's destination. We also outline the main problems for this class of routing protocols. We conclude our findings by discussing opportunities for future research.

Keywords: position-based routing; location-aware routing; ad-hoc networks; wireless networks; routing protocols

1 Introduction

Ad-Hoc wireless networks are self-organizing multi-hop wireless networks, where all the nodes take part in the process of forwarding packets. Ad-Hoc networks can quickly and inexpensively be set up as needed since they do not require any fixed infrastructure, such as base stations or routers. Therefore, they are highly applicable in many fields such as emergency deployments and community networking.

The function of a routing protocol in Ad-Hoc network is to establish routes between different nodes. Ad-Hoc routing protocols are difficult to design in general. There are two main reasons for this: the highly dynamic nature of these networks due to the high mobility of the nodes, and the need to operate efficiently with limited resources, such as network bandwidth and the limited memory and battery power of the individual nodes in the network. Moreover, routing protocols in Ad-Hoc networks, unlike static networks, do not scale well due to frequently changing network topology, lack of predefined infrastructure like routers, peer-to-peer mode of communication and limited radio communication range [20].

For the aforementioned reasons, many routing protocols which are compatible with the characteristics of Ad-Hoc networks have been proposed. In general, they can be divided into two main categories: *topology-based* and *position-based*. *Topology-based* routing protocols use information about links that exist in the network to perform packet forwarding. In general, topology-based routing protocols are considered not to scale in networks with more than several hundred nodes [23].

In recent developments, *position-based* routing protocols exhibit better scalability, performance and robustness against frequent topological changes [20], [23]. Position-based routing protocols use the geographical position of nodes to make routing decisions, which results in improved efficiency and performance. These protocols require that a node be able to obtain its own geographical position and the geographical position of the destination. Generally, this information is obtained via *Global Positioning System (GPS)* and location services. The routing decision at each node is then based on the destination's position contained in the packet and the position of the forwarding node's neighbors. So the packets are delivered to the nodes in a given geographic region in a natural way. There are different kinds of position-based protocols which are categorized into three main groups: *restricted directional flooding*, *greedy* and *hierarchical routing protocols* [13] (to be discussed in *Section 2*).

This survey (which is an extended version of our work in [11]) gives an overview of a large percentage of existing unicast position-based routing protocols for mobile Ad-Hoc networks. We outlined the main problems which must be solved for this class of routing protocols and presented the solutions that are currently available. The discussed protocols are also compared with respect to the used

location service, the used forwarding strategy, tolerability to position inaccuracy, robustness, implementation complexity, scalability, packet overhead, guaranteeing loop-freedom, probability of finding the shortest path and the suitable network density to be implemented in.

The protocols that have been selected for analysis are *MFR* [7], *DIR* [4], *GPSR* [1], *ARP* [20], *I-PBBLR* [23], *POSANT* [18], *DREAM* [15], *LAR* [24], *LARWB* [17], *MLAR* [19], *GRID* [21], *TERMINODES* [9] and *LABAR* [6]. It is worth nothing that many other position-based routing protocols exist for mobile Ad-Hoc networks; however, we have selected what we regard as representative for the existing approaches.

The rest of the paper is organized as follows. *Section 2* presents the basic idea and principles of position-based addressing and routing. *Section 3* gives an overview of the selected position-based routing protocols. *Section 4* outlines the differences between the discussed protocols. Directions for future research are discussed in *Section 5*. Finally, we conclude the paper in *Section 6*.

2 Basic Principles of Position-based Routing

The main prerequisite for position-based routing is that a sender can obtain the current position of the destination. Typically, a location service is responsible for this task. Existing location services can be classified according to how many nodes host the service. This can be either some specific nodes or all nodes of the network. Furthermore, each location server may maintain the position of some specific or all nodes in the network. The four possible combinations can be abbreviated as some-for-some, some-for-all, all-for-some and all-for-all [13].

There are three main packet-forwarding strategies used for position-based protocols: *greedy forwarding*, *restricted directional flooding* and *hierarchical* approaches. While their main objective is to utilize available position information in the Ad-Hoc routing, their means of achieving this are quite different. Most position-based protocols use *greedy forwarding* to route packets from a source to the destination. Greedy protocols do not establish and maintain paths from source to the destination; instead, a source node includes the approximate position of the recipient in the data packet and selects the next hop depending on the optimization criteria of the algorithm; the closest neighbor to the destination for example [13], [20]. Similarly, each intermediate node selects a next hop node until the packet reaches the destination. In order for the nodes to be able to do so, they periodically broadcast small packets (called beacons) to announce their position and enable other nodes to maintain a one-hop neighbor table. Such an approach is scalable and resilient to topology changes since it does not need routing discovery and maintenance; however, periodic beaconing creates a lot of congestion in the network and consumes the nodes' energy [23].

While the beaconing frequency can be adapted to the degree of mobility, a fundamental problem of inaccurate (outdated) position information is always present: a neighbor selected as a next hop may no longer be in transmission range. This leads to a significant decrease in the packet delivery rate with increasing node mobility. To reduce the inaccuracy of position information, it is possible to increase the beaconing frequency. However, this also increases the load on the network by creating a lot of congestion, increasing the probability of collision with data packets and the energy consumption of the nodes.

Unfortunately, greedy routing may not always find the optimal route, and it may even fail to find a path between source and destination when one exists [13]. An example of this problem is shown in Figure 1. Note that there is a valid path from *S* to *D*. The problem here is that *S* is closer to the destination *D* than any of the nodes in its transmission range; therefore greedy forwarding will reach a local maximum from which it cannot recover. Generally, greedy forwarding works well in dense networks, but in sparse ones it fails due to voids (regions without nodes) [20].

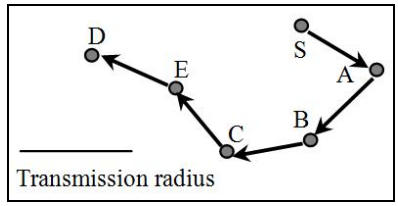

Figure 1
An example of greedy routing failure

In *restricted directional flooding,* the sender will broadcast the packet (whether the data or route request packet) to all single hop neighbors towards the destination. The node which receives the packet checks whether it is within the set of nodes that should forward the packet (according to the used criteria). If yes, it will retransmit the packet. Otherwise the packet will be dropped. In restricted directional flooding, instead of selecting a single node as the next hop, several nodes participate in forwarding the packet in order to increase the probability of finding the shortest path and be robust against the failure of individual nodes and position inaccuracy.

The third forwarding strategy is to form a *hierarchy* in order to scale to a large number of mobile nodes. Some strategies combine nodes' locations and hierarchical network structures by using zone-based routing such as *LABAR*. Others use dominating set routing such as *GRID*. Some others, such as *TERMINODES*, present a two-level hierarchy within them; if the destination is close to the sender, packets will be routed based on a proactive distance vector. Greedy routing is used in longer distances; therefore, these approaches have characteristics similar to those of greedy forwarding.

3 Overview of Selected Position-based Routing Protocols

In this section the selected protocols are described. For each protocol, we tried to summarize its main objectives, how it works and its advantages and disadvantages compared to other protocols. *Subsection 3.1* discusses greedy forwarding protocols, *Subsection 3.2* talks about restricted directional flooding ones and *Subsection 3.3* tackles hierarchical approaches. In the discussion part of each protocol, the following evaluation criteria have been taken into consideration:

- Location service type: indicates the type of the location service used with the given protocol; i.e., it shows how many nodes participate in providing location information and for how many other nodes each of these nodes maintains location information.
- Location service robustness: it is considered to be low, medium or high depending on whether the position of a given node will be inaccessible upon the failure of a single node, the failure of a small subset of the nodes or the failure of all nodes, respectively.
- Forwarding strategy type: describes the fundamental strategy used for packet forwarding.
- Forwarding strategy toleration to position inaccuracy: forwarding strategies tolerate different degrees of inaccuracy of the destination's position. This is reflected by the toleration to position inaccuracy criterion.
- Forwarding strategy robustness: the robustness of an approach is considered to be high if the failure (or absence due to mobility) of a single intermediate node does not prevent the packet from reaching its destination. It is medium if the failure of a single intermediate node might lead to the loss of the packet but does not require the set up of a new route. Finally, robustness is low if the failure of an individual node might result in packet loss and the setting up of a new route. According to this definition, the routing protocols that begin data transmission immediately without the need for routing setup have at least medium robustness.
- Forwarding strategy implementation complexity: describes how complex it is to implement and test a given forwarding strategy. This measure is highly subjective and we will explain our opinion while discussing each protocol.
- Forwarding strategy scalability: describes the performance of the protocol with an increasing number of nodes in the network. It can be classified as follows: high scalability is used when a network grows as much as it needs and the approach is still able to maintain a good performance. Medium scalability means that an approach can handle networks with a reasonable size, but may have problems if it grows. Low scalability describes protocols which are

restricted to small networks. Since all the position-based routing protocols are scalable compared to topology-based ones, all the discussed protocols have at least medium scalability.

- Forwarding strategy packet overhead: refers to bandwidth consumption due to a higher number of signaling packets. The packets' sizes were not taken into consideration since all the discussed protocols are considered to have small packets, compared to secure protocols for example. Note that position-based routing protocols have lower packet overhead compared to topology-based ones. Hence all the discussed protocols have at most medium packet overhead.
- Loop-freedom: any routing protocol should be inherently loop-free to preserve the network resources and guarantee the correct operation of the protocol. Therefore, the discussed protocols are classified as having or not having loop-freedom property.
- Optimal path: this is used to indicate the probability that the protocol will find and use the shortest path for data packet relay.
- Density: indicates whether the protocol is more suitable to be implemented in dense or/and sparse networks.

3.1 Greedy Forwarding Protocols

This section discusses selected greedy forwarding routing protocols. The discussed protocols are *MFR* [7], *DIR* [4], *GPSR* [1], *ARP* [20], *I-PBBLR* [23] and *POSANT* [18].

3.1.1 MFR

Some greedy position-based routing protocols, as *Most Forward within distance R (MFR)* [7], try to minimize the number of hops by selecting the node with the largest progress from the neighbors, where progress is defined as the projection of the distance of the next hop from the sender on the straight line between the sender and the destination [7]. In Figure 2, if *MFR* is used, the source *S* will choose node *A* as the next hop since it has the largest progress to the destination *D*.

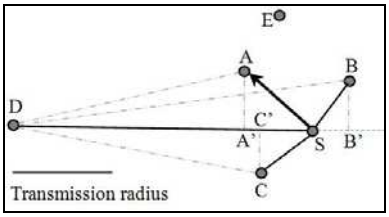

Figure 2
MFR example

MFR has the shortcomings of either not guaranteeing to find a path to the destination or finding a path which is much longer than the shortest path. Moreover, nodes periodically should broadcast beacons to announce their positions and enable other nodes to maintain a one-hop neighbor table.

MFR is the only progress-based algorithm competitive in terms of hop count [16]. However, choosing the node with the largest progress as the next hop will increase the probability that the two nodes will disconnect from each other before the packet reaches the next hop. So the packet drop rate increases greatly, especially in highly mobile environments. Such a situation is very common due to neighbor table inconsistency [20].

Discussion

As other greedy forwarding protocols, all nodes in *MFR* maintain a one-hop neighbor table; i.e., *MFR* uses all-for-some location service. Hence, a given node will be inaccessible upon the failure of a subset of the nodes; its location service has medium robustness. However, the technique used to enable the source knows the position of the destination is not discussed. Greedy forwarding is both efficient and very well suited for use in Ad-Hoc networks with a highly dynamic topology [13]. However, one important drawback of current greedy approaches is that the position of the destination needs to be known with an accuracy of a one-hop transmission range, otherwise the packets cannot be delivered [13].

MFR robustness is medium since the failure of an individual node may cause the loss of a packet in transit, but it does not require setting up a new route, as would be the case in topology-based Ad-Hoc routing. Such an approach is very easy to implement and scalable since it does not need routing discovery and maintenance [22]. Moreover, it has a low packet overhead due to its small number of small-size packets.

MFR is probed to be a loop-free algorithm [8] since it always forces a message to make a step closer to the destination. Generally, greedy routing may not always find the optimum route and it may even fail to find a path between the source and destination when one exists [22]; the probability of finding the optimal path is considered as medium. Finally, all basic distance, progress and direction based methods such as *MFR* and *DIR* have high delivery rates in dense graphs, and low delivery rates in sparse ones [16].

3.1.2 DIR

Compass routing algorithms, such as *DIR* [4], try to minimize the spatial distance that a packet travels and are based on forwarding the packet to the neighboring node that minimizes the angle between itself, the previous node and the destination [13]. The source or intermediate node A uses the location information of the destination D to calculate its direction. Then the message m is forwarded to the neighbor C, such that the direction AC is closest to the direction AD. This

process is repeated until the destination is, eventually, reached [16]. Consider the network in Figure 3, where the transmission radius is as indicated in the figure. The direction *AC* is closest to direction *AD* among candidate directions *AS*, *AB*, *AC*, *AG* and *AF*. So the path selected by *DIR* method is *SACD*.

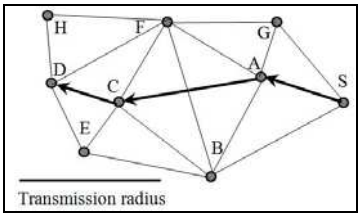

Figure 3
DIR example

As a greedy protocol, *DIR* suffers from congestion created by frequent beaconing, and it may not always find the optimum route, and it may even fail to find a path between source and destination if it exists.

The *DIR* method, and any other method that includes forwarding the message to the neighbor with closest direction, such as *DREAM* [15], are not loop-free, as is shown in [8] using the counterexample in Figure 4. The loop consists of four nodes denoted *S*, *B*, *C* and *A*. The transmission radius is as indicated in the figure. Let the source be any node in the loop, e.g. *S*. Node *S* selects node *B* to forward the message, because the direction of *B* is closer to destination *D* than the direction of its other neighbor *A*. Similarly, node *B* selects *C*, node *C* selects *A* and node *A* selects *S*.

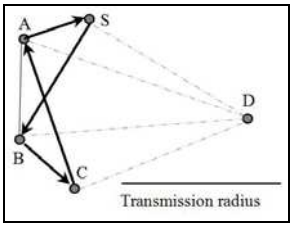

Figure 4
A loop in the directional routing

Discussion

As a greedy forwarding protocol, *DIR* has the same criteria as *MFR* except that *DIR* and any other method that includes forwarding the message to the neighbor with closest direction, such as *DREAM*, are not loop-free.

3.1.3 GPSR

Nearly Stateless Routing with Guaranteed Delivery are schemes where nodes maintain only some local information to perform routing. The face routing and *Greedy-Face-Greedy (GFG)* schemes were described in [14]. In order to ensure message delivery, the face routing (called *perimeter* algorithm in [1]) constructs a planar and connected so-called Gabriel subgraph of the unit graph, and then applies routing along the faces of the subgraph (e.g. by using the right hand rule) that intersect the line between the source and the destination. If a face is traversed using the right hand rule then a loop will be created; since a face will never exist. Forwarding in the right hand rule is performed using the directional approach. To improve the efficiency of the algorithm in terms of routing performance, face routing can be combined with algorithms that usually find shorter routes, such as the greedy algorithm to yield *GFG* algorithm [14]. Routing is mainly greedy, but if a mobile host fails to find a neighbor closer than itself to the destination, it switches the message from 'greedy' state to 'face' state [13].

Authors in [1] transformed *GFG* algorithm into *Greedy Perimeter Stateless Routing (GPSR)* protocol by including IEEE 802.11 medium access control scheme. The perimeter routing strategy of the *GPSR* is based on planar graph traversal and is proposed to address the local maximum problem of greedy forwarding [8]. It is performed on a per-packet basis and does not require the nodes to store any additional information. A packet enters the recovery mode when it arrives at a local maximum. It returns to greedy mode when it reaches a node closer to the destination than the node where the packet entered the recovery mode [13]. *GPSR* guarantees that a path will be found from the source to the destination if there exists at least one such path in the original non-planar graph [13].

In [1] *GPSR* was experimented and compared with the non-position based protocol, *Dynamic Source Routing (DSR)* [3]. *GPSR* protocol consistently delivered over 94% of the data packets successfully; it is competitive with *DSR* in 50 node networks, and increasingly more successful than *DSR* as the number of nodes increases. The routing protocol traffic generated by *GPSR* was constant as mobility increased, while *DSR* must query longer routes with longer diameter and do so more often as mobility increases. Thus, *DSR* generates drastically more routing protocol traffic in simulations with over 100 nodes [1]. Therefore, the scalability seems to be the major advantage of this class of algorithms over source-based protocols. However, these simulations did not include the traffic and the time required to look up the position of the destination. It was also assumed that the position of the destination is accurately known by the sender [13].

Nearly stateless schemes are likely to fail if there is some instability in the transmission ranges of the mobile hosts, when the network graph includes nodes with irregular transmission ranges [18]. Transmission range instability means that the area a mobile host can reach is not necessarily a disk. This unstable situation

occurs if there are obstacles (e.g. buildings, bad weather) that disrupt the radio transmission [16]. In *GPSR*, as with other greedy forwarding protocols, periodic beaconing creates lot of congestion in the network and consumes nodes' energy. In addition, *GPSR* uses link-layer feedback from *Media Access Control (MAC)* layer to route packets; such feedbacks are not available in most of the *MAC* layer protocols [20]. Finally, planarizing the underlying graph is computationally expensive and requires up-to-date neighborhood information [20].

Discussion

GPSR exhibits all the properties of greedy forwarding except that its implementation effort is considered to be of medium complexity due to planarizing underlying network and using perimeter routing. On the other hand, using the right hand thumb rule and perimeter mode routing made it applicable in sparse networks as well as dense ones.

3.1.4 ARP

Another scalable position-based routing protocol is *Angular Routing protocol (ARP)* [20]. In *ARP*, nodes emit a hello packet on a need-basis (non-periodic) at a rate proportional to their speeds. These hello packets enable each node to maintain a one hop neighbor table. *ARP* uses geographic forwarding to route packets to the destination. If geographic forwarding fails, an angle-based forwarding scheme is used to circumvent voids in sparse networks. *ARP* does not need any link-layer feedbacks like *GPSR*. If a source wants to send a packet to a specific destination, it selects as the next hop the node among its neighbors geographically closest to the destination. Each intermediate node follows this next hop selection criterion. Thus, at each hop the packet progresses towards the destination by a distance $\leq 0.9\ R$, where R is the radio range of the node. This is done to avoid the problem of leaving the next hop node out from the transmission range of the current node.

If no node is closer to the destination than the source node, or any intermediate node, then the node selects a neighboring node that creates a minimum angle, among available neighbors. Figure 5 shows the angle-based forwarding to circumvent voids. The intermediate node *B* has no neighbors closer to the destination *D* than itself. In such a situation *B* selects a next hop that forms a minimum angle towards destination; i.e., node *C*.

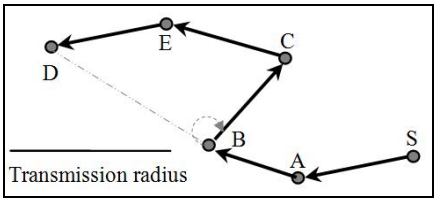

Figure 5
Angle-based forwarding to circumvent voids in *ARP*

After selecting a next hop node, the intermediate node appends its ID to the packet header. For each data packet, the *ARP* header memorizes a maximum of *k* last visited hops in order to avoid selecting a next-hop whose ID presents in the *ARP* header. This memorization technique helps *ARP* avoid local loops but does not guarantee its loop freedom. It is clear that assigning *k* a small value will decrease the percentage of local loops avoided. On the other hand, assigning it a large value will enlarge the size of the packet, which in turn will increase the packet overhead.

The simulations in [20] showed that *ARP* is scalable and achieves a high packet delivery rate while incurring low overhead compared to *GPSR*. Emitting hello packets on a need-basis reduces the problems associated with beaconing. Also, using the angle-based forwarding to circumvent voids increases the probability of finding a path (not necessarily the optimal one) in sparse networks.

Discussion

ARP exhibits all the properties of greedy forwarding except that by memorizing the last visited hops in the packet header it avoids local loops; however, this does not guarantee its loop freedom. Moreover, its use of an angle-based forwarding scheme to circumvent voids makes it applicable in sparse networks as well as dense ones.

3.1.5 I-PBBLR

Most position-based routing protocols use forwarding strategies based on distance, progress or direction. *Improved Progress Position Based BeaconLess Routing algorithm (I-PBBLR)* [23] combines the traditional progress with the direction metric to form the improved progress definition. There are many methods to combine the progress with direction, such as weighted addition and simple multiplication. The authors have chosen the cosine of the angle since its value is between 0 and 1, and it is even. If the traditional progress is multiplied by the cosine of the angle, both the minimum and maximum of the progress are not changed. It also satisfies the need that the node with a smaller angle will forward packet earlier. Finally, they guarantee loop freedom as the packets are always forwarded a step closer to the destination.

I-PBBLR tries to eliminate the beaconing drawbacks by using a beaconless protocol. In beaconless protocols, the sender makes non-deterministic routing decisions allowing opportune receiving nodes to determine a packet's next-hop through contention at transmission time. In *I-PBBLR*, if a source node has a data packet to send, it first determines the position of the destination, stores these geographical coordinates along with its own current position in the header of the packet, and broadcasts the packet to all neighboring nodes (since it does not possess knowledge of neighboring nodes' positions).

Nodes located within the forwarding area of the relaying node apply *Dynamic Forwarding Delay (DFD)* prior to relaying the packet, whereas nodes outside this

area drop the received packet. The value of the *DFD* depends on the relative position coordinates of the current, previous and destination nodes. Eventually, the node that computes the shortest *DFD* forwards the packet first by broadcasting it to all neighboring nodes after replacing the previous node's position in the header with its own current position. Every node in the forwarding area detects the further relaying of the packet and cancels its scheduled transmission of the same packet. This mechanism allows selecting one neighbor as the next hop in a completely distributed manner, without having knowledge of the neighboring nodes, which is achieved by applying the concept of *DFD*. The simulation results showed that position-based beaconless routing using the improved progress reduced the overhead and increased the delivery rate by 3-5% compared with using the traditional progress.

Discussion

I-PBBLR inherited all the properties of greedy forwarding; however, the used location service was not discussed at all. Moreover, using a beaconless protocol slightly increases the robustness and scalability, reduces the packet overhead, improves the performance in sparse networks and increases tolerability to position inaccuracy compared to traditional greedy protocols. Finally, using the improved progress guarantees loop freedom as the packet is always forwarded a step towards the destination.

3.1.6 POSANT

Some position-based routing algorithms, such as *GPSR*, fail to find a route from a source to a destination (or they find a route that is much longer than the shortest path) when the network contains nodes with irregular transmission ranges. On the other hand, routing algorithms based on *Ant Colony Optimization (ACO)* guarantee message delivery and converge on a route which is very close to the optimal route even if the network contains nodes with different transmission ranges. However, *ACO* algorithms use a large number of messages and need a long time before the routes are established. *POSition-based ANT colony routing Algorithm for mobile Ad-Hoc networks (POSANT)* [18] is a reactive routing algorithm which is based on *ACO* and uses information about the location of nodes in order to reduce the route establishment time while keeping the number of generated ants smaller in comparison to other ant-colony-based routing algorithms.

In *POSANT*, to establish a route from a source node *S* to a destination node *D*, neighbors of *S* are partitioned into 3 zones as shown in Figure 6. After that, *S* launches *n* forward ants with unique sequence numbers from each zone at regular time intervals. *POSANT* assumes that each node maintains a table of the values of pheromone trails assigned to its outgoing links for different destinations. Upon receiving a packet for a specific destination, a node will check if there is at least one pheromone trail for that destination; this pheromone trail will be used for

making a stochastic decision to select the next hop. If no such pheromone trail exists, a pheromone trail is initialized to each outgoing link. The amount of the deposited pheromone on each link depends on the zone of the corresponding neighbor. The motivation is that in most cases a shortest route passes through the nodes which are closer to the direction of the destination.

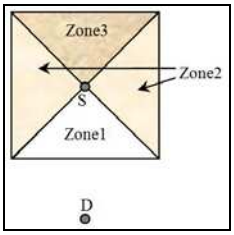

Figure 6
Different zones of *S* for destination node *D*

Whenever a forward ant enters a node from one of its neighbors, the identifier of the neighbor, the sequence number of the ant and the identifier of the destination will be stored. Repeated forward ants will be destroyed. When a forward ant reaches the destination, it is destroyed and a backward ant with the same sequence number is sent back to the source. Moving from node *B* to node *A*, the backward ant increases the amount of pheromone stored in edge *AB*. An evaporation process causes the amount of pheromone deposited in each link to decrease with time.

The above stochastic strategy establishes multiple paths between the source and destination. As a result, *POSANT* is a multipath routing algorithm. Multipath routing reduces the chance of congestion in the network; on the other hand, they can lead to out-of-order packet delivery problems.

Consider if a node *A* realizes that the link to *B* is broken and there is a pheromone trail corresponding to link *AB* for *D* in the pheromone table of *A*. In this case the stochastic data routing will continue, but if there is no pheromone trail for *D* in any of the other outgoing links of *A*, *A* sends a message to its neighbors to inform them that there is no route to *D* from *A*. Upon receiving this message, these neighbors do the same as if the link to *A* is broken. If the only outgoing link of the source node that has a pheromone trail for *D* breaks or a message from this link is received that states there is no route to *D*, a new route establishment process will begin and sending data packets will be suspended until a new route is found. Simulations in [18] showed that *POSANT* has a shorter route establishment time while using a smaller number of control messages than other ant colony routing algorithms.

Discussion

In *POSANT*, the used location service was not discussed. However, the used forwarding strategy is multiple greedy forwarding with the pheromone trail value

used as the optimization criteria; a source launches many forward ants from different zones at regular time intervals and the pheromone trails' values are used for making a stochastic decision to select the next hop.

POSANT is tolerant of position inaccuracy due to the forwarding ants being sent to different zones (not to specific nodes' positions) and due to its use of the pheromone trail value as the optimization criterion (which does not depend on the exact position of nodes).

POSANT's robustness is considered to be medium, since the failure of a single node might result in packet loss but does not result in a new route establishment, except if the only outgoing link of the source node that has a pheromone trail for *D* breaks or a message from this link is received stating that there is no route to *D*.

The use of periodic multiple greedy forwarding caused *POSANT*'s implementation complexity, scalability and packet overhead to be considered as medium. *POSANT* is guaranteed to be loop-free since repeated forward ants are destroyed. Moreover, it has a high probability of finding the optimal path since it is based on *ACO*, which guarantees message delivery and converges to a route which is very close to the optimal route, even if the network contains nodes with different transmission ranges.

Finally, *POSANT* may be implemented in both dense and sparse networks. *POSANT* is better for sparse networks than traditional greedy forwarding because if no pheromone trail exists, the route discovery packet will not be dropped; however, pheromone trail initialization is done. Moreover, if it is used in dense networks it will have good performance due to low processing and medium packet overheads.

3.2 Restricted Directional Flooding

This section discusses a selected set of existing restricted directional flooding routing protocols. The selected protocols are *DREAM* [15], *LAR* [24], *LARWB* [17] and *MLAR* [19].

3.2.1 DREAM

Distance Routing Effect Algorithm for Mobility (DREAM) [15] is an example of restricted directional flooding routing protocols, within which the sender will broadcast the packet towards nodes in a limited sector of the network, that is, to all single hop neighbors towards the destination. *DREAM* algorithm is a proactive protocol that uses a limited flooding of location update messages [16]. In *DREAM*, each node maintains a position database that stores position information about all other nodes in the network. Its location service can therefore be classified as an all-for-all approach. Thus, each node regularly floods packets to update the

position information maintained by the other nodes. The higher the speed of a node, the more the frequency at which it sends position updates. Also, the distance that a position update may travel before it is discarded provides accurate position information in the direct neighborhood of a node and less accurate information at nodes farther away, but this does not cause a problem since intermediate hops are able to update the position information contained in the data packet [7], [11]. In *DREAM* the message is forwarded to all neighbors whose direction belongs to the region that is likely to contain the destination *D*, called the expected region. The expected region is determined by the tangents from the source *S* to the circle centered at *D* and with radius equal to a maximal possible movement of *D* since the last location update [8]. The neighboring hops repeat this procedure using their information on *D*'s position.

Figure 7 is an example of expected region in *DREAM*. If a node does not have a neighbor in the required direction, a recovery procedure must be started. However, this procedure is not part of *DREAM* specification [13].

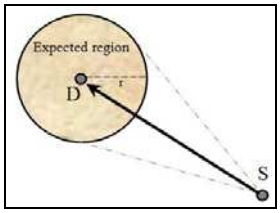

Figure 7
Example of the expected region in *DREAM*

Since *DREAM* uses restricted directional flooding to forward data packets themselves, there will be multiple copies of each packet at the same time. This increases the probability of using the optimal path; however, it decreases its scalability to large networks with a high volume of data transmissions and makes it more suitable for applications that require a high reliability and fast message delivery for infrequent data transmissions.

Discussion

DREAM is robust against position inaccuracy since it uses the expected region concept. It has higher communication complexity than greedy ones and therefore has less scalability to large networks; its scalability and packet overhead are considered to be medium. Moreover, it forwards packets to neighbors with closest direction, so it is not loop-free [8]. On the other hand, it can very simple be implemented and has high probability to find the optimal path. Finally it may be implemented in both dense and sparse networks; it is better for sparse networks than greedy forwarding, and even if it is used in dense ones it will have good performance due to low processing and medium packet overheads.

DREAM's location service is fundamentally different from other location services in that it requires that all nodes maintain position information about every other node. This leads to large overhead due to the position updates and large position information maintained by each node. Hence, *DREAM*'s location service is the least scalable position service and thus not appropriate for large-scale and general-purpose Ad-Hoc networks. On the other hand, a position query requires only a local lookup and the position of a given node will be inaccessible only upon the failure of all nodes, which makes it very robust.

DREAM is very robust against the failure of individual nodes since the data packet goes through multiple paths, so the failure of a single intermediate node does not prevent the packet from reaching its destination. This qualifies it for applications that require a high reliability and fast message delivery for very infrequent data transmissions [13].

3.2.2 LAR

Like *DREAM*, *Location-Aided Routing (LAR)* [24] is an example of restricted directional flooding routing protocols; however, partial flooding is used in *LAR* for path discovery purpose and in *DREAM* for packet forwarding [16]. Thus, *LAR* does not define a location-based routing protocol but instead proposes the use of position information to enhance the route discovery phase of reactive Ad-Hoc routing approaches [13]. If no information is available in the source about the position of the destination, *LAR* is reduced to simple flooding [13]. Otherwise, the expected zone (the area containing the circle and two tangents) is fixed from the source and defined based on the available position information (e.g., from a route that was established earlier) [7], [24]. A request zone is defined as the set of nodes that should forward the route discovery packet. The request zone typically includes the expected zone. Two request zone schemes have been proposed in [24]. The first scheme is a rectangular geographic region. In this case, nodes will forward the route discovery packet only if they are within that specific region. This type of request zone is shown in Figure 8.

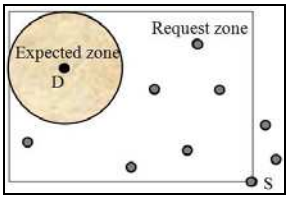

Figure 8
Example of request and expected zones in scheme 1 of *LAR*

In *LAR* scheme 2, the source or an intermediate node will forward the message to all nodes that are closer to the destination than itself. Thus, the node that receives the route request message will check whether it is closer to the destination than the

previous hop, and if so it will retransmit the route request message; otherwise, it will drop the message.

In order to find the shortest path in the network level, instead of selecting a single node as the next hop, several nodes will be selected for managing the route request message, and each of them will put its *IP* address in the header of the request packet. Therefore, the route through which the route request message is passed will be saved in the header of the message [17]; the message size will grow as it goes far from the source and the routing overhead will increase. In *LAR*, if the discovered route breaks for any reason, the route discovery process must start again.

Discussion

As a restricted directional flooding protocol, *LAR* exhibits some of *DREAM*'s properties, such as robustness against position inaccuracy, high communication complexity, medium scalability and packet overhead, not guaranteeing loop-freedom, implementation simplicity, high probability to find the optimal path and suitability for implementation in both dense and sparse networks.

On the other hand *LAR* does not require all nodes to maintain position information about every other node, as in *DREAM*. Instead, it simply uses the available position information from a route that was established earlier.

LAR is robust during route discovery since the route discovery packet goes through multiple paths; however, after route setup, it is like any other protocol that depends on route setup before sending the data packets; i.e., the failure of a single node might result in packet loss and the setting up of a new route. Hence, its robustness is considered to be low. On the other hand, its establishing of a route before beginning data sending makes it more suitable than *DREAM* in cases that require high volumes of data transmissions.

3.2.3 LARWB

Routes in *LAR* are often broken due to mobility [19]. New routes must be rediscovered in order to continue the routing of packets in the queue. This problem was solved by *Location-Aided Routing With Backup (LARWB)* [17] since another route is selected as a backup route which is used when a breakage appears in the primary route. Selecting an appropriate backup route can be done by considering two points: the primary and the backup routes must have the minimum common nodes; and the backup route should have a low probability of having nodes that may leave the radio range of their previous hop node.

Experimental results in [17] show that by using *LARWB*, the number of nodes which participate in routing operation, the average number of exchanged messages in route discovery process and also the average time of route discovery were considerably reduced.

Discussion

LARWB exhibits all the properties of *LAR* except that its robustness is considered to be medium since the failure of a single node might result in packet loss but does not result in setting up of a new route due to the usage of the route backup. This route backup also reduces the number of routing packets; however, we still cannot consider *LARWB*'s packet overhead as low as that in greedy.

3.2.4 *MLAR*

Multipath Location Aided Routing (MLAR) [19] is a multipath routing version of *LAR* that works efficiently in both 2-Dimensional (2D) and 3-Dimensional (3D) networks. Here multipath means the caching of alternate paths to be used in the event of the failure of the primary path and not the use of multiple simultaneous paths, which can lead to out of order packet delivery problems. The two most recently received routes are cached even if they are longer. It is believed that the most recently received path (even if it is longer) is the path most likely to succeed since mobility is more likely to break an older path. However, a routing protocol with longer average hop counts may have lower packet delivery rate. This is because the probability of a packet being dropped is higher if packets traverse longer paths. If the second path also fails a new route request cycle is initiated. Since the packet header contains the entire source route, all paths are checked easily as being loop free at each node that stores routes.

In order to be able to compare *MLAR* to other existing protocols, the authors have extended ns-2 to support 3D mobility models and routing protocols. The simulation results demonstrated the performance benefits of their multipath position based algorithm over a multipath non position based algorithm, *Ad-Hoc On-demand Multipath Distance Vector routing (AOMDV)* [12], as well as with both their single path versions (*LAR* and *Ad-Hoc On-demand Distance Vector routing (AODV)* [2]) in both 2D and 3D. Only *AOMDV* consistently performs better than *MLAR* in terms of overall packet delivery, but this was at the cost of more frequent flooding of control packets and so more bandwidth. Thus, *MLAR* has lower bandwidth and energy usage than non position-based protocols and is more scalable and efficient. Moreover, *MLAR* performs consistently better than *LAR* in terms of packet delivery ratio, by as much as 30% in some cases.

Discussion

MLAR has similar criteria as that of *LAR* except that its robustness is medium since the failure of a single node might result in packet loss but does not result in setting up of a new route due to the usage of the alternate paths. These alternate paths also reduce the packet overhead; however, it is still higher than that of greedy.

Since *MLAR* caches the most recently received routes, the probability of using the optimal path is very low. Lastly, since the packet header contains the entire source

route, all paths are checked easily as being loop free at each node that stores routes; loop freedom is guaranteed.

3.3 Hierarchical Routing Protocols

This section considers some hierarchical routing protocols, namely *GRID* [21], *TERMINODES* [9] and *LABAR* [6].

3.3.1 GRID

The two main strategies used to combine nodes location and hierarchical network structures are the zone-based routing and the dominating set routing [16]. In *GRID* algorithm [21] the dominating set concept is applied. A set is dominating if all the nodes in the system are either in the set or neighbors of nodes in the set. Routing based on a connected dominating set is a promising approach, since the searching space for a route is reduced to nodes in the set. *GRID* tries to exploit location information in route discovery, packet relay and route maintenance. In *GRID* the geographic area is partitioned into a number of squares called grids. In each grid, one mobile host (the one nearest to the physical center of the grid) will be elected as the leader of the grid. The size of each grid depends on transmission radius *R,* and several options are proposed, with the general idea of one leader being able to communicate directly with leaders in neighboring grids, and all nodes within each grid being connected to their leaders. Routing is then performed in a grid-by-grid manner through grids' leaders, and non-leaders have no such responsibility. Hence, the number of packets related to route search is insensitive to the network density. In fact, the cost slightly goes down as the host density increases, since routes become more stable with denser hosts.

In *GRID*, efforts are made in two directions to reduce the route search cost: using the locations of source and destination to confine the search range (like request zone in *LAR*) and delegating the searching responsibility to the gateway hosts. One attractive feature of *GRID* is its strong route maintenance capability since when a leader moves, another leader from the same grid replaces it through a handoff procedure. The probability of route breakage due to a node's roaming is reduced since the next hop is identified by its physical location, instead of by its address. *GRID* uses a specific field to detect duplicate request packets from the same source, so endless flooding of the same request can be avoided; i.e., it is loop free routing.

Simulations in [21] show that *GRID* can reduce the probability of route breakage, reduce the number of route discovery packets and lengthen routes' lifetimes. On the other hand, simulations also show that *GRID* uses longer paths than those used with *LAR*, since the former always confines relay hosts to gateway hosts while *LAR* tries to search the route with the smallest host count. Also, the authors do not

elaborate on the route maintenance required if a grid remains empty after its leader and only node leaves it.

Feeney and Nillson in [10] and Shih et al. in [5] concluded that the node power consumption when idle is nearly as large as when receiving data. Also, a node in idle mode spends about 15-30 times more energy than if it is in sleep mode. Therefore, the development of protocols that have as many nodes as possible sleeping, such as *GRID*, will significantly save network energy.

Discussion

GRID is a hierarchical routing that applies the concept of dominating sets. It, like *LAR*, uses the available position information of the destination from a route established earlier to implement a restricted directional flooding among grids. Consequently it is robust against position inaccuracy since it uses grid-by-grid routing and expected region concept. Although *GRID* has strong route maintenance capability and is very robust as regards node mobility, it is like any other protocol that depends on route setup before sending the data packets in the sense that the failure of a single node might result in packet loss and the setting up of a new route. Moreover, the authors in [21] did not elaborate on the route maintenance required when a grid remains empty after its leader and only node leaves it [16]. Thus, its robustness is considered to be medium.

GRID's implementation complexity is considered to be medium due to its dealing with the area as grids. Its scalability is high due to its use of restricted directional flooding and the delegating of the search responsibility to gateway hosts. Its packet overhead is considered to be low due to the reduced number of small routing packets. *GRID* uses a specific field to detect duplicate request packets from the same source, so endless flooding of the same request can be avoided; i.e., it is loop free. On the other hand, *GRID* uses long paths since packets are forced to be routed through grids' leaders.

Finally, it is better to implement *GRID* in dense networks because of its routing in a grid-by-grid manner through grids' leaders. So the number of packets related to route search is insensitive to the network density. On the contrary, the cost decreases slightly as the host density increases, since routes become more stable with denser hosts. On the other hand, if it is implemented in sparse networks, each node will be the gateway of its grid, and *GRID* may become like native *LAR*; consequently, it will consume network resources in dividing the area into grids and electing gateways without any benefit.

3.3.2 *TERMINODES*

TERMINODES [9] is an example of hierarchical routing protocols. *TERMINODES* presents a two-level hierarchy within which, if the destination is close to the sender (in terms of number of hops), packets will be routed based on a proactive distance vector. Greedy routing is used in long-distance routing [17].

TERMINODES addresses the following objectives: scalability (both in terms of the number of nodes and geographical coverage), robustness, collaboration and simplicity of nodes [16].

This routing scheme is a combination of two protocols called *Terminode Local Routing (TLR)* and *Terminode Remote Routing (TRR)*. *TLR* is a mechanism that allows for the reaching of destinations in the vicinity of a terminode and does not use location information for making packet forwarding decisions. *TRR* is used to send data to remote destinations and uses geographic information; it is the key element for achieving scalability and reduced dependence on intermediate systems. The major novelty is the *Anchored Geodesic Packet Forwarding (AGPF)* component of *TRR*. This is a source-path-based method designed to be robust for mobile networks: instead of using traditional source paths, that is lists of nodes, it uses anchored paths. An anchored path is a list of fixed geographical points, called anchors. The packet loosely follows the anchored path. At any point, the packet is sent in the direction of the next anchor in the anchored path by applying geodesic packet forwarding. When a terminode finds that the next anchor geographically falls within its transmission range, it deletes this from the anchored path and sends the packet in the direction of the new next anchor. This is repeated until the packet is sent in direction of the final destination [16].

The authors of [9] showed by means of simulations for mobile Ad-Hoc networks composed of several hundreds of terminodes that the introduction of a hierarchy can significantly improve the ratio of successfully delivered packets and the routing overhead compared to reactive Ad-Hoc routing algorithms. They also demonstrated the benefits of the combination of *TLR* and *TRR* over an existing protocol that uses geographical information for packet forwarding [13]. However, with the use of greedy routing in long distance routing, *TERMINODES* inherits the problems associated with it.

Discussion

TERMINODES provides a hierarchical approach to position-based Ad-Hoc routing. For long distance-routing it uses a greedy approach and therefore has characteristics similar to those of greedy forwarding. However, due to the usage of a non-position-based approach at the local level, it is more tolerant of position inaccuracy. As with other greedy forwarding protocols, in *TERMINODES* all nodes maintain a one-hop neighbor table; it uses all-for-some location service. Hence, a given node will be inaccessible upon the failure of a subset of the nodes; its location service has a medium robustness. Moreover it may fail to find the optimum route and has higher delivery rates for dense graphs.

TERMINODES's robustness is medium since the failure of an individual node may cause the loss of a packet in transit, but it does not require setting up a new route, as would be the case in topology-based Ad-Hoc routing. Due to using the two-level hierarchy approach, *TERMINODES* is considered to have medium implementation complexity. Such an approach is scalable since it does not require

routing discovery and maintenance in long-distance routing. Moreover, it has low packet overhead due to its small number of small-size packets. *TERMINODES* is considered to be a loop-free algorithm [16] since it always forces the message to make a step closer to the destination.

3.3.3 LABAR

Location Area Based Ad-Hoc Routing for GPS-Scarce Wide-Area Ad-Hoc Networks (LABAR) [6] is a hybrid virtual backbone and geographical location area based Ad-Hoc routing. The authors outlined that using *GPS* can increase the cost and power consumption of small mobile nodes. Thus, *LABAR* requires only a subset of nodes (called G-nodes) to know their exact location, forming location areas around them. G-nodes are interconnected into a virtual backbone structure to enable the efficient exchange of information for the mapping of the *IP* addresses to locations. Nodes that are not enabled with *GPS* equipment are called S-nodes.

Routing in *LABAR* consists mainly of three steps: zone formation, virtual backbone formation and directional routing. The first step of *LABAR* deals with forming the zones; i.e., making the decision as to which S-nodes should belong to which G-nodes. It is assumed that all G-nodes start the zone formation algorithm at the same time to acquire S-nodes. If an S-node has already been attached to a G-node, then the request message is ignored by the S-node. Upon being included in a zone, an S-node initiates the zone formation algorithm on its own in order to draw more S-nodes and form its neighborhood into its zone. By the end of this step, all S-nodes will belong to a G-node and G-nodes will know the IDs of their zone's S-nodes. The second step is to create an easy-to-manage virtual backbone for relaying the position information of nodes. G-nodes in the virtual backbone are responsible for resolving the *IP* addresses into geographical locations. To connect zones and get the virtual backbone to function, a G-node called the root sends connect messages to its adjacent zones. If the particular adjacent zone is not connected yet to the backbone, then it will be added to the backbone. Figure 9 shows an example of such a virtual backbone.

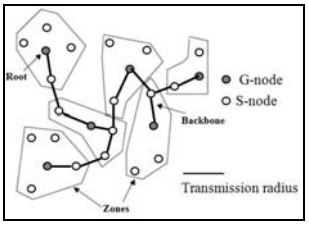

Figure 9
Example of virtual backbone in *LABAR*

The last step is directional routing. The source node queries the source G-node node to map the destination *IP* address into the geographical location area of the

destination. Then the source G-node determines the vector pointing from its own location to the destination's location. The resulting vector's direction is compared to each of the adjacent zones' directions and distances to determine the neighboring zone that will be used in relaying the data to the destination. Now, the source G-node will instruct the source node on how to route the packet inside the zone to reach the next zone with the least number of hops. The node that receives the packet in the neighboring zone will route the packet to the next zone by consulting its zone's G-node (which will consume time). In the case of a failure in the directional route (determined for example through expired hop counters), the source zone will be informed about the failure and the virtual backbone will be used to relay the packets.

LABAR is a combination of proactive and reactive protocols since the virtual backbone structure is used to update location information between G-nodes (in a proactive manner), while user packets are relayed using directional routing towards the direction zone of the destination. One of the important advantages of *LABAR* is the reduction of cost and power consumption through the relaxation of the *GPS*-equipment requirement in each node.

Discussion

LABAR is a hierarchal protocol since it uses zone-based routing. In *LABAR* the virtual backbone structure is used to update location information between G-nodes in a proactive manner; the used location service type is some-for-all. Generally, the robustness of such approaches is medium, since the position of a node will become unavailable if a subset of the nodes failed. *LABAR* exhibits some properties of greedy forwarding such as high scalability, low packet overhead and its suitability to be implemented in dense networks. *LABAR* is tolerable to position inaccuracy through its relaying the user packets towards the direction of the destination's zone, not towards its exact position.

In the case of a failure in the directional route of *LABAR*, the virtual backbone will be used to relay the packets; i.e., *LABAR*'s robustness is high since a failure of a single intermediate node does not prevent the packet from reaching its destination. *LABAR*'s implementation complexity is considered to be medium because of its use of zones. *LABAR* was not considered a loop-free protocol since it uses directional flooding and does not use any technique to indicate that a specific packet has been received earlier by a specific node. However, the expired hop counters can be used to stop the loops after a while.

One may think that *LABAR*'s probability of finding the optimal path is medium since it uses greedy routing; however, simulations have shown that *LABAR* usually uses a long path which sometimes exceeds double the length of the optimal path. This may be owing to using directional route towards the direction of destination's zone, not toward the exact position of it. So, *LABAR*'s probability of finding the optimal path is considered to be low.

4 Summary of the Selected Protocols

Table 1 summarizes the discussed protocols together with the evaluation criteria used.

Table 1
Characteristics of the presented forwarding strategies

Metric	LS type	LS robustness	FS type	FS toleration to position inaccuracy	FS robustness	FS implement. complexity	FS scalability	FS packet overhead	Loop free	Optimal path	Density
MFR	All-for-Some	Medium	Greedy (progress)	TR	Medium	Low	High	Low	Yes[8]	Medium	Dense
DIR	All-for-Some	Medium	Greedy (direction)	TR	Medium	Low	High	Low	No[8]	Medium	Dense
GPSR	All-for-Some	Medium	Greedy+ perimeter	TR	Medium	Medium	High	Low	Yes[16]	Medium	Both
ARP	All-for-Some	Medium	Greedy (distance + angle)	TR	Medium	Low	High	Low	No (only local ones)	Medium	Both
I-PBBLR	-	-	Greedy (progress + direction)	No beacons	Medium	Low	High	Low	Yes[23]	Medium	Dense
POSANT	-	-	Multiple Greedy (pheromone)	Zones and pheromone	Medium	Medium	Medium	Medium	Yes[18]	High	Both
DREAM	All-for-All	High	RDF	ER	High	Low	Medium	Medium	No[8]	High	Both
LAR	-	-	RDF	ER	Low	Low	Medium	Medium	No[8]	High	Both
LARWB	-	-	RDF	ER	Medium	Low	Medium	Medium	No	High	Both
MLAR	-	-	RDF	ER	Medium	Low	Medium	Medium	Yes[19]	Low	Both
GRID	-	-	Hierarchical	Grid-by-grid routing	Medium	Medium	High	Low	Yes	Low	Dense
TERMINODES	All-for-Some	Medium	Hierarchical	Short-distance routing range	Medium	Medium	High	Low	Yes[16]	Medium	Dense
LABAR	Some-for-All	Medium	Hierarchical	Zones	High	Medium	High	Low	No	Low	Dense

Abbreviations: LS: Location Service. FS: Forwarding Strategy. RDF: Restricted Directional Flooding. TR: Transmission Range. ER: Expected Region.

5 Directions of Future Research

In this paper we have shown that there are many approaches to performing position-based packet forwarding. However, there still exist a number of issues and problems that need to be addressed in future research.

Position-based protocols make it possible to have larger networks without scalability problems. However, geographical routing also offers attackers new opportunities, especially due to the fact that most protocols broadcast position information in the clear, allowing anyone within range to receive it. Hence, node position can be altered, making other nodes believe that it is in a different position. This may make nodes believe that the attacker is the closest node to the

destination and choose it as the next hop. Consequently, this attacker will be able to alter or drop packets.

Thus, it is worthwhile that more intensive work be done to secure position-based routing protocols to be able to defend against several attacks, not only from malicious nodes, but also from the compromised ones. Additionally, location privacy is one of the most major issues which need to be addressed, especially the fact that location privacy is hard to achieve when a node identifier can be immediately associated with its position.

Geographical routing protocols depend strongly on the existence of distributed scalable location services which are able to provide the location of any host at any time throughout the entire network. Hence, research should consider the scalability point upon developing new location services. Also, the most common way to enable nodes to know their locations is by equipping them with *GPS*. To decrease the cost and power consumption of small mobile nodes, other techniques for finding relative coordinates should be discussed.

We also need more concentration on power-conscious routing for saving network energy through the development of protocols that have as many sleeping nodes as possible and designing sleep period schedules for each node. Also, more studies should concentrate on *Quality of Service (QoS)*, geocast and multicast position-based routing.

Most routing protocols (not only position-based) consider nodes as neighbors if the Euclidean distance between them at most equals the transmission radius, which is the same for all nodes in the network. However, irregular transmission radius of a node (due to obstacles or noise), unidirectional links and different nodes' transmission radii should be taken into consideration. Moreover, many applications have nodes distributed in 3-Dimensional space, and little research has yet been done in this field.

Another issue that needs to be addressed is enabling connectivity among the individual Ad-Hoc networks, as well as the connectivity of any Ad-Hoc network to the Internet. This will, most likely, require the usage of hierarchal approaches to achieve scalability. This field has already been begun, but it needs further investigation.

Summary and Conclusions

Efficient routing among a set of mobile hosts is one of the most important functions in Ad-Hoc wireless networks. Many points should be taken into consideration when developing a routing protocol; some of these points are high delivery rate, reduced number of hops, small flooding ratio, small end-to-end delay and low power consumption. This survey has presented the current state of unicast position-based Ad-Hoc routing and provided a qualitative evaluation of the presented approaches. At the end, we identified a number of research opportunities which could lead to further improvements in position-based Ad-Hoc routing.

Forwarding techniques based on position information were classified into three distinct categories. Greedy routing does not require the maintenance of explicit routes; instead, it works by forwarding a single copy of data packet towards the destination. If a local maximum is encountered, a repair strategy can be used to avoid dropping the packet. After the comparison of the existing solutions we can conclude that the greedy packet forwarding is an efficient approach that scales well even with highly dynamic networks, and it is a promising strategy for general purpose position-based routing. However, it is not guaranteed to find the optimal path, and it may not find a path at all.

In restricted directional flooding the packets are broadcast in the general direction of the destination. On their way, the position information in the packets may be updated if a node has more current information about the destination's position. Restricted directional flooding has higher packet overhead and less scalability; however, its opportunity of finding the shortest path is higher. Using restricted directional flooding to set up a route in an efficient manner (such as in *LAR*) increases the probability of finding the optimal path and is suitable for cases that require a high volume of data transmissions. However, when it is used to forward the data packets themselves (such as in *DREAM*) it will be more suitable for situations where a small number of packets need to be transmitted very reliably.

Using hierarchical approaches increases the approach scalability. This may be done through the usage of zone-based routing, dominating sets, or by means of a position-independent protocol at the local level and a greedy variant at the long-distance level.

Security has recently gained a lot of attentions in topology-based routing protocols and many attempts to propose end-to-end security schemes have been made. However, it is obvious from the analysis that few research efforts have addressed position-based security issues. Finally, a few researchers have considered the power efficiency metric while developing their protocols.

Acknowledgement

This work was done under the VotF University Malaya fund no. FS132/2008C, PPP University Malaya fund no. PS091/2009A and PPP University Malaya fund no. PS410/2010B.

References

[1] B. Karp, H. Kung: GPSR: Greedy Perimeter Stateless Routing for Wireless Networks, in Proceedings of 6th Annual ACM/IEEE International Conference on Mobile Computing and Networking (MOBICOM 2000), Boston, Massachusetts, USA, 2000, pp. 243-254

[2] C. Perkins, E. Royer: Ad Hoc On-demand Distance Vector Routing, in Proceedings of 2nd IEEE Workshop on Mobile Computing Systems and Applications, New Orleans, LA, IEEE, 1999, pp. 90-100

[3] D. Johnson, D. Maltz: Dynamic Source Routing in Ad Hoc Wireless Networks, Mobile Computing, Vol. 353, Kluwer Academic Publishers, 1996, pp. 153-181

[4] E. Kranakis, H. Singh, J. Urrutia: Compass Routing on Geometric Networks, in Proceedings of 11th Canadian Conference on Computational Geometry, Vancouver, 1999, pp. 51-54

[5] E. Shih, S. Cho, N. Ickes, R. Min, A. Sinha, A. Wang, A. Chandrakasan: Physical Layer Driven Protocol and Algorithm Design for Energy-Efficient Wireless Sensor Networks, in Proceedings of 7th Annual International Conference on Mobile Computing and Networking (MOBICOM 2001), Rome, Italy, ACM, 2001, pp. 272-287

[6] G. Zaruba, V. Chaluvadi, A. Suleman: LABAR: Location Area Based Ad Hoc Routing for GPS-Scarce Wide-Area Ad Hoc Networks, in Proceedings of 1st IEEE International Conference on Pervasive Computing and Communications (PerCom'03), 2003, pp. 509-513

[7] H. Takagi, L. Kleinrock: Optimal Transmission Ranges for Randomly Distributed Packet Radio Terminals, IEEE Transactions on Communications, Vol. 32, No. 3, 1984, pp. 246-257

[8] I. Stojmenovic, X. Lin: Loop-Free Hybrid Single-Path/Flooding Routing Algorithms with Guaranteed Delivery for Wireless Networks, IEEE Transactions on Parallel and Distributed Systems, Vol. 12, No. 10, 2001, pp. 1023-1032

[9] L. Blazevic, L. Buttyan, S. Capkum, S. Giordano, J. Hubaux, J. Le Boudec: Self-Organization in Mobile Ad-Hoc Networks: the Approach of Terminodes, IEEE Communication Magazine, Vol. 39, No. 6, 2001, pp. 166-174

[10] L. Feeney, M. Nilsson: Investigating the Energy Consumption of a Wireless Network Interface in an Ad Hoc Networking Environment, in Proceedings of 20th Annual Joint Conference of the IEEE Computer and Communications Societies (INFOCOM 2001), Vol. 3, USA, 2001, pp. 1548-1557

[11] L. Qabajeh, M. L. Mat Kiah, M. Qabajeh: A Qualitative Comparison of Position-based Routing Protocols for Ad-Hoc Networks, International Journal of Computer Science and Network, Vol. 9, No. 2, 2009, pp.131-140

[12] M. Marina, S. Das: On-Demand Multipath Distance Vector Routing in Ad Hoc Networks, in Proceedings of 9th International Conference on Network Protocols (ICNP 01), 2001, pp. 14-23

[13] M. Mauve, J. Widmer, H. Hartenstein: A Survey on Position-based Routing in Mobile Ad-Hoc Networks, IEEE Network, Vol. 15, No. 6, 2001, pp. 30-39

[14] P. Bose, P. Morin, I. Stojmenovic, J. Urrutia: Routing with Guaranteed Delivery in Ad Hoc Wireless Networks, in Proceedings of 3rd International Workshop on Discrete Algorithms and Methods for Mobile Computing and Communications, 1999, pp. 48-55

[15] S. Basagni, I. Chlamtac, V. Syrotiuk, B. Woodward: A Distance Routing Effect Algorithm for Mobility (DREAM), in Proceedings of 4th Annual ACM/IEEE International Conference on Mobile Computing and Networking (MOBICOM), Dallas, TX, USA, 1998, pp. 76-84

[16] S. Giordano, I. Stojmenovic, L. Blazevic: Position-based Routing Algorithms for Ad Hoc Networks: A Taxonomy. In Cheng, X., Huang, X., Du, D.Z: Ad hoc wireless Networking, Kluwer, 2003, pp. 103-136 http://www.site.uottawa.ca/~ivan/routing-survey.pdf

[17] S. Kalhor, M. Anisi, A. Haghighat: A New Position-based Routing Protocol for Reducing the Number of Exchanged Route Request Messages in Mobile Ad-hoc Networks, in Proceedings of 2nd International Conference on Systems and Networks Communications (ICSNC 2007), IEEE, 2007, p. 13

[18] S. Kamali, J. Opatrny: POSANT: A Position-based Ant Colony Routing Algorithm for Mobile Ad-hoc Networks, in Proceedings of 3rd International Conference on Wireless and Mobile Communications (ICWMC'07), IEEE, 2007

[19] S. Nanda, R. Gray: Multipath Location-aided Routing in 2D and 3D, IEEE Wireless Communications and Networking Conference (WCNC 2006), Vol. 1, 2006, pp. 311-317

[20] V. Giruka, M. Singhal: Angular Routing Protocol for Mobile Ad-hoc Networks, in Proceedings of 25th IEEE International Conference on Distributed Computing Systems Workshops (ICDCSW'05), 2005, pp. 551-557

[21] W. Liao, Y. Tseng, J. Sheu: GRID: A Fully Location-Aware Routing Protocols for Mobile Ad Hoc Networks, Telecommunication Systems, Vol. 18, 2001, pp. 61-84

[22] X. Wu: VPDS: Virtual Home Region-based Distributed Position Service in Mobile Ad Hoc Networks, in Proceedings of 25th IEEE International Conference on Distributed Computing Systems (ICSCS 2005), 2005, pp. 113-122

[23] Y. Cao, S. Xie: A Position-based Beaconless Routing Algorithm for Mobile Ad Hoc Networks, in Proceedings of International Conference on Communications, Circuits and Systems, Vol. 1, IEEE, 2005, pp. 303-307

[24] Y. Ko, N. Vaidya: Location-aided Routing (LAR) in Mobile Ad Hoc Networks, Wireless Network (WINET), Vol. 6, No. 4, ACM, 2000, pp. 307-321

Control Strategies, Robustness Analysis, Digital Simulation and Practical Implementation for a Hybrid APF with a Resonant Ac-link

Yang Han[1], Lin Xu[2], Muhammad Mansoor Khan[2], Chen Chen[2]

[1]Department of Power Electronics, School of Mechatronics Engineering, University of Electronic Science and Technology of China, No.2006 XiYuan Road, West Park of Chengdu Hi-Tech Zone, 611731 Chengdu, P. R. China

[2]Department of Electrical Engineering, XuHui Campus, Shanghai JiaoTong University, #1954 HuaShan Road, 200030 Shanghai, P. R. China

E-mail: hanyang_facts@hotmail.com, xulin198431@hotmail.com

Abstract: This paper proposes a novel hybrid active power filter (HAPF) topology based on the cascaded connection of the AC-side capacitor and the third-order LCL-filter, which has the advantage of the conventional hybrid filter and the LCL-filter in terms of reduced dc-link voltage and better switching ripple attenuation. The robust deadbeat control law is derived for the current loop, with special emphasis on robustness analysis. The stability and robustness analysis under parameter variations are presented for the converter-side current tracking scheme and the grid-side current tracking scheme. It is found that the stability margins obtained from the converter-side current tracking control scheme are generally higher than those obtained from the grid-side current tracking scheme. However, the converter-side current tracking scheme is sensitive to the variation of the damping resistance, and it would impose additional parameter uncertainty on the control system and complicate the problem. Hence the grid-side current tracking scheme is implemented. The simulation results obtained from Matlab/Simulink are presented for verification, where the inductance variation and grid disturbance scenarios are also taken into consideration. The effectiveness of the proposed hybrid APF is substantially confirmed by the simulation and experimental results.

Keywords: power quality; harmonic estimation; active filter; hybrid; robustness analysis; digital signal processor (DSP)

1 Introduction

Due to the proliferation of nonlinear loads in electric power distribution systems, electrical power quality has been an important and growing problem Particularly, power quality problems are causing detrimental effects for customers; these problems result from current harmonics produced by nonlinear loads, e.g., variable ac motor drives, HVDC systems, arc furnaces, grid-connected renewable energy resources and household appliances. The increased harmonic pollution causes a significant increase in line losses, instability, and voltage distortion when the harmonic currents travel upstream and produce voltage drop across the line impedance [1-3]. This fact has led to the proposal of more stringent requirements regarding power quality, like those specifically collected in the standards IEC-61000-3-{2,4} and IEEE-519 [4, 5]. For several decades, active power filters (APFs) have been recognized as the most effective solutions for harmonic compensation. Their objective is to suppress the current harmonics and to correct power factor (PF), especially in fast-fluctuating loads [2]. A lot of recent literature has tried to improve APFs by developing new topologies or new control laws [3, 6-8]. In order to provide a systematic elaboration of the recent development in APFs, a survey of the state-of-the-art techniques for the APFs is outlined herein.

It was reported in Refs. [9-13] that the performance of APF is dependent on how the reference compensating signals are generated. The instantaneous reactive power theory [9], the modified *p-q* theory [10], the synchronous reference frame (SRF) theory [11], the instantaneous i_d-i_q theory [12], and the method for the estimation of current reference by maintaining the voltage of *dc*-link [13] are reported for generating references through the subtraction of positive sequence fundamental component from the nonlinear load current. These control schemes look very attractive for their simplicity and ease of implementation, but fail to provide an adequate solution under extreme conditions of harmonics, reactive power and their combinations, with limited power rating of voltage source inverter (VSI) [14]. In such cases, to safeguard the hardware, the protection scheme isolates the APF, which leaves the system to the mercy of unwanted disturbances; or, if reference signals are saturated, then the APF becomes a source of disturbance itself. In [15], the reference generation method based on the Goertzel algorithm was proposed; however, some practical issues, i.e, the stability of the closed-loop current control algorithm and voltage regulation, have not been discussed. Other solutions to harmonic detection and reference signal generation are based on artificial intelligence (AI), particularly on neural networks (NNs) [16]. In recent literature, a slightly different approach was proposed in [17], where an adaptive linear neural network (ADALINE), trained by a least-squares algorithm (LS) [18], was used to estimate the active component of the fundamental load current. In [19], a single-phase distributed generation (DG) unit with APF capability via adaptive neural filtering (ANF) was introduced, and which does not need *a priori* training of the neural network. Hence it is neither

cumbersome nor computationally demanding, especially if compared with other neural-based techniques that require offline training [16].

Apart from the neural network approach, the genetic algorithm (GA) was also introduced for APF applications [20]. These control strategies have a common drawback concerning the global stability of the closed-loop system, which hampers its application for practical APF systems. To overcome the stability issues, the sliding-mode control (SMC) was presented in [21]. However, the calculation technique for the reference current using SMC scheme is complicated and would require more advanced and sophisticated hardware for the practical implementation of the algorithm. The direct power control (DPC), on the other hand, is an indirect current control method that originates from the instantaneous reactive power theory (IRPT) [22]. However, the main drawback of DPC is the high gain of the controller and, as a consequence, the values of the input inductors have to be very large to attenuate the current ripple, which increases the cost, size, and weight of the system [22, 23]. Recent works have introduced predictive control and model-based strategies for DPC with improved steady state and dynamic response [23], where the control loops is designed with a high gain at the selected harmonic frequencies. In [24], repetitive control was utilized for harmonic compensation, which achieves low total harmonic distortion current waveforms, but at the expense of fast sampling capabilities of the hardware. As an alternative approach, resonant harmonic compensators were presented in [25], which were based on generalized integrators connected in parallel with a conventional tracking regulator. Moreover, deadbeat current control schemes were reported in [26]; these offer the potential for achieving the fastest transient response, more precise current control, zero steady-state error, and full compatibility with digital control platforms. However, there are two main practical issues related to the deadbeat control, namely: 1) bandwidth limitation due to the inherent plant delay and 2) sensitivity to plant uncertainties.

In addition to the reference current generation schemes and the current control algorithms, the switching ripple attenuation and the electromagnetic interference (EMI) reduction are also of vital importance for the practical implementation of APFs. To resolve the issues of switching ripple and EMI reduction, normally a large value inductance for output filtering should be adopted [27]. However, a high value inductance degrades system dynamic response and also requires a higher voltage on the dc-link of the inverter, thus resulting in higher power losses. By connecting a small-rated active filter directly to the single-tuned *LC*-filter to form the hybrid topology, the dc-link voltage of the VSI can be reduced to a fraction of the mains voltages. In [27], an alternative solution for switching frequency reduction using *LCL*-filter-based topology was presented.

In order to take the advantage of the hybrid *LC*-filter topology for reduced dc-link voltage and the *LCL*-filter for better switching ripple attenuation, a novel hybrid APF (HAPF) configuration is proposed in this paper. It resembles the single-tuned *LC*-filter-based hybrid topology at lower frequency range, and thus the dc-link

voltage of the VSI is remarkably reduced. By using a third-order *LCL*-filter to replace the *L*-section of the resonant *LC*-filter, the total filter inductors are significantly reduced and satisfactory switching ripple attenuation is achieved. The adaptive linear neural network [28] is utilized for harmonic estimation and reference current generation for the proposed hybrid APF. Additionally, the deadbeat control law [26] is derived based on the low frequency equivalent model of the *LCL*-filter section of the inverter power-stage. A novel average current tracking scheme is proposed to enhance the performance of the deadbeat control algorithm. The selective harmonic compensation is achieved by using the ADALINE-based harmonic estimation scheme, which significantly reduces controller bandwidth and thus enhances system stability. To validate the proposed APF and its control strategies, extensive simulation results are presented. And a prototype system is also built. The laboratory experiments are also provided, and these are consistent with the theoretical analysis and simulation results.

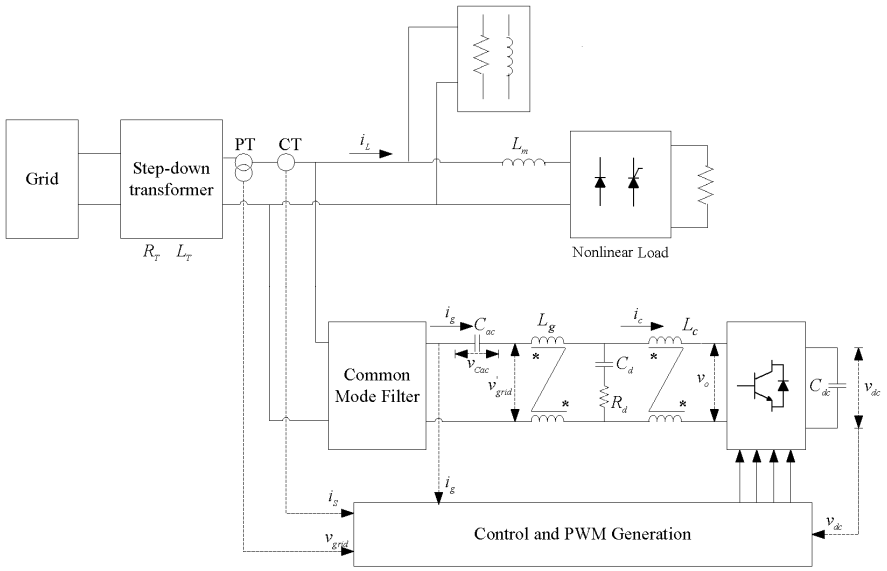

Figure 1
Single-phase schematic of the proposed hybrid active power filter

The organization of this paper is as follows. The mathematical formulation of the proposed HAPF is presented in Section 2. Three aspects related to the control system are discussed in Section 3, namely, the ADALINE-based harmonic estimation scheme, the feedback plus feed-forward control scheme and the dc-link voltage regulation of the VSI. The simulation results and experimental results are presented in Sections 4 and 5, respectively. Finally, Section 6 concludes this paper.

2 Mathematical Model of the Proposed Hybrid APF

Fig. 1 shows the circuit diagram of the proposed *LCL*-filter-based hybrid APF (HAPF). Three single-phase topologies are utilized in the laboratory prototype system as demonstrated by the experimental results; thus only the single-phase representation is illustrated herein. The *LCL*-filter, consisting of L_g, C_d and L_c with possible passive damping resistance R_d, is used as the output filter of the VSI and grid interface. The *LCL*-section is equivalent to an inductor (*L*-filter) at lower frequencies. Hence the *LC* resonant topology is formed between the *LCL*-filter and AC-side capacitor C_{ac} in the low frequency range, and thus the dc-side voltage of the VSI is remarkably reduced to achieve lower EMI emission and higher inverter efficiency. Referring to Fig. 1, the system equations can be derived according to Kirchhoff's laws, which yield:

$$\begin{cases} L_g \dfrac{di_g}{dt} + L_c \dfrac{di_c}{dt} + v_{Cac} = v_{grid} - v_o \\ i_g = C_{ac} \dfrac{dv_{Cac}}{dt} \\ i_d = C_d \dfrac{dv_{cd}}{dt} = i_g - i_c \\ v_{cd} + R_d (i_g - i_c) = L_c \dfrac{di_c}{dt} + v_o \end{cases} \tag{1}$$

where parameters i_g and i_c are inverter currents across the inductors L_g and L_c respectively, i_d and v_{cd} represent the current and voltage across the capacitor of the *RC*-filter brunch, and v_{Cac} is the voltage of the AC-side capacitor C_{ac}. Rearranging Eq. (1), the following equations can be derived:

$$\begin{cases} L_g \dfrac{di_g}{dt} = -R_d (i_g - i_c) - v_{cd} - v_{Cac} + v_{grid} \\ L_c \dfrac{di_c}{dt} = R_d (i_g - i_c) + v_{cd} - v_o \\ C_{ac} \dfrac{dv_{Cac}}{dt} = i_g \\ C_d \dfrac{dv_{Cd}}{dt} = i_g - i_c \end{cases} \tag{2}$$

Assuming $L_g = L_{0g} + \Delta L_g$, $L_c = L_{0c} + \Delta L_c$, $C_{ac} = C_{0ac} + \Delta C_{ac}$, $C_d = C_{0d} + \Delta C_d$, $R_d = R_{0d} + \Delta R_d$, where the subscript '0' denotes the nominal value; ΔL_g , ΔL_c , ΔC_{ac} , ΔC_d , ΔR_d are parameter variations around their nominal values. Therefore, Eq. (2) can be rearranged as:

$$\begin{cases} L_{0g}\dfrac{di_g}{dt} = R_{0d}(i_c - i_g) + \Delta R_d(i_c - i_g) - \Delta L_g\dfrac{di_g}{dt} - v_{cd} - v_{Cac} + v_{grid} \\ L_{0c}\dfrac{di_c}{dt} = R_{0d}(i_g - i_c) + \Delta R_d(i_g - i_c) - \Delta L_c\dfrac{di_c}{dt} + v_{cd} - v_o \\ C_{0ac}\dfrac{dv_{Cac}}{dt} = i_g - \Delta C_{ac}\dfrac{dv_{Cac}}{dt} \\ C_{0d}\dfrac{dv_{Cd}}{dt} = i_g - i_c - \Delta C_d\dfrac{dv_{Cd}}{dt} \end{cases} \tag{3}$$

Let

$$\begin{cases} f_1 = \Delta R_d(i_c - i_g) - \Delta L_g\dfrac{di_g}{dt} + v_{grid} + n_1 \\ f_2 = \Delta R_d(i_g - i_c) - \Delta L_c\dfrac{di_c}{dt} + n_2 \\ f_3 = -\Delta C_{ac}\dfrac{dv_{Cac}}{dt} + n_3 \\ f_4 = -\Delta C_d\dfrac{dv_{Cd}}{dt} + n_4 \end{cases} \tag{4}$$

where n_1, n_2, n_3 and n_4 represent unstructured uncertainties due to un-modeled dynamics. Then Eq.(3) can be expressed in the state-space equations:

$$\dot{\mathbf{x}} = \mathbf{A}_{\mathbf{c}0}\mathbf{x} + \mathbf{B}_{\mathbf{c}0}\mathbf{u} + \mathbf{G}_{\mathbf{c}0}\mathbf{f}\ ,\ \mathbf{y} = \mathbf{C}\mathbf{x} \tag{5}$$

where the vector of state variables $\mathbf{x} = [i_g, i_c, v_{Cac}, v_{cd}]^T$, the equivalent input vector $\mathbf{u} = [0, v_o, 0, 0]^T$, $\mathbf{f} = [f_1, f_2, f_3, f_4]^T$, and the nominal system matrices $\mathbf{A}_{\mathbf{c}0}$, $\mathbf{B}_{\mathbf{c}0}$, $\mathbf{G}_{\mathbf{c}0}$ and $\mathbf{C}$ are derived as:

$$\mathbf{A}_{\mathbf{c}0} = \begin{bmatrix} -\dfrac{R_{0d}}{L_{0g}} & \dfrac{R_{0d}}{L_{0g}} & -\dfrac{1}{L_{0g}} & -\dfrac{1}{L_{0g}} \\ \dfrac{R_{0d}}{L_{0c}} & -\dfrac{R_{0d}}{L_{0c}} & 0 & \dfrac{1}{L_{0c}} \\ \dfrac{1}{C_{0ac}} & 0 & 0 & 0 \\ \dfrac{1}{C_{0d}} & -\dfrac{1}{C_{0d}} & 0 & 0 \end{bmatrix}, \mathbf{B}_{\mathbf{c}0} = diag(0, -\frac{1}{L_{0c}}, 0, 0)\ ,$$

$$\mathbf{G}_{\mathbf{c}0} = diag(\frac{1}{L_{0g}}, \frac{1}{L_{0c}}, \frac{1}{C_{0ac}}, \frac{1}{C_{0d}})\ ,\ \mathbf{C} = diag(1, 0, 0, 0)$$

The transfer functions from the output of the voltage source inverter (VSI) to the grid-side current, converter-side current and the *RC*-filter brunch under nominal system parameters are derived as:

$$G_g(s)=\frac{I_g(s)}{V_o(s)}=\frac{R_{0d}s^2+\frac{1}{C_{0d}}s}{\{L_{0g}L_{0c}s^4+(L_{0g}+L_{0c})R_{0d}s^3+ [\frac{1}{C_{0d}}(L_{0g}+L_{0c})+\frac{L_{0c}}{C_{0ac}}]s^2+\frac{R_{0d}}{C_{0ac}}s+\frac{1}{C_{0ac}C_{0d}}\}} \tag{6}$$

$$G_c(s)=\frac{I_c(s)}{V_o(s)}=\frac{L_{0g}s^3+R_{0d}s^2+(\frac{1}{C_{0d}}+\frac{1}{C_{0ac}})s}{\{L_{0g}L_{0c}s^4+(L_{0g}+L_{0c})R_{0d}s^3 +[\frac{1}{C_{0d}}(L_{0g}+L_{0c})+\frac{L_{0c}}{C_{0ac}}]s^2+\frac{R_{0d}}{C_{0ac}}s+\frac{1}{C_{0ac}C_{0d}}\}} \tag{7}$$

$$G_{RC}(s)=\frac{I_{RC}(s)}{V_o(s)}=-\frac{L_{0g}s^3+\frac{1}{C_{0ac}}s}{\{L_{0g}L_{0c}s^4+(L_{0g}+L_{0c})R_{0d}s^3 +[\frac{1}{C_{0d}}(L_{0g}+L_{0c})+\frac{L_{0c}}{C_{0ac}}]s^2+\frac{R_{0d}}{C_{0ac}}s+\frac{1}{C_{0ac}C_{0d}}\}} \tag{8}$$

To provide an in-depth view of the frequency domain characteristics of Eqs. (6)-(8), the parameter design of the hybrid *LCL*-filter should be addressed, as reported in [27]. The major issues regarding the *LCL*-filter design include the total cost of inductors, the resonant frequency of the hybrid *LCL*-filter, the size of the damping resistance and the attenuation at the switching frequency in order to comply with the power quality standards imposed by IEEE 519-1992 and the IEC 61000-3-4 [4, 5]. In the present case, the resonant frequency at low frequency range is selected between the third and fifth order harmonic frequency to minimize the total cost of the hybrid filter. The next step is to design the *LCL*-filter parameters, which is the full order model of the *L*-filter model for the hybrid *LC*-filter design procedure. There are three major issues in designing of the *LCL*-filter parameters; namely, choosing the resonant frequency, the inductance ratio between the grid-side inductance (L_g) and converter-side inductance (L_c), and the selection of damping resistance [27]. The resonant frequency of the *LCL*-filter is selected significantly higher than the highest load harmonics compensated by the APF. And the selection of damping resistance is a compromise between the requirements of the stability margin and power dissipation. Further, the power quality standards should be rigorously studied to verify the designed parameters [4, 5]. Following these guidelines for parameter design, the specification and system parameters of the proposed hybrid APF is illustrated in Table 1.

Table 1
Specifications and system parameters

Name	Parameters
APF power rating	75 kVA (3-phase)
Nominal grid voltage (phase-to-phase)	380 V(RMS)
Ac-side capacitor C_{ac}	1000 μF
Grid-side inductor of the *LCL*-filter L_g	250 μH
Converter-side inductor of the *LCL*-filter L_c	500 μH
Ac capacitor of the *LCL*-filter C_d	10 μF
Damping resistance R_d	2 Ω
Dc-side voltage of the VSI	300 V
A/D sampling frequency	10 kHz
Inverter switching frequency	10 kHz

Fig. 2 shows the frequency responses of the hybrid *LCL*-filter corresponding to Eqs.(6)-(8), where the effect of damping resistance is also investigated. Fig. 2*a* indicates that the frequency response from inverter output $V_o(s)$ to the grid-side current of the *LCL*-filter $I_g(s)$ shows two resonant peaks, one in the low frequency range (185 Hz), another in the high frequency range (2.9 kHz). The resonant peak at low frequency range is caused by the *LC* resonance between the AC-side filter C_{ac} and the total inductance $L=L_g+L_c$. And the resonant peak at the high frequency range is caused by the *LC* resonance between the *RC*-filter (R_d and C_d) and the total inductance $L=L_g+L_c$. The damping resistance is found to have negligible effect on the resonant peak in the lower frequency range. However, smaller damping resistance causes significant resonant peak in the high frequency range, which implies that insufficient damping might cause instability of the system at higher frequencies. Fig. 2*b* shows the frequency response of the hybrid *LCL*-filter section from $V_o(s)$ to $I_c(s)$. A similar resonant frequency in the low frequency range is observed.

Whereas Fig. 2*b* shows two resonant peaks in the high frequency range, one shows the characteristic of overshoot and another shows the feature of undershoot. Fig. 2*b* also shows that smaller damping resistance results in higher resonant peaks in the high frequency range, making the system vulnerable due to poor stability margin. Fig. 2*c* shows the frequency response from inverter output $V_o(s)$ to the *RC*-filter brunch of the *LCL*-filter $I_{RC}(s)$. It shows that the resonant peak in the lower frequency range has an attenuation of -10dB, which implies that the lower frequency component generated by the VSI is damped in the *RC*-filter. However, the resonant peak in the high frequency range shows an attenuation of about 15 dB when the damping resistance is 0.05 Ω. It can also be inferred that smaller damping resistance results in current amplification at the *RC*-filter. Therefore, proper damping is mandatory to ensure the stable operation of the proposed system.

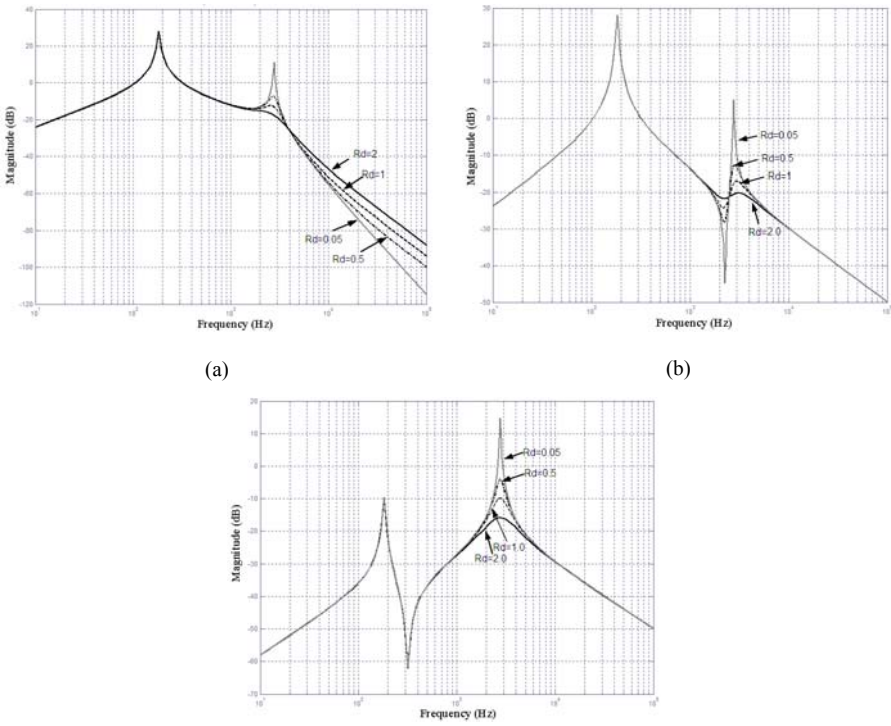

(a) (b)

(c)

Figure 2

Frequency response of the hybrid *LCL*-filter under different damping resistances. (a) From inverter output $V_o(s)$ to the grid-side current of the *LCL*-filter $I_g(s)$; (b) From inverter output $V_o(s)$ to the inverter-side current $I_c(s)$; (c) From inverter output $V_o(s)$ to the *RC*-filter brunch of the *LCL*-filter $I_{RC}(s)$

3 Control System Design

The current control loop is a key element for APFs. The cascaded controller structure is adopted for the proposed hybrid APF, which contains inner current-loop and outer dc-voltage loop (Fig. 3). The inner current loop is responsible for fast harmonic tracking and the outer loop is used for balancing the active power flow of the APF through regulating the dc-bus capacitor voltage [26, 27].

The adaptive linear neural network (ADALINE) is utilized as a harmonic identifier, which recursively extracts the amplitude and phase angle of an individual harmonic component by using the Widrow-Hopf learning algorithm [28]. By using the ADALINE algorithm, the compensating current of the APF is

reconstructed; thus, the control bandwidth is effectively reduced, and the stability margin imposed by the current tracking algorithm is ensured over a wide operation range. To enhance the performance of the APF, the feed-forward control algorithm is devised by feeding the non-active component of the load current into the feed-forward loop, and the voltage drop across the AC-side capacitor C_{ac} is utilized as the voltage feed-forward variable in the feed-forward control loop.

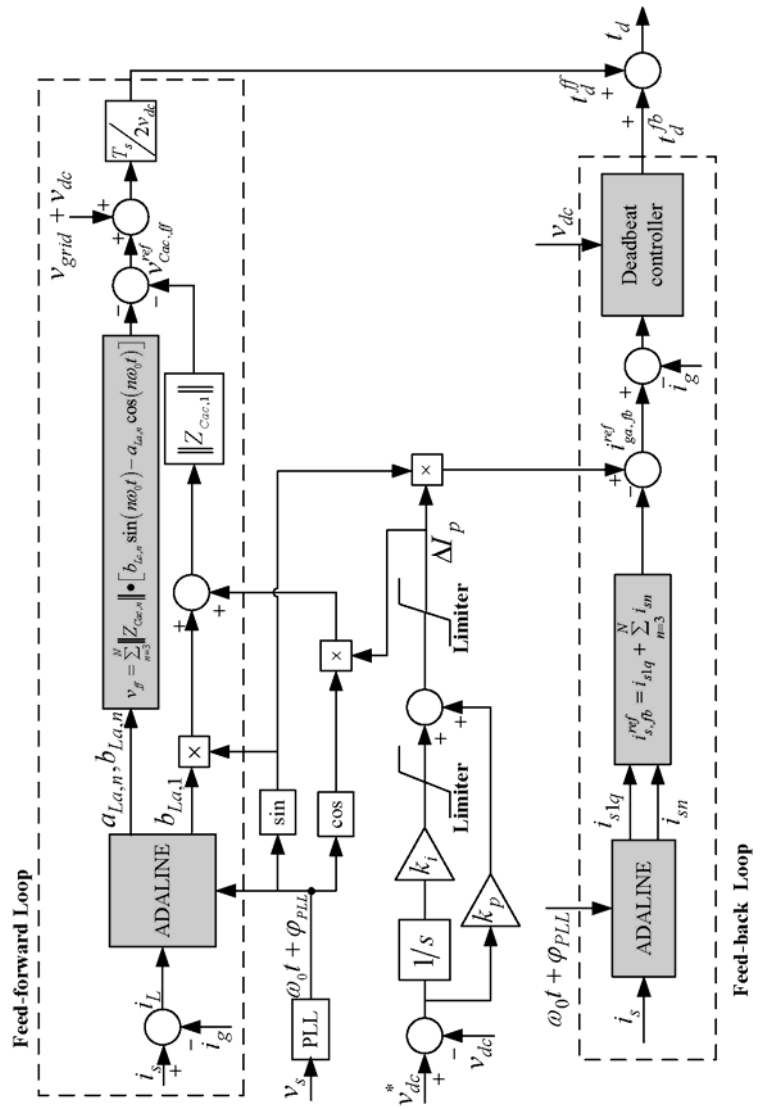

Figure 3
Control block diagram of the proposed hybrid LCL-filter based active power filter. (This figure is vertically presented for better clarity)

3.1 Harmonic Detection using Adaptive Linear Neural Network (ADALINE)

The most critical issues associated with APF control is that of finding an appropriate control algorithm, one which can obtain an accurate reference signal for control purposes, particularly when the load harmonics are time-varying [6-17]. Therefore, the performance of the APF strongly depends on the harmonic detection method [9-11]. To take advantage of the on-line learning capabilities of neural networks (NNs), the adaptive linear neural network (ADALINE) is utilized to estimate the time-varying magnitudes and phases of the fundamental and harmonic components from the source current and load current (Fig. 1) [6]. The motivation is to adopt a combined feed-forward and feedback control strategy for the proposed APF using ADALINEs as harmonic identifiers. For the sake of clarity, the background of ADALINE is briefly outlined herein [6, 28, 29].

An arbitrary signal $Y(t)$ at the kth sampling time can be represented by the Fourier series expansion as:

$$\begin{aligned} Y(t_k) &= \sum_{n=0,1,2,3,\cdots}^{N} A_n \sin(n\omega_0 t_k + \varphi_n) + \varepsilon(t_k) \\ &= \sum_{n=0,1,2,3,\cdots}^{N} (a_n \sin n\omega_0 t_k + b_n \cos n\omega_0 t_k) + \varepsilon(t_k) \end{aligned} \tag{9}$$

where A_n and φ_n are correspondingly amplitude and the phase angle of the nth order harmonic component, and $\varepsilon(t_k)$ represents higher order components and random noise, and a_n, b_n (n is integer) are also known as the Fourier coefficients, which can be calculated recursively using the least-mean-square (LMS) algorithm [30]. In other words, the Fourier coefficients can be estimated recursively by formulating the target signal $Y(t_k)$ as the inner product of the pattern vector X_k and weight vector W_k, which are defined as:

$$\begin{cases} X_k = [1, \sin\omega_0 t_k, \cos\omega_0 t_k, \cdots, \sin N\omega_0 t_k, \cos N\omega_0 t_k\ ]^T \\ W_k = [b_0^k, a_1^k, b_1^k, a_2^k, b_2^k, ..., a_N^k, b_N^k]^T \end{cases} \tag{10}$$

Therefore, the square error on the pattern X_k can be expressed as

$$\begin{aligned} \varepsilon_k &= \frac{1}{2}(d_k - X_k^T W_k)^2 = \frac{1}{2} e_k^2 \\ &= \frac{1}{2}(d_k^2 - 2d_k X_k^T W_k + W_k^T X_k X_k^T W_k) \end{aligned} \tag{11}$$

where d_k is the desired scalar output for the target signal $Y(t_k)$. The mean-square error (MSE) ε can be obtained by calculating the expectation of both sides of Eq. (12), as:

$$\varepsilon = E[\varepsilon_k] = \frac{1}{2}E[d_k^2] - E[d_k X_k^T]W_k + \frac{1}{2}W_k^T E[X_k X_k^T]W_k \tag{12}$$

where the weights are assumed to be fixed at W_k while computing the expectation. The objective of the ADALINE is to find optimal weight vector $\hat{W}_k$ that minimizes the MSE of Eq. (13). When mean-square error ε is minimized, the weight vector $\hat{W}$ after convergence would be [6, 28, 29]:

$$\hat{W} = [b_0, a_1, b_1, a_2, b_2, ..., a_N, b_N]^{\mathrm{T}} \tag{13}$$

Thus, the fundamental component and the *n*th order harmonic component of the measured signal can be obtained as:

$$\begin{cases} Y_1(t_k) = a_1 \sin(\omega_0 t_k) + b_1 \cos(\omega_0 t_k) \\ Y_n(t_k) = a_n \sin(n\omega_0 t_k) + b_n \cos(n\omega_0 t_k) \end{cases} \tag{14}$$

In this paper, the fixed-point digital signal processors (DSPs) from Texas Instruments (TI TMS320F2812) are adopted to implement the ADALINE-based estimation algorithm and the control algorithm for the APF. The phase and magnitude of the individual harmonic components, from the 3rd to the 25th order, are estimated for the higher convergence of ADALINE, but only the lower-order harmonics from 3rd to 19th order are selected in the current-loop control to save the computation resources. However, the selected harmonics can easily be extended. The accurate and rapid estimation capability of ADALINE is crucial when selective harmonic compensation is adopted in current control for the purpose of reducing controller bandwidth, thus increasing system robustness and enhancing stability [28].

3.2 The Proposed Feedback plus Feed-forward Control Strategy

In this section, the feedback plus feed-forward control scheme are described consecutively. Firstly, the deadbeat control law for the average current control scheme is introduced by using the discrete domain representation of the *LCL*-filter model. Then, stability analysis of the closed-loop current control schemes under various parameter variation scenarios is presented. Finally, the feed-forward control loop, which achieves fast load disturbance compensation, is presented.

In the forthcoming derivations, the current in phase '*a*' is analyzed for the sake of brevity. However, the same conclusions can also be applied for the other phases. The load current in phase '*a*' is represented by:

$$
\begin{aligned}
& i_{La}(t) = \sum_{n=1}^{\infty} I_{La,n} \sin(n\omega_0 t + \varphi_{La,n}) \\
& = a_{La,1} \sin(\omega_0 t + \varphi_{PLL}) + b_{La,1} \cos(\omega_0 t + \varphi_{PLL}) \\
& + \sum_{n=2}^{\infty} [a_{La,n} \sin(n\omega_0 t) + b_{La,n} \cos(n\omega_0 t)]
\end{aligned} \tag{15}
$$

where $a_{La,1}=I_{La,1}\cos(\varphi_{La,1}-\varphi_{PLL})$ and $b_{La,1}=I_{La,1}\sin(\varphi_{La,1}-\varphi_{PLL})$ represent the amplitude of the fundamental active and reactive component of the nonlinear load current, and φ_{PLL} represents the initial phase angle of the phase-locked-loop (PLL) [28, 29], which is synchronized with the fundamental frequency component of the grid voltage. And $I_{La,n}$ and $\varphi_{La,n}$ (n>1, n is integer) represent the amplitude and phase angle of the nth order harmonic component of the load current, respectively. The parameters $a_{La,n}$ and $b_{La,n}$ (n>1, n is integer) represent the weights of the individual harmonic component obtained from the ADALINE. The individual harmonic component can be reconstructed using Eq. (15) if the weights $a_{La,n}$ and $b_{La,n}$ (n is integer) are precisely calculated. Similarly, the source-side current in phase 'a' supplied by the distribution system is represented as:

$$
\begin{aligned}
& i_{sa}(t) = a_{sa,1} \sin(\omega_0 t + \varphi_{PLL}) + b_{sa,1} \cos(\omega_0 t + \varphi_{PLL}) \\
& + \sum_{n=2}^{\infty} [a_{sa,n} \sin(n\omega_0 t) + b_{sa,n} \cos(n\omega_0 t)]
\end{aligned} \tag{16}
$$

where $a_{sa,1}= I_{sa,1}\cos(\varphi_{sa,1}-\varphi_{PLL})$ and $b_{sa,1}=I_{sa,1}\sin(\varphi_{sa,1}-\varphi_{PLL})$ represent the amplitude of the fundamental active and reactive component of the source-side current, and $I_{sa,n}$ and $\varphi_{sa,n}$ (n>1, n is integer) represent the amplitude and phase angle of the nth order harmonic component of the source-side current, respectively. The parameters $a_{sa,n}$ and $b_{sa,n}$ (n is integer) represent the weights of the individual harmonic component obtained from a separate ADALINE block in the feedback loop (Fig. 3). To achieve the feedback current tracking control, the fundamental reactive component and the selected harmonic components are utilized as the reference current for the APF. Furthermore, the output of the voltage-loop controller ΔI_p, after being multiplied by a unit sinusoidal signal synchronized with the grid voltage by using PLL, is added to the feedback current to compensate for the power loss of the inverter [6-19]. Therefore, the compensating current of the APF in the feedback loop is represented as:

$$
\begin{aligned}
& i_{ga,fb}^{ref}(t) = -\{b_{sa,1} \cos(\omega_0 t + \varphi_{PLL}) + \sum_{n=3}^{N} [a_{sa,n} \sin(n\omega_0 t) + b_{sa,n} \cos(n\omega_0 t)]\} \\
& + \Delta I_p \sin(\omega_0 t + \varphi_{PLL})
\end{aligned} \tag{17}
$$

Note that a finite number of harmonics is selected in Eq. (17), since only a limited number of harmonics are processed in the ADALINE-based harmonic estimation scheme due to the limited computational load, constrained by the DSP.

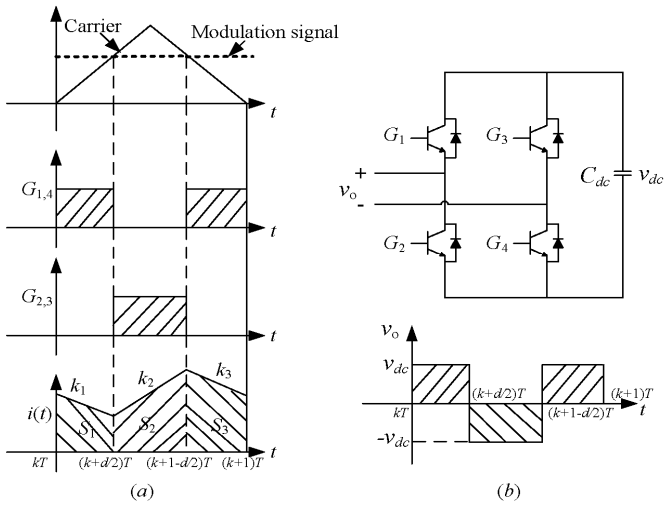

Figure 4

Principle of current tracking control scheme: (a) Geometrical interpretation for deriving the average current during one PWM period; (b) Schematic of the voltage source inverter (VSI) and its output voltage

3.2.1 Deadbeat Control Scheme for the Feedback Current Control Loop

To simplify the control effort for the proposed hybrid APF, the deadbeat control scheme is adopted in the feedback closed-loop for reference current tracking. Only the *LCL*-section of the hybrid APF is used to derive the deadbeat control law. The AC-side capacitor voltage, on the other hand, is regulated by controlling the injection current of the *LCL*-filter. Moreover, the *RC*-filter brunch of the *LCL*-filter section, adopted for high frequency switching ripple attenuation and stability enhancement, shows little impact on the low frequency range below 2 kHz (Fig. 2*a*). Hence, the effect of the *RC*-filter is neglected when deriving the deadbeat control law for the sake of simplicity. Therefore, the degree of freedom of the control system for the hybrid APF is significantly reduced.

Utilizing the concept of the reduced order model for the *LCL*-filter, the deadbeat current control law for the inner current loop is derived herein. Firstly, the differential equation for the inductor current across *LCL*-filter section is represented as:

$$v_{grid} - v_{Cac} - v_o = \left(L_g + L_c\right)\frac{di}{dt} \tag{18}$$

where parameters v_{grid}, v_{Cac} and v_o represent the grid side voltage, the AC-capacitor voltage and output voltage of the voltage source inverter, respectively. In order to derive the discrete domain representation of Eq. (18), the operation

principle of the inverter under different switching patterns is given by Fig. 4. It can be observed that, when the switches G_1 and G_4 are switched on, and the switches G_2 and G_3 are turned off, the output voltage of the inverter is v_{dc}, and then the inverter current undergoes a falling stage, according to the direction of current defined in Fig. 1. When the switches G_1 and G_4 are switched off, and switches G_2 and G_3 are switched on, the output voltage of VSI would be $-v_{dc}$, which results in a rising stage of the inverter current (Fig. 4*a*-*b*). Therefore, Eq. (18) can be rewritten in the discrete form using piecewise linear representation as:

$$\begin{cases} i_g[(k+\frac{d}{2})T_s]-i_g[kT_s]=\frac{d}{2}T_s\cdot\frac{v_{grid}[k]-v_{Cac}[k]-v_{dc}[k]}{L_g+L_c} \\ i_g[(k+1-\frac{d}{2})T_s]-i_g[(k+\frac{d}{2})T_s]=(1-d)T_s\cdot\frac{v_{grid}[k]-v_{Cac}[k]+v_{dc}[k]}{L_g+L_c} \\ i_g[(k+1)T_s]-i_g[(k+1-\frac{d}{2})T_s]=\frac{d}{2}T_s\cdot\frac{v_{grid}[k]-v_{Cac}[k]-v_{dc}[k]}{L_g+L_c} \end{cases} \tag{19}$$

where d in Eq. (19) is the abbreviation of $d[k]$, representing the duty cycle of the kth control period. The grid voltage and AC capacitor voltage are assumed to be constants during one PWM cycle (quasi-steady-state model) in discrete equations. After mathematical manipulations of Eq. (19), the duty ratio of PWM signal at the kth control period is obtained as:

$$d[k]=-\frac{(L_g+L_c)\{i_g[(k+1)T_s]-i_g[kT_s]\}}{2v_{dc}[k]T_s}+\frac{v_{dc}[k]+v_{grid}[k]-v_{Cac}[k]}{2v_{dc}[k]} \tag{20}$$

In order to track the reference signal and achieve deadbeat control, the current at (k+1)th sampling interval $i_g[(k+1)T_s]$ should be replaced by the reference signal at the next sampling cycle [26, 31]. Nevertheless, in the proposed hybrid APF, the resetting filters are adopted at the sampling stage, and hence the instantaneous quantities cannot be directly obtained at kth and (k+1)th sampling instants. On the contrary, all the sampling signals, i.e., the voltages and currents, are the average quantities of the previous period. Therefore, the current tracking scheme should be modified to account for the average quantities, and hence the theoretical derivation of the average current during the kth control period is given herein.

Referring to Fig. 4*a*, it can be deduced that, during the switching on/off processes of the power electronic switches, the output current during one control period undergoes rising and falling stages according to the switching patterns of the switches. Therefore, the average current can be obtained by dividing the total shadowed area denoted as S_1, S_2 and S_3 by the control period T_s. As shown in Fig. 4*a*, the slopes of the current $i(t)$ during one PWM control period are denoted as:

$$\begin{cases} k_1 = k_3 = \dfrac{v_{grid}[k] - v_{Cac}[k] - v_{dc}[k]}{L_g + L_c} \\ k_2 = \dfrac{v_{grid}[k] - v_{Cac}[k] + v_{dc}[k]}{L_g + L_c} \end{cases} \tag{21}$$

The shadowed area denoted as S_1, S_2 and S_3 in Fig. 4*a* can be derived as:

$$\begin{cases} S_1 = \dfrac{1}{2}\{2i_g[kT_s] + k_1 \dfrac{d}{2}T_s\} \cdot \dfrac{d}{2}T_s \\ S_2 = \dfrac{1}{2}\{2i_g[kT_s] + k_1 dT_s + k_2(1-d)T_s\} \cdot (1-d)T_s \\ S_3 = \dfrac{1}{2}\{2i_g[kT_s] + k_1 \cdot \dfrac{3d}{2}T_s + 2k_2(1-d)T_s\} \cdot \dfrac{d}{2}T_s \end{cases} \tag{22}$$

Therefore, the average inverter current of the *k*th control period can be derived as:

$$\overline{i_g}[kT_s] = \frac{S_1 + S_2 + S_3}{T_s} \tag{23}$$

Therefore, from Eqs. (22) and (23), the instantaneous current at the (*k*+1)th sampling instant can be rewritten as:

$$i_g[(k+1)T_s] = \overline{i_g}[kT_s] + \frac{\{v_{dc}[k] + v_{grid}[k] - v_{Cac}[k]\}T_s - 2dT_s v_{dc}[k]}{2(L_g + L_c)} \tag{24}$$

Hence, the duty cycle can be rewritten in terms of the average current of the *k*th sampling period as:

$$d[k] = -\frac{(L_g + L_c)\{i_g[(k+1)T_s] - \overline{i_g}[kT_s]\}}{v_{dc}[k]T_s} + \frac{v_{dc}[k] + v_{grid}[k] - v_{Cac}[k]}{2v_{dc}[k]} \tag{25}$$

In Eq. (25), the term L/T_s is denoted as the current controller gain derived from the deadbeat control law. It is interesting to notice from Eq. (20) and Eq. (25) that the deadbeat control law for the average current tracking control and the instantaneous current tracking control have similar expression. However, the controller gain, denoted by L/T_s, for the current tracking error in Eq. (25) of the average current tracking scheme is twice the value of the instantaneous current tracking scheme, which shows the superior performance for the proposed scheme; i.e., the adoption of resetting filter is helpful in increasing the current controller gain, thus increasing the tracking dynamics for the reference compensation current of the APF.

Nevertheless, the aforementioned deadbeat control scheme is based on the reduced order model of the *LCL*-filter, where the *RC*-filter is neglected at the modeling stage. Hence, the performance of the current tracking scheme may be imperfect

due to model mismatch and parameter uncertainty. Therefore, the stability analysis of the current control scheme is rigorously studied to ensure the stable operation of the APF. In the forthcoming subsection, the *RC*-filter is incorporated into the mathematical manipulations and the selection of the current controller gain is discussed with respect to the stability requirement.

3.2.2 Root Locus Analysis of the Grid-side Current Tracking Scheme

This subsection presents the performance of the grid-side current (i_g) tracking scheme by using the closed-loop root locus plots and the open-loop impulse responses. The plant model under this scenario can be obtained by deriving the open-loop transfer function from the inverter output to the grid-side current of the *LCL*-filter section:

$$G_{g,plant}(s) = \frac{R_{0d}C_{0d}s + 1}{L_{0g}L_{0c}C_{0d}s^3 + R_{0d}C_{0d}(L_{0g} + L_{0c})s^2 + (L_{0g} + L_{0c})s} \tag{26}$$

The current loop transfer function $G_{g,cc}(s)$ is simply represented by a proportional gain K_{cc}, and the transfer function of the delay due to PWM generation and computational delay (T_d) is expressed as:

$$G_{g,delay}(s) = e^{-sT_d} \tag{27}$$

Hence the open loop transfer function of the grid-side current tracking control algorithm can be represented by:

$$\begin{aligned} G_{g,open}(s) &= G_{g,cc}(s)G_{g,plant}(s)G_{g,delay}(s) \\ &= K_{cc}e^{-sT_d}\frac{R_{0d}C_{0d}s + 1}{L_{0g}L_{0c}C_{0d}s^3 + R_{0d}C_{0d}(L_{0g} + L_{0c})s^2 + (L_{0g} + L_{0c})s} \end{aligned} \tag{28}$$

Therefore, the closed-loop transfer function of the grid-side current tracking control scheme can be derived as:

$$\begin{aligned} G_{g,close}(s) = \frac{G_{g,open}(s)}{1 + G_{g,open}(s)} = \frac{K_{cc}e^{-sT_d}(R_{0d}C_{0d}s + 1)}{\{L_{0g}L_{0c}C_{0d}s^3 + R_{0d}C_{0d}(L_{0g} + L_{0c})s^2} \\ +(K_{cc}R_{0d}C_{0d}e^{-sT_d} + L_{0g} + L_{0c})s + K_{cc}e^{-sT_d}\} \end{aligned} \tag{29}$$

It should be noted that, to achieve an optimal dynamic performance of the proposed hybrid APF, the selection of the current loop controller should be rigorously studied. If the gain is selected too small, the dynamic response of the current tracking will be sluggish. On the other hand, if the current loop gain is too high, the stability constraint of the closed-loop control will be violated. Hence the current loop gain will be carefully studied in the subsection by using discrete domain representation of the closed-loop transfer function under various parameter variation scenarios, which will be discussed herein.

Referring to Eq. (29), the closed-loop transfer function of the current loop tracking control under nominal system parameters can be rewritten in the discrete domain (z-domain) as:

$$G_{g,close}(z)=\frac{K_{cc}(0.08836z^2+0.09784z-0.004811)}{\{z^4-0.9407z^3+(0.08836K_{cc}+0.2419)z^2 \\ +(0.09784K_{cc}-0.3012)z-0.004811K_{cc}\}} \tag{30}$$

where T_d is assumed to be one control period (T_s=100μs). The closed-loop root locus plot and open-loop impulse response of the grid-side current control scheme under nominal system parameters is illustrated by Fig. 5*a*. It can be observed that the closed-loop system would be unstable when the current controller gain exceeds 5.6. It is interesting to notice that this stability margin is lower than the controller gain directly derived from the deadbeat control low. This gain limit should be satisfied in the practical system to ensure closed-loop stability, as discussed in the simulation and experimental results. Moreover, it can be observed from Fig. 5*a* that the open-loop impulse response shows an overshoot of 0.18 p.u with the response time of 1.2 millisecond. In order to investigate the robustness of the presented hybrid APF and the control scheme, the influence of parameter variations is also rigorously studied herein by taking into account the variation of interfacing inductances, the control delay and the *RC* filter parameter variations.

It should be noted that the interfacing inductances may deviate from their nominal values in practical systems due to the variation of the operational conditions, humidity and temperature deviation. Hence the influence of inductance variations is considered here by changing the grid-side inductance to 0.8 p.u and converter side inductance to 1.2 p.u. Under this condition, the closed-loop transfer function of the grid-side current tracking scheme in discrete domain can be derived as:

$$G_{g,close}(z)=\frac{K_{cc}(0.09322z^2+0.1047z-0.00515)}{\{z^4-0.9617z^3+(0.09322K_{cc}+0.2731)z^2 \\ +(0.1047K_{cc}-0.3114)z-0.00515K_{cc}\}} \tag{31}$$

The closed-loop root locus plot and open-loop impulse response of the grid-side current tracking scheme under inductance variations is illustrated by Fig. 5*b*. It can be observed that the closed-loop system would be unstable when the current controller gain exceeds 5.15, which is lower than the case of the nominal system parameters. Besides, it can be observed from Fig. 5*b* that the open-loop impulse response shows an overshoot of 0.195 p.u with the response time of 1.2 millisecond. Next, we consider the effect of the control delay on the performance of the current tracking control, which is associated with PWM generation and computational delay, etc. Considering the control delay as $1.5T_s$, then the closed-loop transfer function of the current tracking algorithm is derived as:

$$G_{g,close}(z) = \frac{K_{cc}(0.02253z^3 + 0.1347z^2 + 0.02834z - 0.00414)}{\{z^5 - 0.9407z^4 + (0.02253K_{cc} + 0.2419)z^3 + (0.1347K_{cc} - 0.3012)z^2 + 0.02834K_{cc}z - 0.00414K_{cc}\}} \quad (32)$$

The closed-loop root locus plot and open-loop impulse response of the grid-side current tracking scheme corresponding to the variation of control delay is illustrated by Fig. 5*c*. It can be observed that the closed-loop system would be unstable when the current controller gain exceeds 4.87, which is lower than the case of the nominal system parameters. Besides, it can be observed from Fig. 5*c* that the open-loop impulse response shows an overshoot of 0.17 p.u with the response time of 1.2 millisecond, which is almost the same as the case of the nominal system parameters. It is also found that a longer delay would not only deteriorate the stability of the closed-loop system, but would also significantly hamper the quality of the output voltage waveform, which would result in poor precision of the current tracking algorithm. However, as discussed in the experimental results, the control delay does not have a significant effect on the performance of the system since the ADALINE-based harmonic estimation algorithm was adopted to generate the reference current for the current loop controller. Hence the control delay can be compensated for by shifting the reference compensation current of the APF by one sampling period, which can be easily achieved by adding $\Delta\theta_n$ ($\Delta\theta_n=\omega_n T_s=2\pi f_0 n T_s$, n is the harmonic order) to the phase angle of the individual harmonic component by modifying the $sin(n\omega_0 t)$ and $cos(n\omega_0 t)$ into $sin(n\omega_0 t+\Delta\theta_n)$ and $cos(n\omega_0 t+\Delta\theta_n)$ in the reconstruction process of the ADALINE-based harmonic estimation algorithm.

Next, we consider the effect of the *RC*-filter parameters on the performance of the current loop tracking algorithm by changing the filtering capacitance and the damping resistance, respectively. If the filtering capacitance of the *RC*-filter is modified to C_d=5 μF, then the closed-loop transfer function of the current tracking control algorithm is derived as:

$$G_{g,close}(z) = \frac{K_{cc}(0.1391z^2 + 0.1296z + 0.04588)}{\{z^4 + 0.05781z^3 + (0.1391K_{cc} - 0.7566)z^2 + (0.1296K_{cc} - 0.3012)z + 0.04588K_{cc}\}} \quad (33)$$

The closed-loop root locus plot and open-loop impulse response of the grid-side current tracking control with the variation of filtering capacitance is illustrated by Fig. 5*d*. It can be observed that the closed-loop system would be unstable when the current controller gain exceeds 7.66, which is much higher than the case of the nominal system parameters. Moreover, it can be observed from Fig. 5*d* that the open-loop impulse response shows an overshoot of 0.144 p.u with the response time of 1.1 millisecond, which is remarkably lower than the case of nominal system parameters. It is found that the smaller the filtering capacitance, the higher the stability margin and the faster the dynamic response of the current tracking

control algorithm can be achieved. Nevertheless, smaller filtering capacitance would result in poor attenuation of higher order switching harmonics. Therefore, a compromise should be achieved between the filtering efficiency and the closed-loop stability constraint. Next, the effect of the damping resistance on the closed-loop current tracking control is examined by changing the damping resistance R_d to 0.1Ω, and then the closed-loop transfer function can be derived as:

$$G_{g,close}(z) = \frac{K_{cc}(0.05958z^2 + 0.189z + 0.05182)}{\{z^4 - 0.6889z^3 + (0.05958K_{cc} + 0.6306)z^2 + (0.189K_{cc} - 0.9418)z + 0.05182K_{cc}\}} \quad (34)$$

The closed-loop root locus plot and open-loop impulse response of the grid-side current tracking control scheme with the variation of damping resistance is illustrated by Fig. 5*e*. It can be observed that the closed-loop system would be unstable when the current controller gain exceeds 5.29, which is lower than the case of the nominal system parameters. Besides, it can be observed from Fig. 5*e* that the open-loop impulse response shows an overshoot of 0.23 p.u with the response time of 18 millisecond, which is significantly higher than the case of the nominal system parameters. It is found that a smaller damping resistance would result in a smaller stability margin and a prolonged dynamic response of the current tracking control scheme. On the other hand, however, the reduced damping resistance results in a higher damping of higher order switching harmonics of the inverter, as demonstrated in Fig. 2*a*. Therefore, a compromise must be achieved between the stability constraint and the switching ripple attenuation for practical systems. Table 2 shows the summery of the stability margin and dynamic response of the grid-side current tracking control scheme, where the results obtained under the nominal system parameters and parameter variation scenarios are presented. In the forthcoming subsection, a similar analysis is provided for the closed-loop locus diagrams and open-loop impulse responses of the current regulation scheme based on the converter-side tracking control scheme.

Table 2
Summary of the stability margin and dynamic response of the grid-side current tracking scheme

Case	Marginal gain (deg)	Overshoot (pu)	Response time (ms)
1	5.6	0.18	1.2
2	5.15	0.195	1.2
3	4.87	0.17	1.2
4	7.76	0.144	1.1
5	5.29	0.23	18

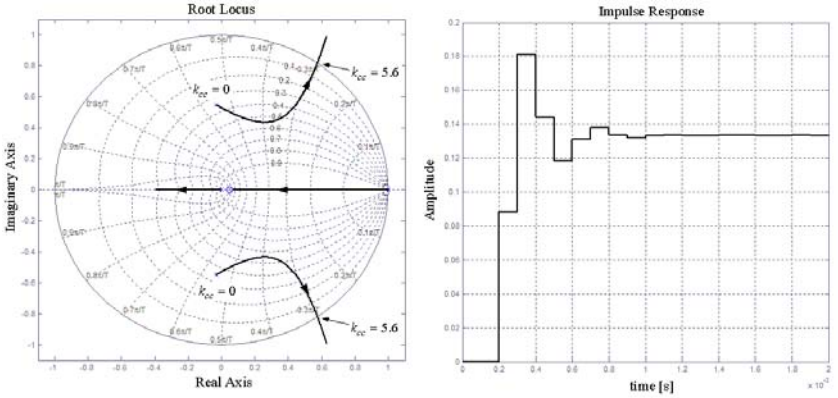
Root Locus
Imaginary Axis
Real Axis
$k_{cc} = 0$
$k_{cc} = 5.6$
$k_{cc} = 0$
$k_{cc} = 5.6$
Impulse Response
Amplitude
time [s]

(a)

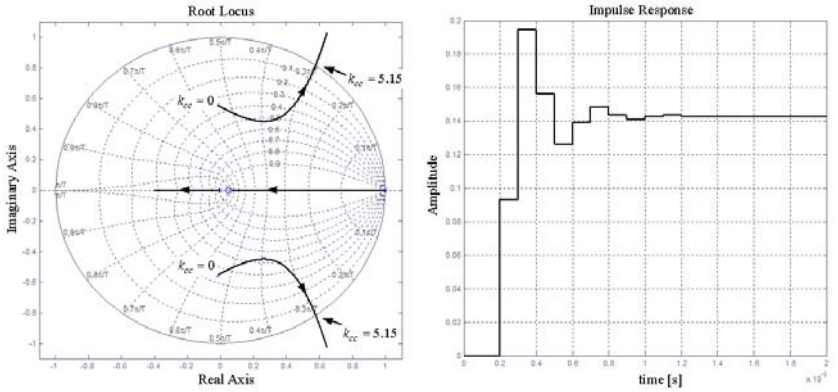
Root Locus
Imaginary Axis
Real Axis
$k_{cc} = 0$
$k_{cc} = 5.15$
$k_{cc} = 0$
$k_{cc} = 5.15$
Impulse Response
Amplitude
time [s]

(b)

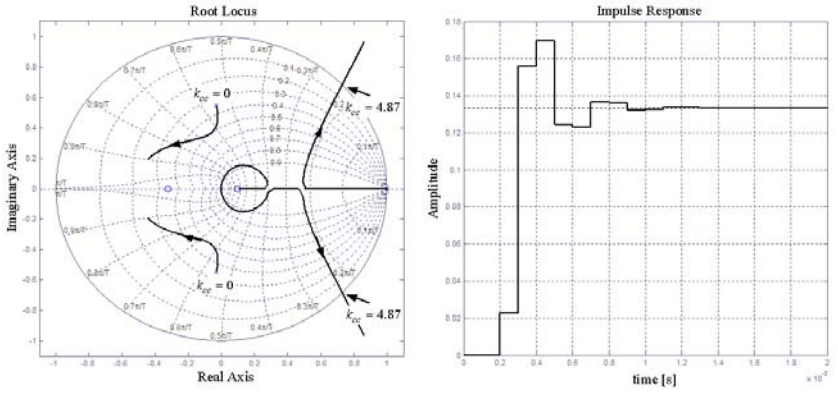
Root Locus
Imaginary Axis
Real Axis
$k_{cc} = 0$
$k_{cc} = 4.87$
$k_{cc} = 0$
$k_{cc} = 4.87$
Impulse Response
Amplitude
time [s]

(c)

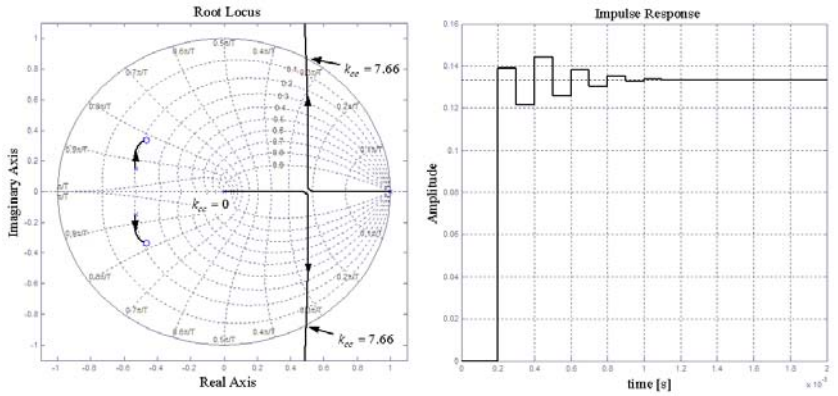

(d)

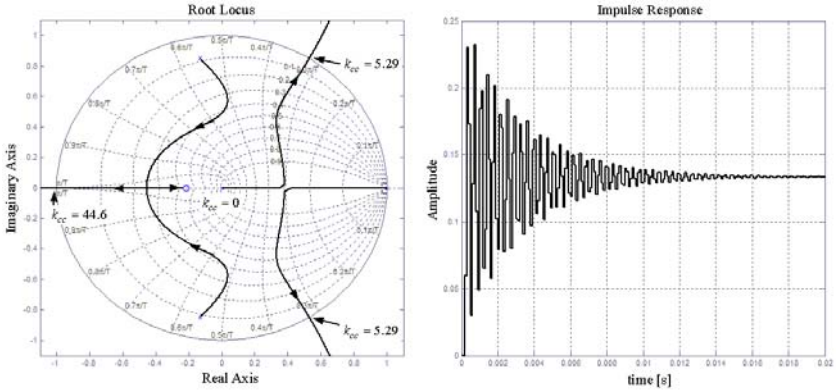

(e)

Figure 5

The closed-loop root locus diagrams and the open-loop impulse responses of the current regulation algorithm based on the grid-side current (i_g) tracking control scheme. (a) Root locus and impulse response under nominal parameters; (b) Root locus and impulse response under inductance variations; (c) Root locus and impulse response under different control delay (T_d=1.5T_s); (d) Root locus and impulse response under different *RC*-filter capacitance C_d; (e) Root locus and impulse response under different *RC*-filter resistance R_d

3.2.3 Root Locus Analysis of the converter-side Current Tracking Scheme

This subsection presents the performance of the converter-side current (i_c) tracking scheme by using the closed-loop root locus plots and the open-loop impulse responses. The plant model under this scenario can be obtained by deriving the open-loop transfer function from the inverter output to the converter side current of the *LCL*-filter section:

$$G_{c,plant}(s) = \frac{L_{0g}C_{0d}s^2 + R_{0d}C_{0d}s + 1}{L_{0g}L_{0c}C_{0d}s^3 + R_{0d}C_{0d}(L_{0g} + L_{0c})s^2 + (L_{0g} + L_{0c})s} \tag{35}$$

The current loop transfer function $G_{c,cc}(s)$ is simply represented by a proportional gain K_{cc}, and the transfer function of the delay due to PWM generation and computational delay is derived as:

$$G_{c,delay}(s) = e^{-sT_d} \tag{36}$$

Hence the open loop transfer function of the converter-side current tracking control algorithm under the present case can be represented by:

$$G_{c,open}(s) = K_{cc}e^{-sT_d}\frac{L_{0g}C_{0d}s^2 + R_{0d}C_{0d}s + 1}{L_{0g}L_{0c}C_{0d}s^3 + R_{0d}C_{0d}(L_{0g} + L_{0c})s^2 + (L_{0g} + L_{0c})s} \tag{37}$$

Therefore, the closed-loop transfer function of the converter-side current tracking control scheme is:

$$G_{c,close}(s) = \frac{G_{c,open}(s)}{1 + G_{c,open}(s)} = \frac{K_{cc}e^{-sT_d}(L_{0g}C_{0d}s^2 + R_{0d}C_{0d}s + 1)}{\{L_{0g}L_{0c}C_{0d}s^3 + [K_{cc}e^{-sT_d}L_{0g}C_{0d} + R_{0d}C_{0d}(L_{0g} + L_{0c})]s^2 + (K_{cc}R_{0d}C_{0d}e^{-sT_d} + L_{0g} + L_{0c})s + K_{cc}e^{-sT_d}\}} \tag{38}$$

The closed-loop transfer function of the converter-side current tracking scheme can be rewritten in the discrete domain, which will be discussed in detail herein. Under nominal system parameters, the closed-loop transfer function of the converter-side current (i_c) tracking control scheme can be rewritten in the discrete domain (z-domain):

$$G_{c,close}(z) = \frac{K_{cc}(0.1558z^2 - 0.03707z + 0.6264)}{\{z^4 - 0.9407z^3 + (0.1558K_{cc} + 0.2419)z^2 - (0.03707K_{cc} + 0.3012)z + 0.6264K_{cc}\}} \tag{39}$$

where T_d is assumed to be one control period (T_s=100μs). The closed-loop root locus and open-loop impulse response of the converter-side current tracking scheme corresponding to the nominal system parameters is illustrated by Fig. 6*a*. It can be observed that the closed-loop system would be unstable when the current controller gain exceeds 9.91. It is worth noting that this stability margin is higher than the controller gain directly derived from the deadbeat control low. On the other hand, however, this gain is also higher than the stability margin obtained from the grid-side current tracking control scheme. Moreover, it can be observed from Fig. 6*a* that the open-loop impulse response shows an overshoot of 0.155 p.u with the response time of 1.2 millisecond.

Next, the influence of parameter variations is also rigorously studied herein by taking into account the variation of interfacing inductances, the control delay and the *RC*-filter parameter variations. Similar to the previous section, the influence of inductance variations is considered here by changing the grid-side inductance to 0.8 p.u and converter-side inductance to 1.2 p.u. Under this condition, the closed-loop transfer function in discrete domain can be derived as:

$$G_{c,close}(z)=\frac{K_{cc}(0.1801z^2-0.06898z+0.08171)}{\{z^4-0.9617z^3+(0.1801K_{cc}+0.2731)z^2 \\ -(0.06898K_{cc}+0.3114)z+0.08171K_{cc}\}} \tag{40}$$

The closed-loop root locus and open-loop impulse response of the converter-side current tracking scheme corresponding to inductance variations is illustrated by Fig. 6*b*. It can be observed that the closed-loop system would be unstable when the current controller gain exceeds 8.79, which is lower than the case of the nominal system parameters. Besides, it can be observed from Fig. 6*b* that the open-loop impulse response shows an overshoot of 0.18 p.u with the response time of 1.4 millisecond. Next, we consider the effect of control delay on the performance of the converter-side current tracking scheme. Similar to the previous section, here the control delay is considered to be $1.5T_s$; then the closed-loop transfer function of the current tracking algorithm is derived as:

$$G_{c,close}(z)=\frac{K_{cc}(0.08873z^3+0.0386z^2+0.02188z+0.3219)}{\{z^5-0.9407z^4+(0.08873K_{cc}+0.2419)z^3 \\ +(0.0386K_{cc}-0.3012)z^2+0.02188K_{cc}z+0.3219K_{cc}\}} \tag{41}$$

The closed-loop root locus and open-loop impulse response of the converter-side current tracking scheme corresponding to the variation of control delay is illustrated by Fig. 6*c*. It can be observed that the closed-loop system would be unstable when the current controller gain exceeds 7.48, which is lower than the case of the nominal system parameters. Besides, it can be observed from Fig. 6*c* that the open-loop impulse response shows an overshoot of 0.138 p.u with the response time of 1.2 millisecond, which exhibits lower overshoot than the case of the nominal system parameters. Next, we consider the effect of the *RC* filter parameters on the performance of the converter-side current control scheme by changing the filtering capacitance and the damping resistance, respectively. If the filtering capacitance of the *RC* filter is modified to C_d=5 μF, then the closed-loop transfer function of the converter-side current tracking control algorithm is derived as:

$$G_{c,close}(z)=\frac{K_{cc}(0.1305z^2+0.1468z+0.0373)}{\{z^4+0.05781z^3+(0.1305K_{cc}-0.7566)z^2 \\ +(0.1468K_{cc}-0.3012)z+0.0373K_{cc}\}} \tag{42}$$

The closed-loop root locus and open-loop impulse response of the converter-side current control scheme with the variation of filtering capacitance is illustrated by Fig. 6*d*. It can be observed that the closed-loop system would be unstable when the current controller gain exceeds 7.46, which is much higher than the case of the nominal system parameters. Moreover, it can be observed from Fig. 6*d* that the open-loop impulse response shows an overshoot of 0.14 p.u with the response time of 1.1 millisecond, which is remarkably lower than the case of the nominal system parameters. It is worth noting that, the smaller the filtering capacitance, the lower is the achieved stability margin of the current tracking control algorithm, which shows a phenomenon the reverse of the case of the grid-side current tracking control scheme. Next, the effect of the damping resistance on the closed-loop current tracking control is examined by changing the damping resistance R_d to 0.1 Ω, and then the closed-loop transfer function can be derived as:

$$G_{c,close}(z) = \frac{K_{cc}(0.1702z^2 - 0.3227z + 0.1624)}{\{z^4 - 0.6889z^3 + (0.1702K_{cc} + 0.6306)z^2 - (0.3227K_{cc} + 0.9418)z + 0.1624K_{cc}\}} \tag{43}$$

The closed-loop root locus plot and open-loop impulse response of the converter-side current tracking control scheme with the variation of damping resistance is illustrated by Fig. 6*e*. It can be observed that the closed-loop system shows multiple poles at the unit cycle of the root locus diagram, and the system would be unstable when the current controller gain exceeds 1.09, which is significantly lower than in the case of the nominal system parameters. Besides, it can be observed from Fig. 6*e* that the open-loop impulse response shows an overshoot of 0.185 p.u with the response time of 18 millisecond, which is significantly higher than in the case of nominal system parameters. It is found that smaller damping resistance would result in smaller stability margin and prolonged dynamic response of the converter-side current control scheme, which is consistent with the analysis in the previous section.

Table 3 shows a summary of the stability margin and dynamic response of the converter-side current tracking scheme, where the results obtained under the nominal system parameters and parameter variation scenarios are presented. It should be pointed out that the stability margins obtained from the converter-side current tracking control scheme are generally higher than those obtained from the grid-side current tracking scheme. However, the converter-side current tracking control scheme is rather sensitive to the variation of the damping resistance. Moreover, if the converter-side current tracking scheme is adopted, then the generation of the reference current would be rather complex since the impedance transfer function between the grid-side and converter-side current must be utilized (see Fig. 1), which would impose additional parameter uncertainty on the control system and complicate the problem. Therefore, the grid-side current tracking control is practically implemented, as reported in the simulation and experimental sections.

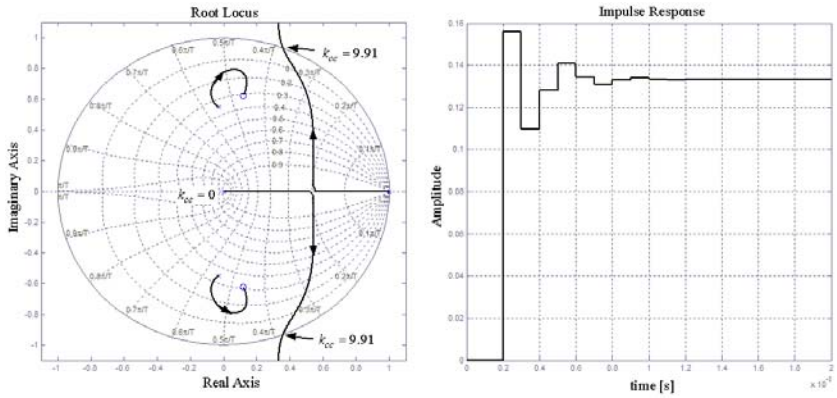
Root Locus
Imaginary Axis
Real Axis
$k_{cc} = 9.91$
$k_{cc} = 0$
$k_{cc} = 9.91$
Impulse Response
Amplitude
time [s]

(a)

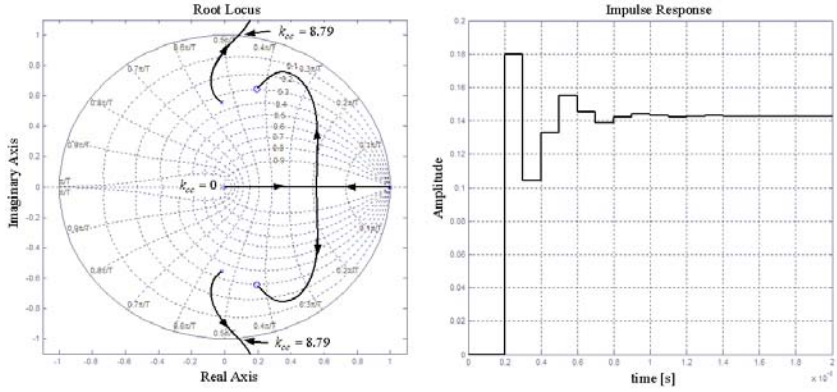
Root Locus
Imaginary Axis
Real Axis
$k_{cc} = 8.79$
$k_{cc} = 0$
$k_{cc} = 8.79$
Impulse Response
Amplitude
time [s]

(b)

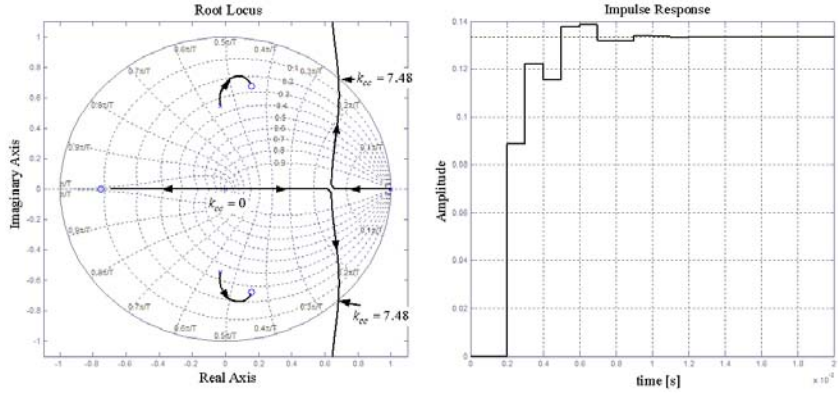
Root Locus
Imaginary Axis
Real Axis
$k_{cc} = 7.48$
$k_{cc} = 0$
$k_{cc} = 7.48$
Impulse Response
Amplitude
time [s]

(c)

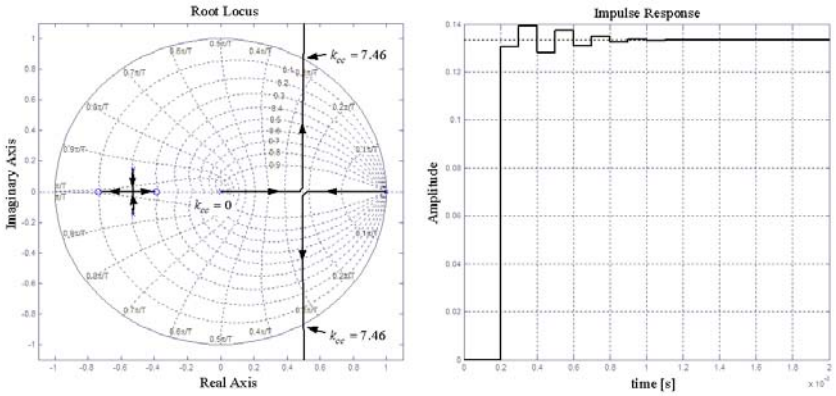

(d)

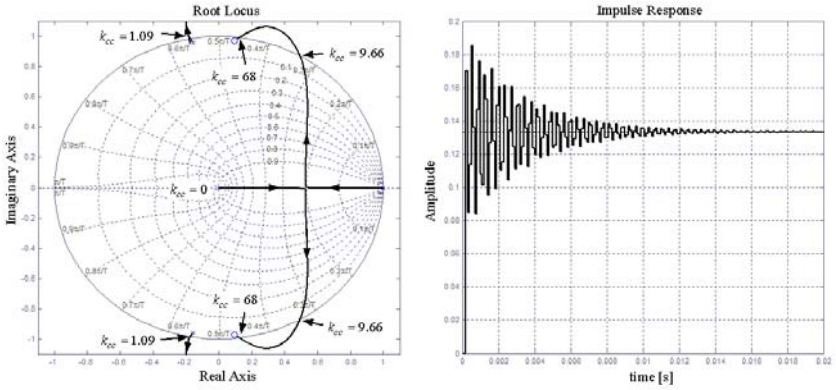

(e)

Figure 6

The closed-loop root locus diagrams and the open-loop impulse responses of the current regulation algorithm based on the converter-side current (i_c) tracking control scheme. (a) Root locus and impulse response under nominal parameters; (b) Root locus and impulse response under inductance variations; (c) Root locus and impulse response under different control delay (T_d=1.5T_s); (d). Root locus and impulse response under different *RC*-filter capacitance C_d; (e). Root locus and impulse response under different *RC*-filter resistance R_d

In the previous subsections, the closed-loop current tracking scheme was analyzed using root locus methodologies, and the grid-side current tracking scheme and the converter-side current tracking scheme are presented based on the mathematical model of the *LCL*-filter section. It can be noticed that the effect of the AC-side capacitor C_{ac} was not taken into account. Therefore, the effect of the AC-side capacitor will be presented in the forthcoming subsection, where this effect is compensated in the feed-forward loop.

Table 3
Summary of the stability margin and dynamic response of the converter-side current tracking scheme

Case	Marginal gain (deg)	Overshoot (pu)	Response time (ms)
1	9.91	0.155	1.2
2	8.79	0.18	1.4
3	7.48	0.138	1.2
4	7.46	0.14	1.1
5	1.09	0.185	18

3.2.4 Feed-Forward Loop for Load Disturbance Rejection

As is well known, the phase angle of the voltage drop across a capacitor is always a 90-degree lag of the current flowing into the capacitor, which is the basis for the forthcoming derivations. The APF compensating current can be denoted by using the grid-side current of the *LCL*-filter section:

$$\begin{aligned} i_{ga}(t) &= \sum_{n=1}^{N} I_{ga,n} \sin(n\omega_0 t + \varphi_{ga,n}) \\ &= I_{ga,1} \cos(\varphi_{ga,1} - \varphi_{PLL}) \sin(\omega_0 t + \varphi_{PLL}) + I_{ga,1} \sin(\varphi_{ga,1} - \varphi_{PLL}) \cos(\omega_0 t + \varphi_{PLL}) + \\ &\sum_{n=3}^{N} [I_{ga,n}.\cos\varphi_{ga,n} \sin(n\omega_0 t) + I_{ga,n}.\sin\varphi_{ga,n} \cos(n\omega_0 t)] \end{aligned} \tag{44}$$

where N represents the number of the highest harmonic component compensated by the APF. The voltage drop across the AC-side capacitor C_{ac} is represented as:

$$v_{Cac}(t) = \sum_{n=1}^{N} \frac{I_{ga,n}}{n\omega_0 C_{ac}} \sin(n\omega_0 t + \varphi_{ga,n} - \frac{\pi}{2}) \tag{45}$$

the feed-forward loop for the proposed APF can be easily derived by selecting the non-active component of the load current as the reference current in the feed-forward loop, which is represented as:

$$i_{ga,ff}^{ref}(t) = -\{b_{La,1} \cos(\omega_0 t + \varphi_{PLL}) + \sum_{n=3}^{N} [a_{La,n} \sin(n\omega_0 t) + b_{La,n} \cos(n\omega_0 t)]\} \tag{46}$$

Under this scenario, i.e., the non-active component of load-side current is utilized as the feed-forward current (note that the direction should be negative according to the positive direction of APF current defined in Fig. 1) besides, the active current of the VSI generated by the dc-voltage control loop would also have a voltage drop across the capacitor C_{ac}, then the virtual voltage drop across the AC-side capacitor C_{ac} can be denoted as:

$$v_{Cac,ff}^{ref}(t) = -\frac{1}{\omega_0 C_{ac}}(b_{La,1}\sin(\omega_0 t + \varphi_{PLL}) + \Delta I_p \cos(\omega_0 t + \varphi_{PLL})) - \sum_{n=3}^{N}\frac{1}{n\omega_0 C_{ac}}[b_{La,n}\sin(n\omega_0 t) - a_{La,n}\cos(n\omega_0 t)] \quad (47)$$

Hence the feed-forward control signal is obtained as:

$$t_d^{ff}[k] = \frac{\{v_{dc}[k] + v_{grid}[k] - v_{Cac,ff}^{ref}[k]\}T_s}{2v_{dc}[k]} \quad (48)$$

After the feed-forward signal is derived, Eq. (48) can be substituted into Eq. (25) to synthesize the total control signal.

3.3 Dc-Link Voltage Control

In order to ensure a smooth operation of the APF, the dc-link voltage is sensed by using a potential transducer (PT) and sent to the controller through the A/D channel, where the resetting filter is utilized as a pre-filter for the sampled dc-link voltage. The difference between the dc-link voltage and its reference is regulated by using a proportional-integral (PI) controller (k_i=0.1, k_p=0.6), and the output of the PI regulator is multiplied by a unit sinusoidal function synchronized to grid voltage by using a phase-locked-loop (PLL). The output of the dc-bus voltage regulator is set as the active current reference for the inner current loop (Fig. 3) and also utilized in the feed-forward loop. In addition, to ensure a smooth transient response in the dc-bus voltage, two limiters are used in the control loop, one at the output of the integrator and another at the output of the PI regulator.

4 Simulation Results and Discussions

This section presents the simulation results of the proposed hybrid APF under various parameter variations, including the grid voltage distortion, inductance variations and grid disturbance scenarios. The nominal parameters of the system are listed in Table 1. The thyristor rectifier load is used as a harmonic source, which consists of two anti-parallel connected thyristor switches with resistive load of 2.2 Ω. In order to test the dynamic performance of the presented system, a step change of load is applied by parallel connecting another 2.2 Ω resistor at the load-side of the thyristor switches. Fig. 7 shows the simulation results of the APF under ideal grid voltage and nominal inductances. Fig. 7*a* shows the load current i_L, the converter-side and grid-side currents of the hybrid APF (denoted by i_c and i_g), and the source-side current of the distribution system i_s.

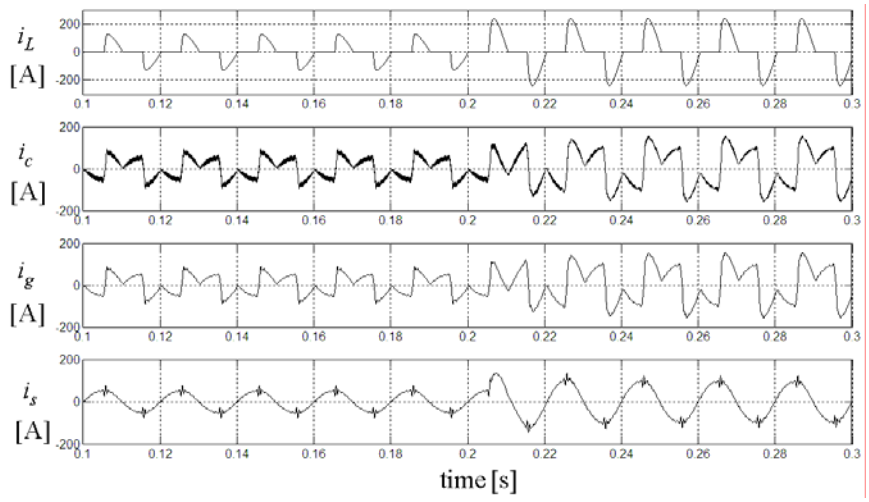

(a)

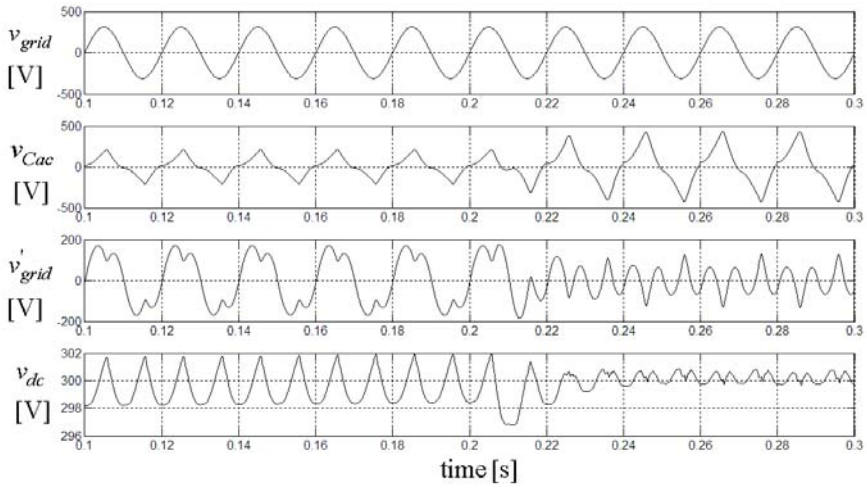

(b)

Figure 7

The simulation results of the hybrid *LCL*-filter based APF under ideal grid voltage and nominal inductances. (a) The load current i_L, the converter-side and grid-side currents of the hybrid APF (denoted by i_c and i_g), and the source-side current of the distribution system i_s. (b) The grid voltage v_{grid}, the AC capacitor voltage v_{Cac}, the voltage behind the AC capacitor v'_{grid}, and the dc-link voltage of the voltage source inverter v_{dc}

It can be observed that the nonlinear load current i_L, generated by the thyristor rectifier, is highly distorted with sharp rising and falling edges, i.e., a high *di*/*dt* ratio. This kind of load is rather difficult to compensate due to high *di*/*dt* ratio, which requires the compensating device to have sufficient bandwidth to cover the spectrum of the load harmonics. In case of the full compensation scheme, as reported in many previous literature sources [6, 9-12], if the APF were designed to compensate all the non-active component of the load-side current, this would result in ineffective compensation due to the limited current loop gain adopted to ensure the closed-loop stability. If the designer were to aim to improve the compensation performance of the total compensation scheme by increasing the current-loop gain, the system would be prone to be destabilized in the case of compensating a high *di*/*dt* ratio load with sharp rising and falling edges, such as the thyristor rectifier with resistive load considered herein.

Fig. 7*a* shows that the source-side current of the distribution system is sinusoidal and almost in phase with the grid voltage, and the sharp rising and falling edges of load current is well compensated. In addition, the dynamic response of the source-side current is also sufficiently fast when a sudden increase of load is applied at t=0.2s. The converter-side and grid-side currents of the APF (i_c and i_g) can also be observed in Fig. 7*a*, which shows that the high frequency switching ripples in the converter-side current i_c is filtered out by the *RC*-filter hence the injection current i_g is almost ripple free. Fig. 7*b* shows the grid voltage at the common coupling point (PCC), AC capacitor voltage, the voltage behind the AC capacitor (or the virtual grid voltage), and the dc-link voltage of the VSI, denoted by v_{grid}, v_{Cac}, v'_{grid} and v_{dc}, respectively. It shows that the capacitor voltage v_{Cac} and the virtual grid voltage v'_{grid} are highly distorted due to the nonlinear compensating current generated by the VSI.

Additionally, it is interesting to notice that the capacitor voltage v_{Cac} undergoes a step increase when the transient increase of load is applied, while the virtual grid voltage, denoted by v'_{grid}, undergoes a decrease of amplitude. Moreover, voltage fluctuation in the dc-link voltage decreases from 4V to 1V when a sudden increase of load is applied. This phenomenon is fundamentally different from the conventional APF with *L*-filter or *LCL*-filter as interfacing inductance [27], where the dc-link voltage fluctuation would increase when a step load increase is applied. In the present case, the reduced dc-link fluctuation is mainly due to the reduction of the virtual grid voltage v'_{grid} after a step increase of load is applied, which shows that the dc-link voltage regulation works more effectively under heavy load for the proposed system.

Fig. 8 shows the simulation results of the proposed hybrid APF under non-ideal grid voltage and inductance variation scenario. It shows that the performance is almost same as in the case of the nominal inductance. However, the only

difference can be observed from Fig. 8*a*, where the source-side current i_s shows a little oscillation at the rising and falling edges of the nonlinear load current. This phenomenon, as stated previously, can be easily attenuated by reducing the current-loop gain. In addition, Fig. 8*b* shows that the grid voltage, AC capacitor voltage, voltage behind the AC capacitor, and dc-link voltage of the VSI are almost the same as in the case under nominal inductance scenario.

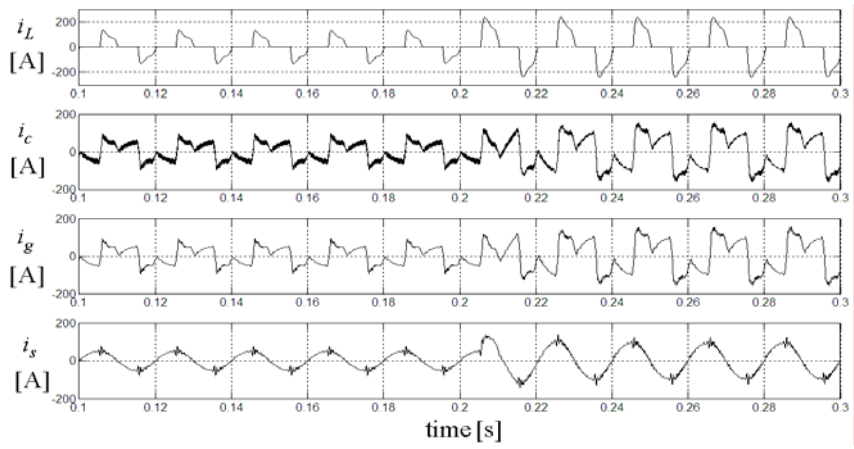

(a)

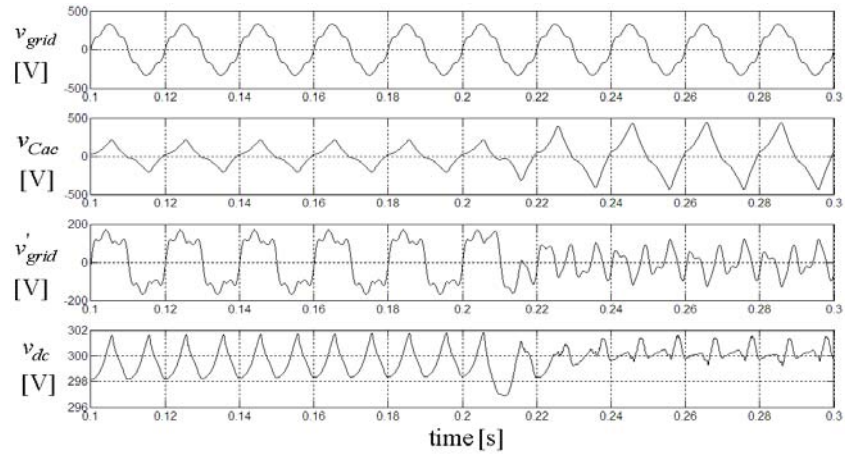

(b)

Figure 8

The simulation results of the hybrid *LCL*-filter based APF under non-ideal grid voltage and inductance variations. (a) The load current i_L, the converter-side and grid-side currents of the hybrid APF (denoted by i_c and i_g), and the source-side current of the distribution system i_s. (b) The grid voltage v_{grid}, the AC capacitor voltage v_{Cac}, the voltage behind the AC capacitor v'_{grid}, and the dc-link voltage of the voltage source inverter v_{dc}

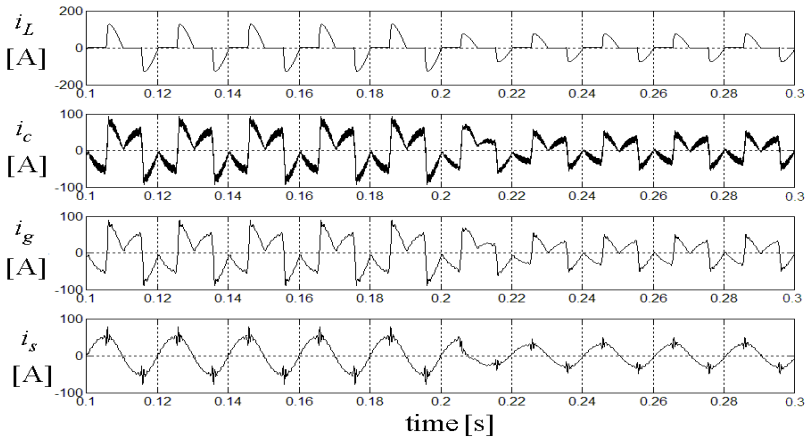

(a)

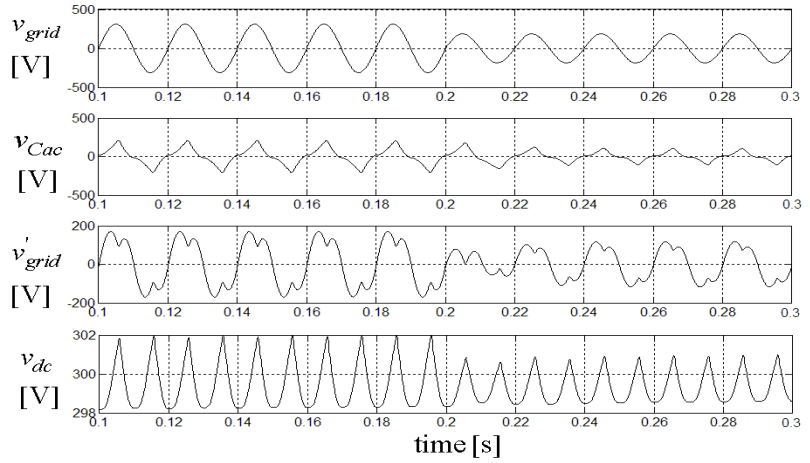

(b)

Figure 9

The simulation results of the hybrid *LCL*-filter based APF under voltage sag. (a) The load current i_L, the converter-side and grid-side currents of the hybrid APF (denoted by i_c and i_g), and the source-side current of the distribution system i_s. (b) The grid voltage v_{grid}, the AC capacitor voltage v_{Cac}, the voltage behind the AC capacitor v'_{grid}, and the dc-link voltage of the voltage source inverter v_{dc}

Fig. 9 shows the performance of the proposed APF under voltage sag of 0.4 p.u; it shows that the load current reduces significantly when the voltage sag occurs at t=0.2 s. Consequently, the compensating current, either the converter-side current i_c or the grid-side current i_g of the *LCL*-filter section, also undergoes remarkable reduction in magnitude. Further, it can be observed from Fig. 9*a* that the source-

side current shows a satisfactory result with excellent sinusoidal wave shape, with a transient response of less than one fundamental cycle. Fig. 9*b* also shows that the AC capacitor voltage v_{Cac} undergoes a reduction in magnitude when voltage sag occurs, and lower voltage ripple is achieved at the dc-link of the VSI due to the reduction in the compensating current. It can be concluded from the simulation results that a stable operation of the proposed APF is achieved with excellent steady state and dynamic response under parameter variations and grid perturbations, which validates the robustness and effectiveness of the proposed hybrid APF and its control strategies.

5 Experimental Results

In order to further verify the performance of the proposed APF, a hardware prototype system was built in the laboratory using three single-phase VSI topologies. Fig. 10 shows the software architectures of the devised control scheme for the proposed hybrid *LCL*-filter based APF. Three digital signal processors from Texas Instrument[1] (TMS3202812) are adopted in the prototype system. The main controller is responsible for execution of main program, soft-start routine, and protection routine. The auxiliary controller is used specifically for ADALINE-based harmonic extraction algorithm. The third DSP is used for man/machine interface, i.e., parameter display and touch board. The field programmable gate array (FPGA) from Altera[2] (EP1C6Q240C8) is used to receive gating signals from main controller and generate PWM signals for the insulated gate bipolar transistors (IGBTs). In addition, the FPGA also serves as the digital I/O to generate trigger signals for the soft-start circuit, the circuit breaker and other protection circuitry. The insulated gate bipolar transistors (IGBTs) from Semikron[3] are adopted as the power electronic switches for the voltage source inverters.

It should be pointed out that commercial fixed point digital signal processors (DSP), such as TI TMS320F2812, show the characteristic of sequential sampling of the input analog signals. This feature, however, may deteriorate the performance for the APF when real time compensation is required. In order to achieve simultaneous sampling of the analog signals, i.e., the synchronous sampling, the field programmable gate array (FPGA) is adopted as the interface for the two DSPs. In other words, the FPGA serves as the bi-directional random access memory (RAM) for the master and slave DSPs. As shown in Fig. 10, the grid voltages, AC capacitor voltages and the dc-link voltages of the three voltage

[1] Trademark—website: www.ti.com
[2] Trademark—website: www.altera.com
[3] Trademark—website: www.semikron.com

source inverters (VSIs) are obtained from the potential transducers (PTs), and the compensating currents of the APF and the source side currents are obtained from the current transducers (CTs). The fifteen channel signals are preprocessed by the proposed resetting filters, and then sampled by the AD8364 microchips and transmitted to the master DSP. The slave DSP is responsible for the harmonic decomposition of the proposed ADALINE estimation scheme for individual phase. Fig. 10 also shows that the third DSP is adopted to control the touch board and display panel. However, the hardware and control algorithm of the touch board is beyond the scope of this paper and hence it will not be discussed further.

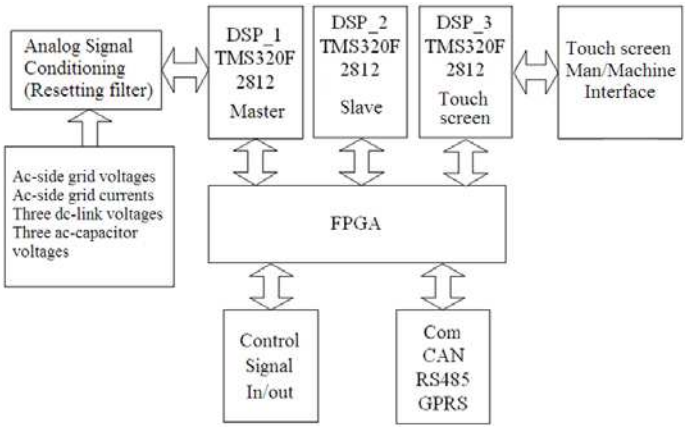

Figure 10
The software architectures of the master/slave digital signal processors and the field programmable gate array for implementation of the proposed control scheme

Fig. 11 shows the steady state experimental results in phase 'A' when the firing angle of the thyristor load is 90 degrees. The total harmonic distortion (THD) of the load current is 75%, which is highly distorted by characteristic harmonics components, such as the 3^{rd}, 5^{th}, 7^{th} and 11^{th} order harmonic components. However, after compensation by the proposed APF, the grid side current shows an excellent sinusoidal waveform, with a distortion of about 13%, which is much less than the load side distortion. In addition, the grid current is almost in phase with the grid voltage, with a power factor of about 0.95. Fig. 11b also shows the waveform of the dc-link voltage, which is consistent with that of the simulation results, with the amplitude of about 300 V.

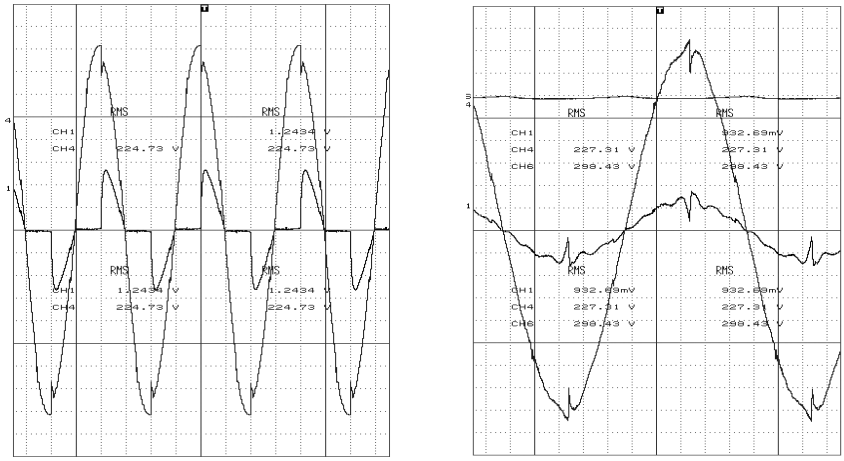

(a) (b)

Figure 11

The experimental results of the APF in phase 'A' with thyristor rectifier load when firing angle=90°. (a) The grid current and voltage (ch-1: 80 A/div, ch-4:40 V/div, X-axis:5 ms/div); (b) The grid current i_{sa} (ch-1: 80 A/div) and the APF dc-link voltage $v_{dc,A}$(ch-3:20 V/div, X-axis:2 ms/div)

Fig.12 shows the load side currents in phase 'A', 'B', 'C', as well as the neutral wire current, and the FFT spectrum of the currents in phase 'B' and 'C'. It can be observed that the load currents are highly distorted and each phase shows a phase shift of 120 degrees. And the neutral wire current is characterized by the 3N (N is integer) order harmonics.

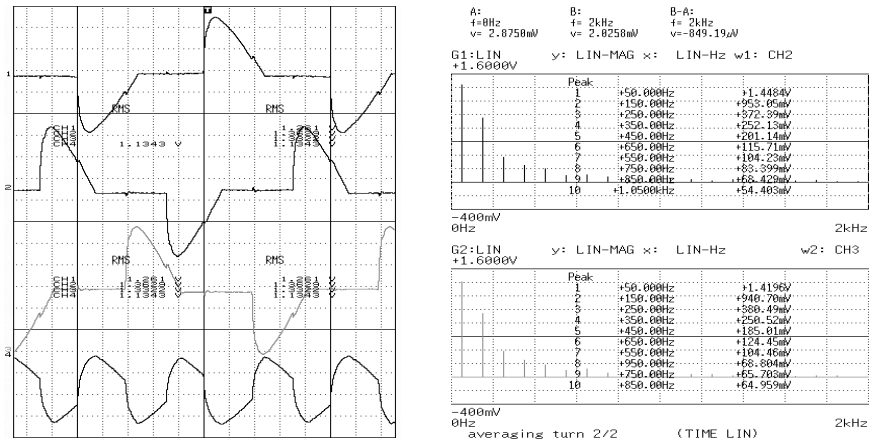

(a) (b)

Figure 12

Experimental results of the three single-phase thyristor load when firing angle=90°. (a) The load currents i_{La}, i_{Lb}, i_{Lc}, i_{LN} (ch-1 to ch-4: 80A/div, X-axis: 2ms/div); (b) The FFT spectrum of i_{Lb}, i_{Lc}

After the APF is switched on, it can be observed from Fig. 13 that the grid side currents are almost sinusoidal. In addition, the neural wire current is also well compensated and the 3 N (N is integer) order harmonics are almost eliminated.

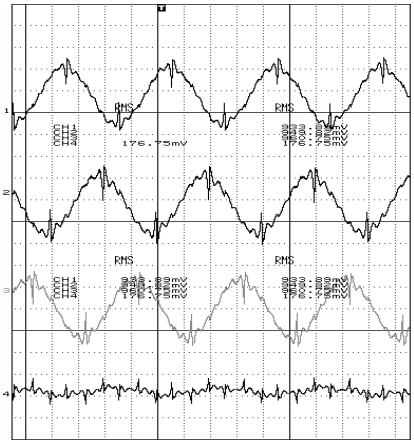

(a)

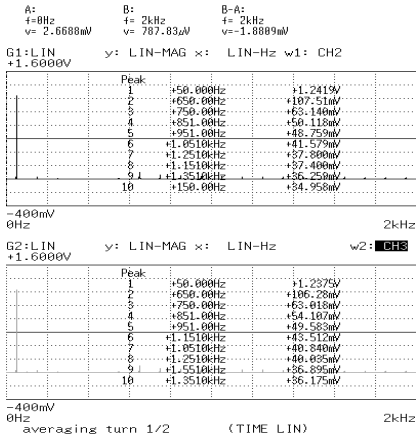

(b)

Figure 13

Experimental results of the grid currents after compensation when firing angle=90°. (a) The load currents i_{sa}, i_{sb}, i_{sc}, i_{sN} (ch-1 to ch-4: 80 A/div, X-axis: 5 ms/div); (b) The FFT spectrum of i_{sb}, i_{sc}

The experimental results illustrated by Figs. 11-13 indicate that the proposed hybrid APF is quite effective for compensating the nonlinear load current with sharp rising and falling edges. The three single-phase topologies of the hybrid APF provides flexible solutions for harmonic and reactive compensation of the three-phase balanced or unbalanced nonlinear load. The consistency between the simulation and experimental results verifies the effectiveness and robustness of the proposed control scheme.

Conclusions

This paper proposes a new APF topology, using the single-phase hybrid *LCL*-filter as the building block. The proposed hybrid APF shows the advantage of the conventional hybrid APF in the sense that the dc-link voltage of the voltage source inverter is significantly reduced compared to the pure APF based on the *L*-filter or *LCL*-filter as the interfacing impedance between the inverter and the grid.

The mathematical modeling of the hybrid APF is presented by using state-space representations. The feed-forward and feedback control scheme is proposed to ensure precise steady-state and dynamic performance of the APF. To reduce the controller bandwidth, the selective harmonic compensation scheme is adopted by using the well-known adaptive linear neural networks. Therefore, the interested harmonics are selected to be compensated to limit the controller bandwidth, thus ensuring the stability of the closed-loop current tracking algorithm.

To verify the effectiveness of the proposed APF, extensive simulation results obtained from Matlab/Simulink are provided under parameter variations and grid voltage disturbances. It is demonstrated by the simulation results that satisfactory compensation is achieved by using the proposed ADALINE-based feed-forward and feedback control strategies. A laboratory prototype system is also built. The digital signal processors (DSPs) and field programmable gate array (FPGA) are utilized as the main controller to implement the control strategies. The feasibility and effectiveness of the proposed APF is substantially confirmed by digital simulation and experimental results obtained from the laboratory prototype system.

References

[1] B. Oral, F. Donmez, The Impact of Natural Disasters on Power Systems: Anatomy of Marmara Earthquake Blackout, Acta Polytechnica Hungarica, Vol. 7, No. 2, pp. 107-118, 2010

[2] Y. Han, M. M. Khan, G. Yao, L. Zhou, C. Chen, Power Quality Enhancement for Automobile Factory Electrical Distribution System-Strategies and Field Practice, Przegląd Elektrotechniczny, 2009, 85(6): 159-163

[3] M Cirrincione, M. Pucci, G. Vitale, A. Miraoui, Current Harmonic Compensation by a Single-Phase Active Power Filter Controlled by Adaptive Neural Filtering, IEEE Trans. on Ind. Electron., Vol. 56, No. 8, pp. 3128-3143, Aug. 2009

[4] Recommended Practices and Requirements for Harmonics Control in Electrical Power Systems, IEEE-519, 1993

[5] Limits for Harmonic Current Emissions (Equipment Input Current up to and Including 16A Per Phase), IEC 61000-3-2 International Standard, 2000

[6] Y. Han, M. M. Khan, G. Yao, L. Zhou, C. Chen, A Novel Harmonic-Free Power Factor Corrector Based on T-type APF with Adaptive Linear Neural Network (ADALINE) Control, Simulation Modeling Practice and Theory, 2008, 16(10): 1215-1238

[7] Y. Han, M. M. Khan, G.Yao, L. Zhou, C. Chen, State-Space Averaging (SSA) Technique for Modeling of the Cascaded H-Bridge Multilevel DSTATCOMs and Active Filters, International Review of Electrical Engineering-IREE, 2009, 4(5):744-760

[8] Y. Han, M. M. Khan, G. Yao, L. Zhou, C. Chen, A Novel Modulation Scheme for DC-Voltage Balancing Control of Cascaded H-Bridge Multilevel APF, Przegląd Elektrotechniczny, 2009, 85(5): 81-85

[9] Y. Han, M. M. Khan, G. Yao, L. Zhou, C. Chen, Flicker Mitigation of Arc Furnace Load Using Modified *p-q-r* Method, Przegląd Elektrotechniczny, 2009, 85(1): 225-229

[10] Y. Komatsu, T. Kawabata, Experimental Comparison of p-q and Extended p-q Method for Active Power Filter, in Proc. EPE, pp. 2.729-2.734

[11] I. Etxeberria-Otadui, A. L. D. Heredia, H. Gaztanaga, S. Bacha, M. Reyero, A Single Synchronous Frame Hybrid (ssfh) Multifrequency Controller for Power Active Filters, IEEE Trans. Ind. Electron., 53(5) (2006) 1640-1648

[12] G. D. Marques, A Comparison of Active Power Filter Control Methods in Unbalanced and Non-Sinusoidal Conditions, Proc. IEEE IECON, pp. 444-449, 1998

[13] B. Singh, K. Al-Haddad, A. Chandra, A New Control Approach to Three-Phase Active Filter for Harmonics and Reactive Power Compensation, IEEE Trans. Power Syst., 13(1) (1998) 133-138

[14] S. Dalapati, C. Chakraborty, Dynamic Performance of a Dead-Band Controlled Capacitor Charging Type Inverter, Simulat. Model Pract. Theor., 17(5)(2009) 911-934

[15] S. A. González, R. García-Retegui, M. Benedetti, Harmonic Computation Technique Suitable for Active Power Filters, IEEE Trans. Ind. Electron., 54(5) (2007) 2791-2796

[16] R. Taleb, A. Meroufel, P. Wira, Control of a Uniform Step Asymmetrical 9-level Inverter Based on Artificial Neural Network Strategy, Acta Polytechnica Hungarica, Vol. 6, No. 4, pp. 137-156, 2009

[17] Y. Han, M. M. Khan, G. Yao, L. Zhou, C. Chen, The Adaptive Signal Processing Scheme for Power Quality Conditioning Applications Based on Active Noise Control (ANC), Elektronika Ir Elektrotechnika, 2009(8):9-14

[18] D. O. Abdeslam, P. Wira, J. Merckle, D. Flieller, Y.-A. Chapuis, A Unified Artificial Neural Network Architecture for Active Power Filters, IEEE Trans. Ind. Electron., 54(1) (2007) 61-76

[19] M. Cirrincione, M. Pucci, G. Vitale, A Single-Phase DG Generation unit with Shunt Active Power Filter Capability by Adaptive Neural Filtering, IEEE Trans. Ind. Electron., 55(5) (2008) 2093-2110

[20] M. El-Habrouk, M. K. Darwish, A New Control Technique for Active Power Filters Using a Combined Genetic Algorithm/Conventional Analysis, IEEE Trans. Ind. Electron., 49(1) (2002)58-66

[21] Y. A.-R. I. Mohamed, E. F. El-Saadany, A Control Scheme for PWM Voltage-Source Distributed-Generation Inverters for Fast Load-Voltage Regulation and Effective Mitigation of Unbalanced Voltage Disturbances, IEEE Trans. Ind. Electron., 55(5)(2008) 2072-2084

[22] H. Akagi, Y. Kanazawa, A. Nabae, Instantaneous Reactive Power Compensators Comprising Switching Devices without Energy Storage, IEEE Trans. Ind. Appl., 20(3) (1984) 625-630

[23] S. Vazquez, J. A. Sanchez, J. M. Carrasco, J. I. Leon, E. Galvan, A Model-based Direct Power Control for Three-Phase Power Converters, IEEE Trans. Ind. Appl., 55(4) (2008)1647-1657

[24] R. Griñó, R. Cardoner, R. Costa-Castelló, E. Fossas, Digital Repetive Control of a Three-Phase Four-Wire Shunt Active Filter, IEEE Trans. Ind. Electron., 54 (3) (2007) 1495-1503

[25] M. Castilla, J. Miret, J. Matas, et al., Linear Current Control Scheme with Series Resonant Harmonic Compensator for Single-Phase Grid-connected Photovoltaic Inverters, IEEE Trans. Ind. Electron., 55(7)(2008)2724-2733

[26] K. K. Shyu, M. J. Yang, Y. M. Chen, Y. F. Lin, Model Reference Adaptive Control Design for a Shunt Active-Power-Filter System, IEEE Trans. Ind. Electron., 55(7)(2008)97-106

[27] Y. Han, M. M. Khan, G. Yao, L. Zhou, C. Chen, A Robust Deadbeat Control Scheme for Active Power Filter with LCL Input Filter, Przegląd Elektrotechniczny, 2010, 86(2): 14-19

[28] B. Singh, J. Solanki, An Implementation of an Adaptive Control Algorithm for a Three-Phase Shunt Active Filter, IEEE Trans. on Ind. Electron.,Vol. 56, No. 8, pp. 2811-2820, Aug. 2009

[29] Y. Han, L. Xu, M. M. Khan, G. Yao, L. Zhou, C. Chen, A Novel Synchronization Scheme for Grid-connected Converters by Using Adaptive Linear Optimal Filter Based PLL (ALOF-PLL), Simulation Modeling Practice and Theory, 2009, 17(7): 1299-1345

[30] Satish Kumar, Neural Networks, McGraw-Hill Education (Asia) Co. and Tsinghua University Press, 2006

[31] K. Masoud, G. Ledwich, Sampling Averaging for Inverter Control, IEEE 33rd Annual Power Electronics Specialists Conference, Vol. 4, 2002, pp. 1699-1704

Testing the Coarse Alignment Algorithm Using Rotation Platform

Milos Sotak

Department of Electronics
Armed Forces Academy
Demanova 393, 031 06 Liptovsky Mikulas 6, Slovakia
milos.sotak@gmail.com

Abstract: The paper deals with testing the coarse alignment algorithm for the inertial measurement unit ADIS16405 using a rotation platform. The ADIS16405 is the new six-degree of freedom inertial measurement unit which is being produced by Analog Devices. The main goal of the paper is to describe the determination of the initial attitude of the inertial measurement unit with respect to the navigation frame as a referenced frame and to depict appropriate tests using a rotation platform. In this work the attitude is represented by the Euler angles (the roll, pitch and yaw angles). The tests were conducted using the INS/GNSS development kit which had been mounted on the rotation platform. The overall factual results are illustrated and correctness of the algorithm was definitely confirmed.

Keywords: alignment algorithm; attitude; inertial measurement unit; navigation

1 Introduction

The Inertial Measurement Unit (IMU) typically provides an output of a vehicle's accelerations and angular rates, which are then integrated to obtain the vehicle's position, velocity, and attitude. The system providing this information is called an Inertial Navigation System (INS). Over the last decades there has been a remarkable increase in demand for low-cost inertial navigation systems to serve in car navigation, personal navigation, indoor navigation, the navigation of Unmanned Aerial Vehicles (UAVs), etc. Recent technological progress in the precision and reliability of micro-electro-mechanical systems (MEMS) has remarkably affected the area of low-cost INS [13, 14, 15, 16]. The operation of an inertial navigation system follows the laws of classical mechanics as formulated by Newton. The ability to measure specific forces using accelerometers allows for calculating changes in velocity and position by performing successive integration of the acceleration with respect to time [4]. To function properly, the INS must be initialized when turned on by an initialization procedure containing an alignment

procedure which determines the initial attitude [3, 17]. The initial attitude is understood as setting up the initial Euler angles (the roll, pitch and yaw angles) which express the relationship between the navigation frame as the reference frame and the body frame as the frame where the inertial measurement unit is mounted. Low-cost inertial measurement units contain three-axis accelerometers, three-axis gyroscopes and three-axis magnetometers. The reason for the implementation of magnetometers into this configuration is that the low quality of gyroscopes in the low-cost inertial measurement units does not allow for the performance of the so-called self-alignment. Self-alignment stands for the capability to determine the initial attitude without external sources.

2 Transformation Matrix and Euler Angles

The relationship between vectors in the navigation frame (as a reference frame) and the body frame are completely described by the transformation matrix $\boldsymbol{C}_{\mathrm{n}}^{\mathrm{b}}$ [3, 5, 6, 8]. The $\boldsymbol{C}_{\mathrm{n}}^{\mathrm{b}}$ is defined by the sequence of three rotations of the planes $[\phi]_1, [\theta]_2, [\psi]_3$ comprising Euler angles ϕ, θ, ψ and can be calculated

$$\boldsymbol{C}_{\mathrm{n}}^{\mathrm{b}} = [\phi]_1 \cdot [\theta]_2 \cdot [\psi]_3 , \tag{1}$$

where

$$[\phi]_1 = \begin{bmatrix} 1 & 0 & 0 \\ 0 & \cos\phi & \sin\phi \\ 0 & -\sin\phi & \cos\phi \end{bmatrix}, \tag{2}$$

$$[\theta]_2 = \begin{bmatrix} \cos\theta & 0 & \sin\theta \\ 0 & 1 & 0 \\ -\sin\theta & 0 & \cos\theta \end{bmatrix}, \tag{3}$$

$$[\psi]_3 = \begin{bmatrix} \cos\psi & \sin\psi & 0 \\ -\sin\psi & \cos\psi & 0 \\ 0 & 0 & 1 \end{bmatrix}, \tag{4}$$

where ϕ, θ and ψ represent the roll, pitch and yaw angles. Substituting equations (2), (3) and (4) in the equation (1) can be expressed as the transformation matrix $\boldsymbol{C}_{\mathrm{n}}^{\mathrm{b}}$ in the following way

$$\boldsymbol{C}_{\mathrm{n}}^{\mathrm{b}} = \begin{bmatrix} \cos\psi\cos\theta & \sin\psi\cos\theta & -\sin\theta \\ \begin{pmatrix}\cos\psi\sin\theta\sin\phi \\ -\sin\psi\cos\phi\end{pmatrix} & \begin{pmatrix}\sin\psi\sin\theta\sin\phi \\ +\cos\psi\cos\phi\end{pmatrix} & \cos\theta\sin\phi \\ \begin{pmatrix}\cos\psi\sin\theta\cos\phi \\ +\sin\psi\sin\phi\end{pmatrix} & \begin{pmatrix}\sin\psi\sin\theta\cos\phi \\ -\cos\psi\sin\phi\end{pmatrix} & \cos\theta\cos\phi \end{bmatrix}. \tag{5}$$

Due to the fact that transformation matrix is orthogonal [3, 4, 7, 9], an inverse transformation from the body frame to navigation frame can be calculated as following

$$\boldsymbol{C}_{\mathrm{b}}^{\mathrm{n}} = \left[\boldsymbol{C}_{\mathrm{n}}^{\mathrm{b}}\right]^{\mathrm{T}} = \left[\psi\right]_{3}^{\mathrm{T}} \cdot \left[\theta\right]_{2}^{\mathrm{T}} \cdot \left[\phi\right]_{1}^{\mathrm{T}}. \tag{6}$$

3 Coarse Alignment Algorithm

As mentioned above, the goal of the alignment procedure is to determine the initial attitude of the inertial navigation system. Due to the fact that the IMU ADIS16405 consists of three-axis accelerometers, three-axis gyroscopes and three-axis magnetometers, the self-alignment can be achieved easily. Therefore, it isn't necessary to use any information from other systems to determine the initial attitude. The coarse alignment algorithm can be split into two parts. The first step of the coarse alignment algorithm is called leveling and the second step is called course alignment.

3.1 Leveling

The goal of leveling is to determine the roll angle ϕ and the pitch angle θ between the navigation frame and the body frame. Typically, the orientation of the navigation frame is defined as *x*-axis towards north, *y*-axis towards to the east and *z*-axis towards down [3, 6, 11]. Therefore, this notification is denoted as a NED (North, East, Down) direction and the axes of navigation frame are denoted as $\left[\mathrm{x}_{\mathrm{NED}}^{\mathrm{n}}, \mathrm{y}_{\mathrm{NED}}^{\mathrm{n}}, \mathrm{z}_{\mathrm{NED}}^{\mathrm{n}}\right]$ and the vectors of accelerations are expressed in the navigation frame as $\boldsymbol{a}_{\mathrm{NED}}^{\mathrm{n}} = \left[\mathrm{a}_{\mathrm{NED}}^{\mathrm{nx}}, \mathrm{a}_{\mathrm{NED}}^{\mathrm{ny}}, \mathrm{a}_{\mathrm{NED}}^{\mathrm{nz}}\right]^{\mathrm{T}}$. The measured outputs of accelerometers represent the specific forces, expressed in the body frame as the components of vector $\boldsymbol{f}_{\mathrm{ADIS}}^{\mathrm{b}} = \left[\mathrm{f}_{\mathrm{ADIS}}^{\mathrm{bx}}, \mathrm{f}_{\mathrm{ADIS}}^{\mathrm{by}}, \mathrm{f}_{\mathrm{ADIS}}^{\mathrm{bz}}\right]^{\mathrm{T}}$. In the Fig. 3 the ADIS16405 sensor is illustrated with the sensors axes orientation defined. It is clear that the accelerometers axes are in the opposite direction of the axes of magnetometers and

the axes of gyroscopes. Therefore, it is suitable to transform the outputs of the accelerometers to the opposite direction. Typically in navigation for the reference frame it is preferable to express the sensor outputs in the same direction as in the navigation frame axes direction (under the condition that the roll, pitch and yaw angles are equal to zero; it means the navigation frame is coincident with the body frame). It can be done by the transformation matrix $\boldsymbol{C}_{\mathrm{ADIS}}^{\mathrm{ADISinNAV}}$.

The mentioned transformation can be written as

$$\boldsymbol{f}_{\mathrm{ADISinNAV}}^{\mathrm{b}} = \boldsymbol{C}_{\mathrm{ADIS}}^{\mathrm{ADISinNAV}} \cdot \left(-\boldsymbol{f}_{\mathrm{ADIS}}^{\mathrm{b}}\right), \tag{7}$$

or

$$\begin{bmatrix} \mathrm{f}_{\mathrm{ADISinNAV}}^{\mathrm{bx}} \\ \mathrm{f}_{\mathrm{ADISinNAV}}^{\mathrm{by}} \\ \mathrm{f}_{\mathrm{ADISinNAV}}^{\mathrm{bz}} \end{bmatrix} = \begin{bmatrix} 0 & 1 & 0 \\ 1 & 0 & 0 \\ 0 & 0 & -1 \end{bmatrix} \cdot \begin{bmatrix} -\mathrm{f}_{\mathrm{ADIS}}^{\mathrm{bx}} \\ -\mathrm{f}_{\mathrm{ADIS}}^{\mathrm{by}} \\ -\mathrm{f}_{\mathrm{ADIS}}^{\mathrm{bz}} \end{bmatrix}. \tag{8}$$

In general, the specific force vector is defined as

$$\boldsymbol{f}_{\mathrm{ADISinNAV}}^{\mathrm{b}} = \boldsymbol{a}_{\mathrm{ADISinNAV}}^{\mathrm{b}} - \boldsymbol{g}^{\mathrm{b}}, \tag{9}$$

where vector $\boldsymbol{a}_{\mathrm{ADISinNAV}}^{\mathrm{b}}$ is represented as an acceleration of the body frame relative to the inertial frame. Assuming the alignment procedure of the ADIS16405 is stationary, the $\boldsymbol{a}_{\mathrm{ADISinNAV}}^{\mathrm{b}} = 0$ so equation (3) can be rewritten

$$\boldsymbol{f}_{\mathrm{ADISinNAV}}^{\mathrm{b}} = -\boldsymbol{g}^{\mathrm{b}}. \tag{10}$$

Let $\boldsymbol{g}^{\mathrm{b}}$ be the gravity vector in the body frame, and taken that the sensor position on the Earth is known, according to this, the gravity in the navigation frame can be computed [6] as

$$\boldsymbol{g}^{\mathrm{n}} = \begin{bmatrix} 0 \\ 0 \\ 9.7803267715 \frac{1+0.001931851353\sin^2(\varphi)}{\sqrt{1-0.0066943800299\sin^2(\varphi)}} \end{bmatrix}, \tag{11}$$

where φ is the latitude.

If the sensor position is unknown, then

$$\boldsymbol{g}^{\mathrm{n}} = \begin{bmatrix} 0 \\ 0 \\ \mathrm{g}_{\mathrm{e}} \end{bmatrix}, \tag{12}$$

where $g_e = 9.80665\ \mathrm{m.s^{-2}}$ is the Earth gravity constant. The relationship between the gravity vector in the body frame and navigation frame can be expressed as

$$\boldsymbol{g}^{b} = \boldsymbol{C}_{n}^{b} \cdot \boldsymbol{g}^{n}, \tag{13}$$

or

$$\boldsymbol{g}^{b} = \begin{bmatrix} -\sin\theta \\ \cos\theta\sin\phi \\ \cos\theta\cos\phi \end{bmatrix} \cdot g_e . \tag{14}$$

Substituting equation (14) into equation (10) can be rewritten as

$$\begin{bmatrix} f_{ADISinNAV}^{bx} \\ f_{ADISinNAV}^{by} \\ f_{ADISinNAV}^{bz} \end{bmatrix} = -\begin{bmatrix} -\sin\theta \\ \cos\theta\sin\phi \\ \cos\theta\cos\phi \end{bmatrix} \cdot g_e . \tag{15}$$

In the Fig. 1, the determination of roll angle ϕ is illustrated. The outputs of *x* and *z* accelerometers are $f_{ADIS}^{bx} = 0.31g$, $f_{ADIS}^{bz} = -0.95g$ or, applying the equation (7), they are $f_{ADISinNAV}^{by} = -0.31g$ and $f_{ADISinNAV}^{bz} = -0.95g$. It is depicted in the upper part of Fig. 1 which is denoted as "ADIS16405 in *x*-*z* plane". From the equation (15), the roll angle can be computed as

$$\phi = \operatorname{atan2}\left(-f_{ADISinNAV}^{by}, -f_{ADISinNAV}^{bz}\right), \tag{16}$$

So the values of specific forces can be substituted as following

$$\phi = \operatorname{atan2}\left(-(-0.31g), -(-0.95g)\right) = 18^{\circ}. \tag{17}$$

Using direct outputs from the accelerometers

$$\phi = \operatorname{atan2}\left(f_{ADIS}^{bx}, -f_{ADIS}^{bz}\right). \tag{18}$$

When the measured values of specific forces are substituted we can get following

$$\phi = \operatorname{atan2}\left(0.31g, -(-0.95g)\right) = 18^{\circ}. \tag{19}$$

For the roll angle determination in all four quadrants it is necessary to use the *atan2* function. Due to the correct determination of roll in all four quadrants, the correct expression of the parameters is very important. Therefore, in the bottom part of Fig. 1, which is denoted as "function *atan2* in plane", the transformation of accelerometers outputs in ADIS16405 *x*-*z* plane to the *x*-*y* plane for *atan2* function is illustrated.

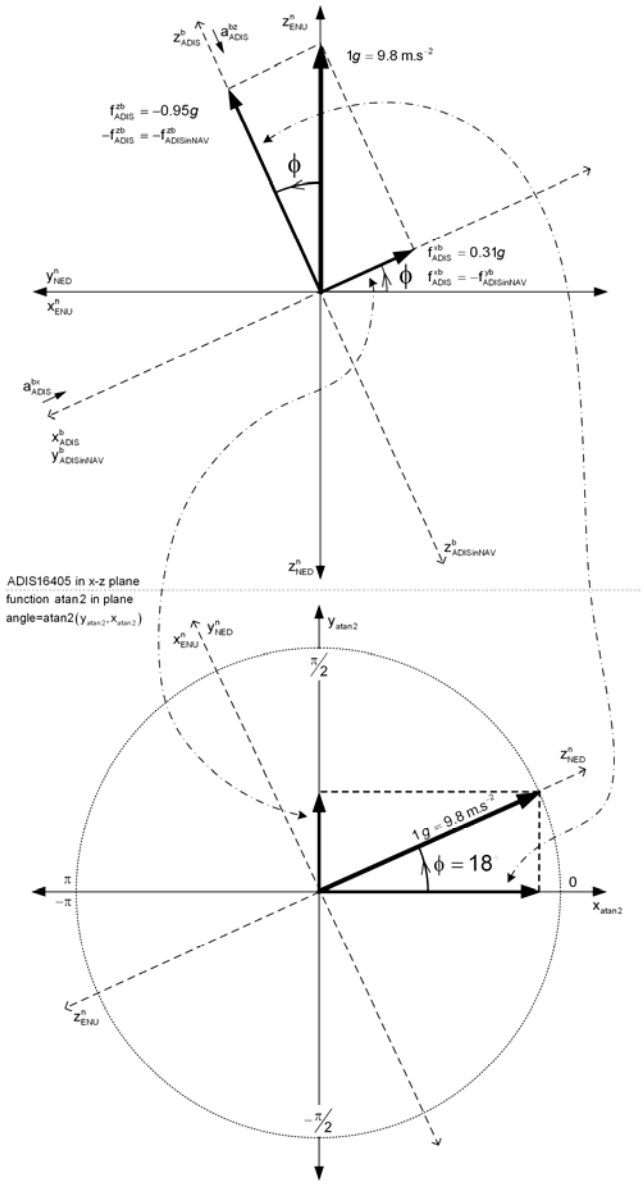

Figure 1
The determination of roll angle ϕ

Likewise, the pitch θ angle can be determined as

$$\theta = \operatorname{atan}2\left(f^{bx}_{ADISinNAV}, \sqrt{\left(f^{by}_{ADISinNAV}\right)^2 + \left(f^{bz}_{ADISinNAV}\right)^2} \right), \tag{20}$$

or, using of the accelerometers output measurements

$$\theta = \operatorname{atan2}\left(-f_{ADIS}^{by}, \sqrt{\left(f_{ADIS}^{bx}\right)^2 + \left(f_{ADIS}^{bz}\right)^2} \right). \tag{21}$$

The output of *y* accelerometer is $f_{ADIS}^{by} = 0.08g$ or applying the equation (7) it is $f_{ADISinNAV}^{bx} = -0.08g$, so the values of specific forces can be substituted to equation (20) as following

$$\theta = \operatorname{atan2}\left(\left(-0.08g\right), \sqrt{\left(-0.31g\right)^2 + \left(-0.95g\right)^2} \right) = -4.57^\circ . \tag{22}$$

When the measured values of specific forces are substituted to equation (21) we can get following

$$\theta = \operatorname{atan2}\left(-\left(0.08g\right), \sqrt{\left(0.31g\right)^2 + \left(-0.95g\right)^2} \right) = -4.57^\circ . \tag{23}$$

3.2 Course Alignment

The goal of the course alignment is to determine the yaw angle ψ between the navigation frame and the body frame. For the low-cost sensors, where low quality gyroscopes are used (it means the errors of the gyroscopes are greater than angular rate of Earth), the yaw can be determined by the magnetometers [6, 10].

Using the World Magnetic Model [2], the geomagnetic field vector, $\boldsymbol{b}_{Earth}$, can be described by 7 elements. These are the northerly intensity b_{Earth}^{nx} , the easterly intensity b_{Earth}^{ny} , the vertical intensity b_{Earth}^{nz} (positive downwards) and the following quantities derived from b_{Earth}^{nx} , b_{Earth}^{ny} , and b_{Earth}^{nz} - i.e. the total intensity $\left\|\boldsymbol{b}_{Earth}\right\|$, the horizontal intensity $b_{Earth}^{horizontal}$, the inclination angle $\gamma_{inclination}$, (also called the dip angle and measured from the horizontal plane to the field vector, positive downwards), and the declination angle $\alpha_{declination}$ (also called the magnetic variation and measured clockwise from true north to the horizontal component of the field vector). In the descriptions of b_{Earth}^{nx} , b_{Earth}^{ny} , b_{Earth}^{nz} , $\left\|\boldsymbol{b}_{Earth}\right\|$, $b_{Earth}^{horizontal}$, $\gamma_{inclination}$ and $\alpha_{declination}$ above, the vertical direction is perpendicular to the WGS-84 ellipsoid model of the Earth, the horizontal plane is perpendicular to the vertical direction, and the rotational directions clockwise and counter-clockwise are determined by a view from above (see Fig. 2). The Earth's geomagnetic field points from the magnetic north pole to the magnetic south pole through the Earth, taking the opposite path through the upper atmosphere. The field is thus vertical at the magnetic poles and horizontal near the equator.

The magnetic field is measured by the three magnetometers of ADIS16405 and the vector of magnetic field can be denoted as $\boldsymbol{m}^{\mathrm{b}}_{\mathrm{ADIS}} = \left[\mathrm{m}^{\mathrm{bx}}_{\mathrm{ADIS}}, \mathrm{m}^{\mathrm{by}}_{\mathrm{ADIS}}, \mathrm{m}^{\mathrm{bz}}_{\mathrm{ADIS}} \right]^{\mathrm{T}}$. Due to same reason as mentioned for the accelerometers, it should be transformed by the following

$$\boldsymbol{m}^{\mathrm{b}}_{\mathrm{ADISinNAV}} = \boldsymbol{C}^{\mathrm{ADISinNAV}}_{\mathrm{ADIS}} \cdot \boldsymbol{m}^{\mathrm{b}}_{\mathrm{ADIS}} . \tag{24}$$

The relationship between the magnetic vector in the body frame and the navigation frame can be expressed by

$$\boldsymbol{m}^{\mathrm{n}} = \boldsymbol{C}^{\mathrm{n}}_{\mathrm{b}} \cdot \boldsymbol{m}^{\mathrm{b}}_{\mathrm{ADISinNAV}} . \tag{25}$$

Using equation (4), equation (21) can be rewritten as

$$\boldsymbol{m}^{\mathrm{n}} = \left[\psi\right]^{\mathrm{T}}_{3} \cdot \left[\theta\right]^{\mathrm{T}}_{2} \cdot \left[\phi\right]^{\mathrm{T}}_{1} \cdot \boldsymbol{m}^{\mathrm{b}}_{\mathrm{ADISinNAV}} , \tag{26}$$

multiplying both sides by the rotation matrix $\left[\psi\right]_{3}$ we get

$$\left[\psi\right]_{3} \cdot \boldsymbol{m}^{\mathrm{n}} = \left[\theta\right]^{\mathrm{T}}_{2} \cdot \left[\phi\right]^{\mathrm{T}}_{1} \cdot \boldsymbol{m}^{\mathrm{b}}_{\mathrm{ADISinNAV}} , \tag{27}$$

and

$$\left[\theta\right]^{\mathrm{T}}_{2} \cdot \left[\phi\right]^{\mathrm{T}}_{1} \cdot \boldsymbol{m}^{\mathrm{b}}_{\mathrm{ADISinNAV}} = \left[\psi\right]_{3} \cdot \boldsymbol{m}^{\mathrm{n}} . \tag{28}$$

Expressing $\left[\theta\right]^{\mathrm{T}}_{2} \cdot \left[\phi\right]^{\mathrm{T}}_{1}$, equation (28) can be rewritten

$$\begin{bmatrix} \cos\theta & \sin\theta\sin\phi & \sin\theta\cos\phi \\ 0 & \cos\phi & -\sin\phi \\ -\sin\theta & \cos\theta\sin\phi & \cos\theta\cos\phi \end{bmatrix} \cdot \boldsymbol{m}^{\mathrm{b}}_{\mathrm{ADISinNAV}} = \left[\psi\right]_{3} \cdot \boldsymbol{m}^{\mathrm{n}} . \tag{29}$$

The roll and pitch angles are determined by equations (16), (20) and the vector $\boldsymbol{m}^{\mathrm{b}}_{\mathrm{ADISinNAV}}$ is known from equation (24) respective from the magnetometers measurements. Therefore, the left side can be substituted by the new vector $\boldsymbol{m}^{\theta\phi}_{\mathrm{ADISinNAV}}$,

where

$$\boldsymbol{m}^{\theta\phi}_{\mathrm{ADISinNAV}} = \begin{bmatrix} \cos\theta & \sin\theta\sin\phi & \sin\theta\cos\phi \\ 0 & \cos\phi & -\sin\phi \\ -\sin\theta & \cos\theta\sin\phi & \cos\theta\cos\phi \end{bmatrix} \cdot \boldsymbol{m}^{\mathrm{b}}_{\mathrm{ADISinNAV}} . \tag{30}$$

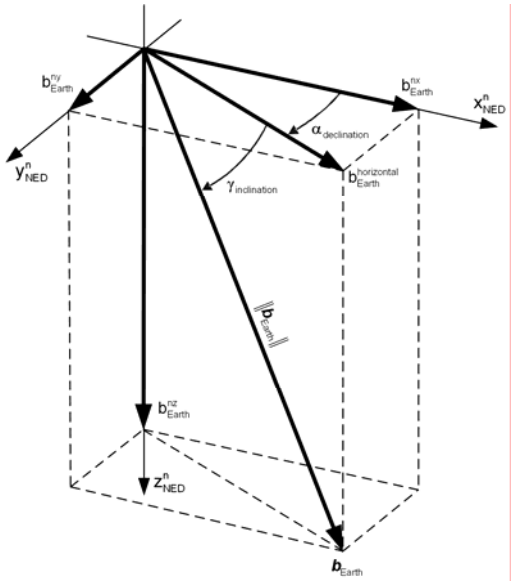

Figure 2
The geomagnetic field vector in the navigation frame

The right side of the equation (29) consists of the unknown variable yaw ψ and the magnetic field vector $\boldsymbol{m}^{\mathrm{n}}$ expressed in the navigation frame, which represents the geomagnetic field vector $\boldsymbol{b}_{\mathrm{Earth}}$. The geomagnetic field vector $\boldsymbol{b}^{\mathrm{n}}_{\mathrm{Earth}}$ in the navigation frame can be calculated as

$$\boldsymbol{m}^{\mathrm{n}} = \boldsymbol{b}^{\mathrm{n}}_{\mathrm{Earth}} = \boldsymbol{C}^{\mathrm{n}}_{\mathrm{GMF}} \cdot \begin{bmatrix} \|\boldsymbol{b}_{\mathrm{Earth}}\| \\ 0 \\ 0 \end{bmatrix}, \tag{31}$$

where $\boldsymbol{C}^{\mathrm{n}}_{\mathrm{GMF}}$ is the transformation matrix from the geomagnetic frame to the navigation frame, and is determined according to equation (6) with the declination and the inclination angles

$$\boldsymbol{C}^{\mathrm{n}}_{\mathrm{GMF}} = \left[\alpha_{\mathrm{declination}}\right]^{\mathrm{T}}_{3} \cdot \left[-\gamma_{\mathrm{inclination}}\right]^{\mathrm{T}}_{2} \cdot \left[0\right]^{\mathrm{T}}_{1}, \tag{32}$$

where

$$\left[-\gamma_{\mathrm{inclination}}\right]_2 = \begin{bmatrix} \cos(-\gamma_{\mathrm{inclination}}) & 0 & \sin(-\gamma_{\mathrm{inclination}}) \\ 0 & 1 & 0 \\ -\sin(-\gamma_{\mathrm{inclination}}) & 0 & \cos(-\gamma_{\mathrm{inclination}}) \end{bmatrix}, \tag{33}$$

$$\left[\alpha_{\text{declination}}\right]_3 = \begin{bmatrix} \cos\alpha_{\text{declination}} & \sin\alpha_{\text{declination}} & 0 \\ -\sin\alpha_{\text{declination}} & \cos\alpha_{\text{declination}} & 0 \\ 0 & 0 & 1 \end{bmatrix}. \tag{34}$$

Applying equations (30) and (31), equation (29) can be rewritten as

$$\boldsymbol{m}_{\text{ADISinNAV}}^{\theta\phi} = \left[\psi\right]_3 \cdot \boldsymbol{C}_{\text{GMF}}^{\text{n}} \cdot \begin{bmatrix} \left\|\boldsymbol{b}_{\text{Earth}}\right\| \\ 0 \\ 0 \end{bmatrix}, \tag{35}$$

or

$$\boldsymbol{m}_{\text{ADISinNAV}}^{\theta\phi} = \left[\psi\right]_3 \cdot \left[\alpha_{\text{declination}}\right]_3^{\text{T}} \cdot \left[-\gamma_{\text{inclination}}\right]_2^{\text{T}} \cdot \begin{bmatrix} \left\|\boldsymbol{b}_{\text{Earth}}\right\| \\ 0 \\ 0 \end{bmatrix}, \tag{36}$$

and after multiplying the right side

$$\boldsymbol{m}_{\text{ADISinNAV}}^{\theta\phi} = \left[\psi\right]_3 \cdot \begin{bmatrix} \cos\alpha_{\text{declination}} \cdot \cos\gamma_{\text{inclination}} \\ \sin\alpha_{\text{declination}} \cdot \cos\gamma_{\text{inclination}} \\ \sin\gamma_{\text{inclination}} \end{bmatrix} \cdot \left\|\boldsymbol{b}_{\text{Earth}}\right\|, \tag{37}$$

where $\alpha_{\text{declination}}$, $\gamma_{\text{inclination}}$ and $\left\|\boldsymbol{b}_{\text{Earth}}\right\|$ can be determined by the World Magnetic Model [2]. The angle between the magnetic north pole and the *x* axis of the body frame can determine the magnetic heading

$$\psi_{\text{m}} = \psi - \alpha_{\text{declination}}\,. \tag{38}$$

The low-cost systems assume the magnetometers measurements are either isolated or compensated from the vehicle magnetic field [6]. Also, there are the assumptions that the local magnetic field deviation and inclination are compensated. Taking these assumptions into consideration, equation (31) and equation (35) can be rewritten

$$\boldsymbol{m}^{\text{n}} = \begin{bmatrix} \left\|\boldsymbol{b}_{\text{Earth}}\right\| & 0 & 0 \end{bmatrix}^{\text{T}}, \tag{39}$$

$$\boldsymbol{m}_{\text{ADISinNAV}}^{\theta\phi} = \left[\psi\right]_3 \cdot \begin{bmatrix} \left\|\boldsymbol{b}_{\text{Earth}}\right\| \\ 0 \\ 0 \end{bmatrix}, \tag{40}$$

or

$$\boldsymbol{m}_{\mathrm{ADISinNAV}}^{\theta\phi} = \begin{bmatrix} \cos\psi \\ -\sin\psi \\ 0 \end{bmatrix} \cdot \left\| \boldsymbol{b}_{\mathrm{Earth}} \right\|. \tag{41}$$

From equation (41), the yaw can be computed as

$$\psi = \operatorname{atan2}\left(-\mathrm{m}_{\mathrm{ADISinNAV}}^{\theta\phi\,\mathrm{y}}, \mathrm{m}_{\mathrm{ADISinNAV}}^{\theta\phi\,\mathrm{x}}\right), \tag{42}$$

where $\mathrm{m}_{\mathrm{ADISinNAV}}^{\theta\phi\,\mathrm{x}}, \mathrm{m}_{\mathrm{ADISinNAV}}^{\theta\phi\,\mathrm{y}}$ are transformed measured values from magnetometers.

The magnetometers are measuring the following values $\boldsymbol{m}_{\mathrm{ADIS}}^{\mathrm{b}} = \left[86.0, 233.5, -361.0\right]^{\mathrm{T}}$ mG and therefore the values of roll and pitch from equations (17) and (22) can be substituted to equation (30) as following

$$\boldsymbol{m}_{\mathrm{ADISinNAV}}^{\theta\phi} = \begin{bmatrix} 0.99 & -0,02 & -0,07 \\ 0 & 0,95 & -0,30 \\ 0,07 & 0,30 & 0,94 \end{bmatrix} \cdot \underbrace{\boldsymbol{C}_{\mathrm{ADIS}}^{\mathrm{ADISinNAV}} \cdot \begin{bmatrix} 86.0 \\ 233.5 \\ -361.0 \end{bmatrix}}_{\boldsymbol{m}_{\mathrm{ADISinNAV}}^{\mathrm{b}}} = \begin{bmatrix} 203.2 \\ -29.7 \\ 387.3 \end{bmatrix} \mathrm{mG}. \tag{43}$$

Substituting $\mathrm{m}_{\mathrm{ADISinNAV}}^{\theta\phi\,\mathrm{x}}, \mathrm{m}_{\mathrm{ADISinNAV}}^{\theta\phi\,\mathrm{y}}$ from equation (43) into equation (42) the value of yaw angle is the following

$$\psi = \operatorname{atan2}\left(-\left(-29.7\right), 203.2\right) = 8.3^{\circ}. \tag{44}$$

4 The Sensor ADIS16405

The ADIS16405 iSensor is a complete inertial system that consists of triaxal gyroscope, triaxial accelerometer, and triaxial magnetometer sensors [1]. Each sensor in the ADIS16405 combines industry-leading iMEMS technology with signal conditioning optimizing dynamic performances. The factory calibration characterizes each sensor for sensitivity, bias, alignment, and linear acceleration (gyro bias). As a result, each sensor has its own dynamic compensation formulas that provide accurate sensor measurements over a temperature range of −40°C to +85°C. The magnetometers employ a self-correction function to provide accurate bias performance over temperature as well. The ADIS16405 provides a simple, cost-effective method for integrating accurate, multi-axis, inertial sensing into industrial systems, especially when compared with the complexity and investment associated with discrete designs. All necessary motion testing and calibration are part of the production process at the factory, greatly reducing system integration

time. Tight orthogonal alignment simplifies inertial frame alignment in navigation systems. An improved SPI interface and register structure provide faster data collection and configuration control. This compact module is approximately 23 mm × 23 mm × 23 mm and provides a flexible connector interface, which enables multiple mounting orientation options, see Fig. 3. The functional block diagram of ADIS16405 is illustrated in Fig. 4.

BASIC SPECIFICATIONS OF ADIS16405

GYROSCOPES	
Dynamic Range	**±300°/sec**
or	**±150°/sec**
or	**±75°/sec**
Initial Sensitivity	
for range ±300°/sec	**0.05 °/sec/LSB**
for range ±150°/sec	**0.025 °/sec/LSB**
for range ±75°/sec	**0.0125 °/sec/LSB**
Initial Bias Error (±1σ)	**±3 °/sec**
In-Run Bias Stability (1 σ)	**0.007 °/sec**
Angular Random Walk (1 σ)	**2.0 °/√hr**
Output Noise ±300°/sec range, no filtering, rms	**0.9 °/sec**
Rate Noise Density (±300°/sec, no filtering, rms)	**0.05 °/sec/√Hz**
ACCELEROMETERS	
Dynamic Range	**±18g**
Initial Sensitivity	**3.33 m*g*/LSB**
Initial Bias Error (±1 σ)	**±50 m*g***
In-Run Bias Stability (1 σ)	**0.2 m*g***
Velocity Random Walk (1 σ)	**0.2 m/sec/√hr**
Output Noise (no filtering, rms)	**9 m*g***
Noise Density (no filtering,rms)	**0.5 m*g*/√Hz**
MAGNETOMETERS	
Dynamic Range	**±3.5gauss**
Initial Sensitivity	**0.5 mgauss/LSB**
Initial Bias Error (±1 σ)	**±4 mgauss**
Output Noise (no filtering, rms)	**1.25 mgauss**
Noise Density (no filtering, rms)	**0.066 mgauss/√Hz**
POWER SUPPLY	
Operating voltage range, VCC	**5.0 V**
Power Supply Current (max)	**70 mA**

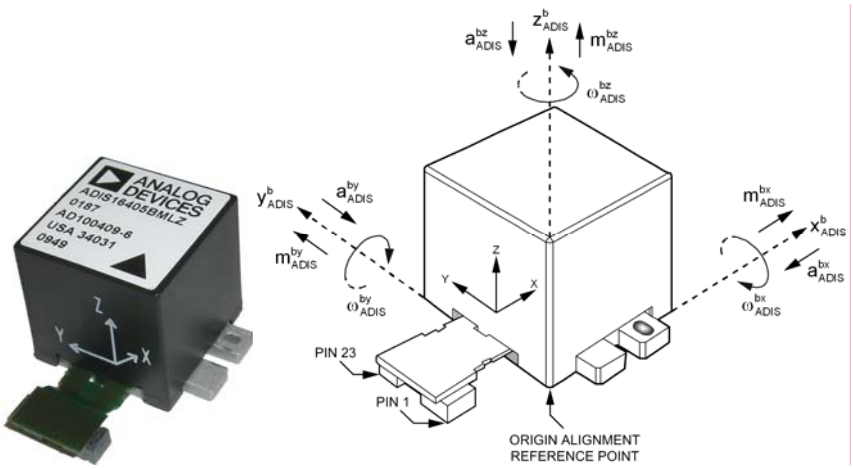

Figure 3
The sensor ADIS16405BMLZ

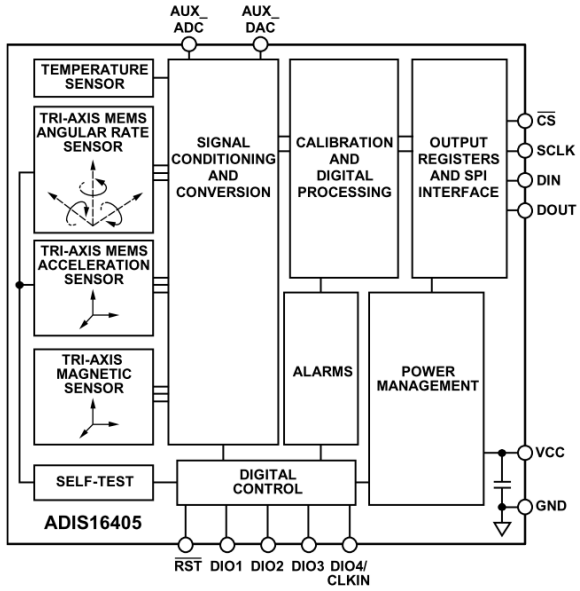

Figure 4
Functional Block Diagram of ADIS16405 [1]

5 Tests & Results

All tests were conducted using the INS/GNSS development kit. The INS/GNSS development kit is shown in Fig. 5 and consists of the inertial measurement unit ADIS16405, the GNSS receiver LEA-5T, pressure sensors and a WIFI module. All sensors and systems are controlled by the processor. These tests have been conducted using the ADIS16405 and the WIFI module only. The data from ADIS16405 were processed and then transferred by WIFI module to a personal computer for further processing.

Figure 5
The rotation platform with INS/GNSS development kit placed on it

The IMU was externally synchronized by the processor and the data sampling rate was 100 Hz. For testing, the INS/GNSS development kit was mounted on the rotation platform. The varied attitudes of ADIS16405 within the known quadrants were set and the data from sensors were collected and processed. For every adjusted attitude, an average of 100 measured samples was computed. In other words, according to the equations (45) and (46), the mean for each sensor was calculated.

$$\boldsymbol{f}^{\mathrm{b}}_{\mathrm{ADIS}} = \frac{\sum_{\mathrm{k=1}}^{100} \boldsymbol{f}^{\mathrm{b}}_{\mathrm{ADIS}}(\mathrm{k})}{100} \tag{45}$$

$$\boldsymbol{m}^{\mathrm{b}}_{\mathrm{ADIS}} = \frac{\sum_{\mathrm{k=1}}^{100} \boldsymbol{m}^{\mathrm{b}}_{\mathrm{ADIS}}(\mathrm{k})}{100} \tag{46}$$

The roll, pitch and yaw angles were calculated from average values.

Three tests were conducted. During the first test the roll angle was changed within an interval $\pm 30^{\circ}$. The results for this test are depicted in Fig. 9. The large crosses represent the manually set roll angles of the platform. The small crosses represent the values of the roll angles calculated from the measured data. During the second test, the pitch angle varied within an interval $\pm 60^{\circ}$. The test results are illustrated in Fig. 10. During the last test, the yaw angle varied from 0° to 360° and the results are shown in Fig. 11. The raw measured data from sensors, for all three tests, are depicted in Fig. 6, Fig. 7 and Fig. 8. The equations (16), (20) and (42) were used to calculate the values of the Euler angles.

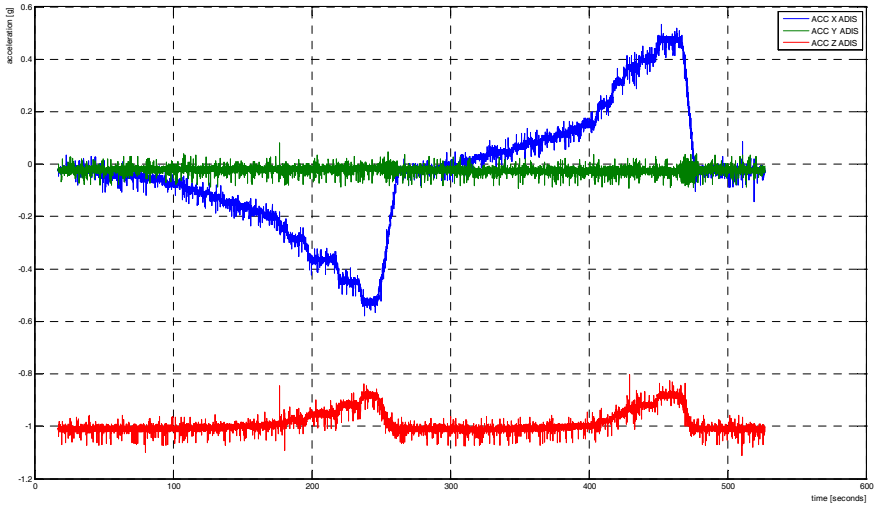

Figure 6
Test 1 - measured data for the roll angle

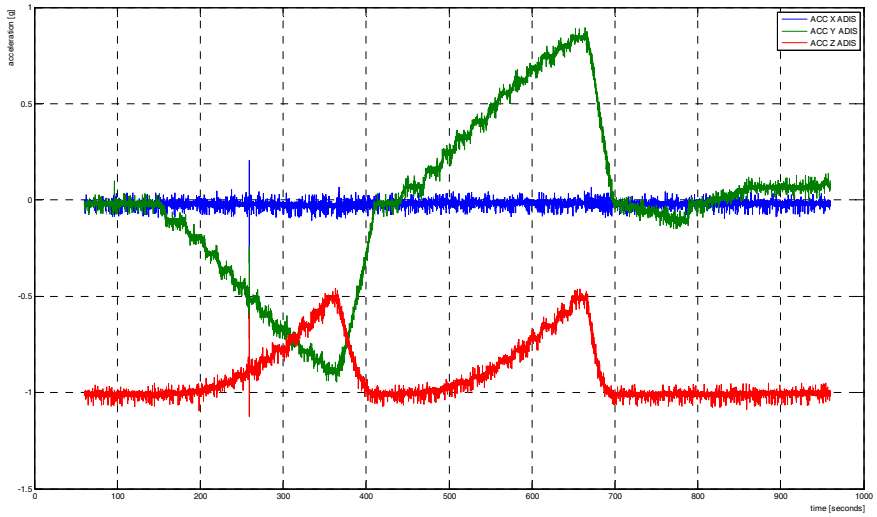

Figure 7
Test 2 - measured data for the pitch angle

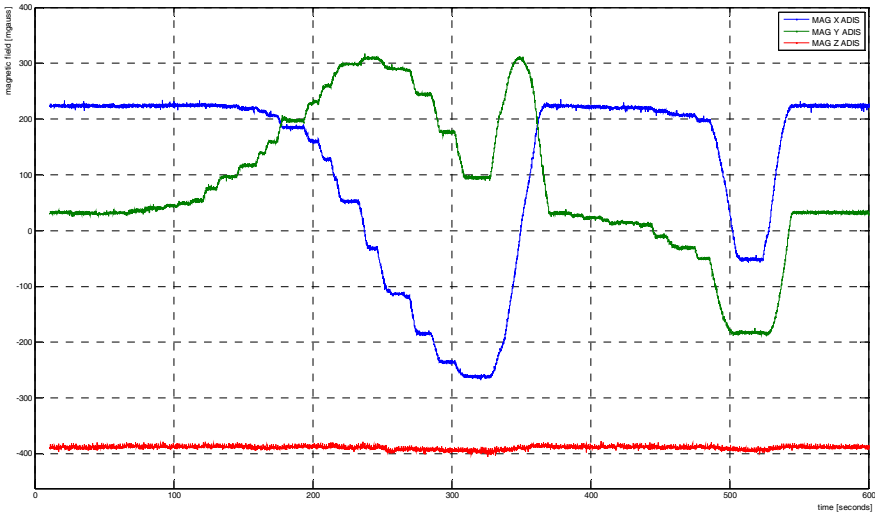

Figure 8
Test 3 - measured data for the yaw angle

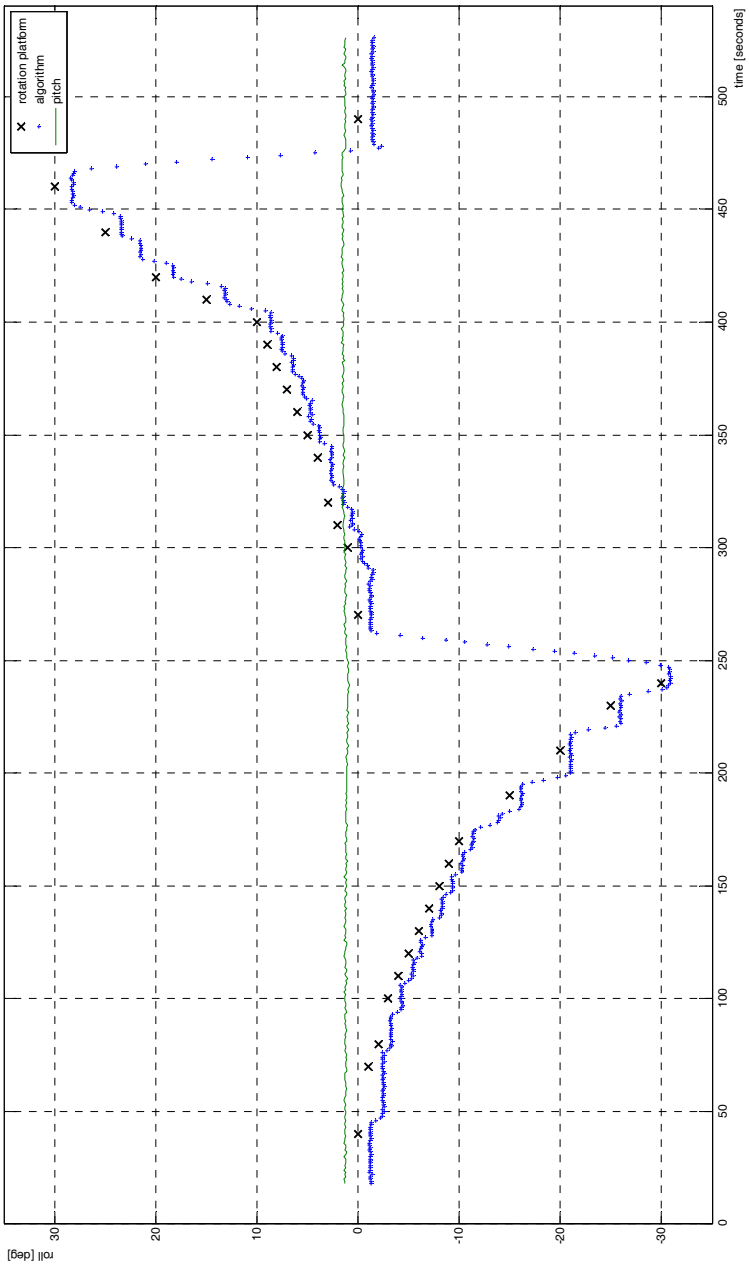

Figure 9
Test 1 - the roll angle measurement

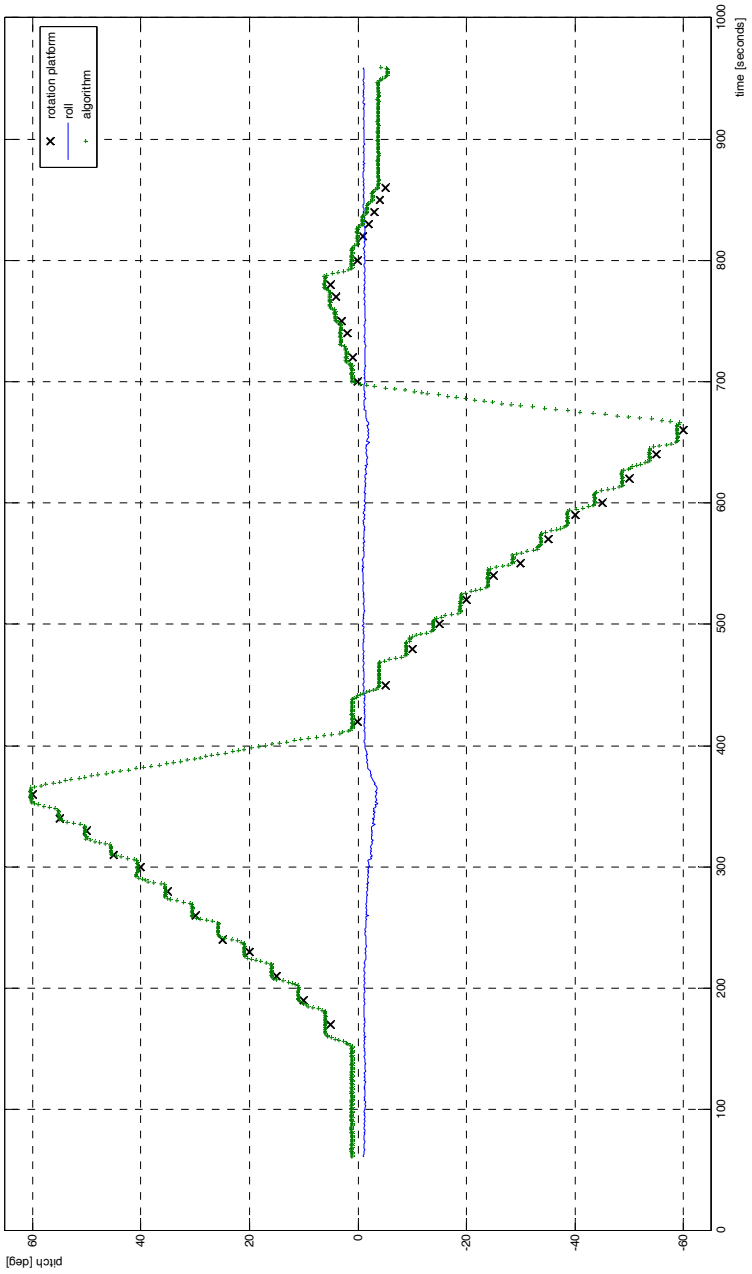

Figure 10
Test 2 - the pitch angle measurement

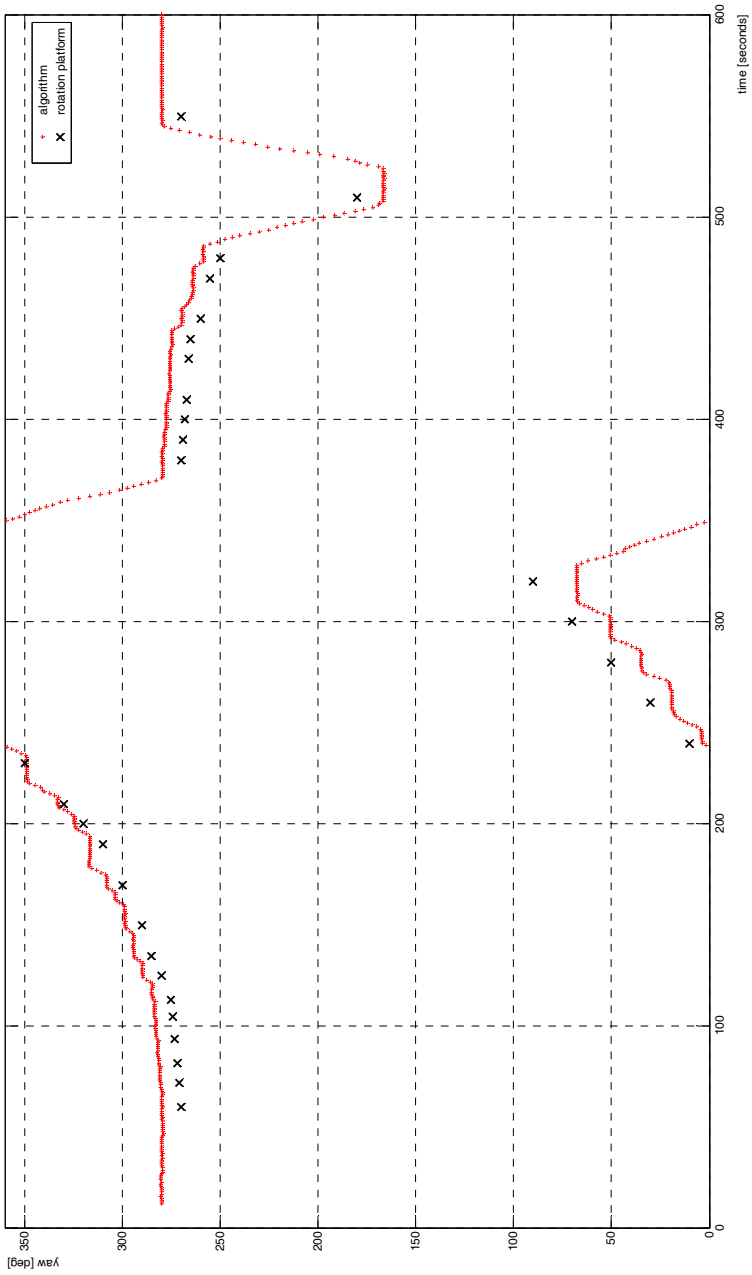

Figure 11
Test 3 - the yaw angle measurement

Conclusion

The paper describes the testing of the coarse alignment algorithm for the inertial measurement unit ADIS16405 using a rotation platform. The main part of the paper deals with the coarse alignment algorithm for the inertial measurement unit. The attitudes (the roll, pitch and yaw angles) are defined by equations (16), (20) and (42). The results of the tests are depicted. It is clear that the calculated values of the roll and pitch angles are not identical to values set by the rotation platform. The reason for the difference is a bias of accelerometers. Each milli-*g* of sensor bias contributes to the attitude estimate by 1 mrad of the error. The error in yaw angle determination is caused by magnetometer and accelerometer bias as well as by rough determination of the initial direction of rotation platform with respect to the north magnetic pole. The tests were conducted using the INS/GNSS development kit which was mounted on the rotation platform. The results confirm the validity of the coarse alignment algorithm for ADIS16405. The main contribution of this research is the coarse alignment algorithm for the ADIS16405 which was evaluated and applied for real sensor data. This coarse alignment algorithm is implemented in the real-time integrated navigation systems developed nowadays.

Acknowledgment

This research was supported by the project “Integrated navigation systems” No.: SPP–852_08-RO02_RU21-240, Sponsored by the Ministry of Defense of the Slovakia.

References

[1] Datasheet of ADIS16405: High Precision Tri-Axis Gyroscope, Accelerometer, Magnetometer http://www.analog.com/static/imported-files/data_sheets/ADIS16400_16405.pdf

[2] Maus, S., Macmillan S., McLean S., Hamilton B., Thomson A., Nair M., and Rollins C.: The US/UK World Magnetic Model for 2010-2015, NOAA Technical Report NESDIS/NGDC

[3] Sotak, M., Sopata, M., Breda, R., Rohac, J., Vaci, L.: Navigation System Integration. Monograph: 1. ed., printed by Robert Breda, Kosice, the Slovak Republic, 2006, ISBN 80-969619-9-3 (in Slovak)

[4] Reinstein, M., Sipos, M., Rohac, J. Error Analyses of Attitude and Heading Reference Systems. In Przegląd Elektrotechniczny, ISSN 0033-2097, Vol. 85, No. 8, pp. 114-118, 2009

[5] Farrell, J. A, M. Barth.: The Global Positioning System and Inertial Navigation: Theory and Practice. McGraw-Hill 1999. ISBN-0-07-022045-X

[6] Farrell, J. A.: Aided Navigation: GPS with High Rate Sensors. McGraw-Hill 2008, ISBN: 978-0-07-149329-8

[7] Berezny, S. [et al.]: Another Mathematical Optimization Models Based on Assignment Problem. In: Acta Montanistica Slovaca, ISSN 1335-1788, Vol. 12, No. 4, pp. 356-360, 2007

[8] Orejas, M. E., Vaci, L., Sopata M.: Multiple Sensor Integration for Autonomous Vehicle Navigation. In: MOSATT 2009: proceedings of the International scientific Conference: Zlata Idka, September 22-24, 2009, Košice: printed by Robert Breda, pp. 272-277, ISBN 978-80-970202-1-7, 2009

[9] Groves, Paul D.: Principles of GNSS, Inertial, and Multi-Sensor Integrated Navigation Systems. Artech House Publishers, 2007, ISBN: 978-1580532556

[10] Kuffova, M., Kralik, V.: Indoor Navigation and Mapping Robot System. In: ICMT ´09: International Conference on Military Technologies 2009, May 5-6, 2009, Brno: University of Defence, ISBN 978-80-7231-648-9, pp. 499-502, 2009

[11] Breda, R.: Computation of Navigational Equation in the Inertial Coordinate System. In: Acta Avionica, ISSN 1335-9479, Vol. 11, No. 17, pp. 71-73, 2009

[12] Necas, P.: Simulation Systems and the Slovak Digitalized Terrain Environment. In: ITEC 2001, 12th International Conference and Exhibition for Training, Education and Simulation, April 24-26, 2001, Lille, France, Warminster, 2001, ISBN 0953-4215-4-4

[13] Labun J., Adamcik F., Pila J., et al.: Effect of the Measured Pulses Count on the Methodical Error of the Air Radio Altimeter, In: Acta Polytechnica Hungarica, Vol. 7, Issue: 1, pp. 41-49, 2010, ISSN 1785-8860

[14] Kelemen, M.: Progressive Technologies in Military Aviation Education and Training: The Part of Navigation in Support of Human Activity on the SEA, 14th International Scientific and Technical Conference Proceedings, Naval University of Gdynia Gdynia, November 18-19, 2004

[15] Kurnaz S., Cetin O.: Autonomous Navigation and Landing Tasks for Fixed Wing Small Unmanned Aerial Vehicles, In: Acta Polytechnica Hungarica, Vol. 7, Issue 1, pp. 87-102, 2010, ISSN 1785-8860

[16] Ochodnicky, J.: Multisensor Networks. Data Association and Target Tracking Principles. Military Academy, Liptovsky Mikulas, ISBN 80-8040-157-8, 2001 (in Slovak)

[17] Cizmar, J., Skvarek, J., Jalovecky, R.: An Inertial Reference Unit - Development and Testing, 2nd International Scientific Conference, Bratislava, April 29, 2008, ISBN: 978-80-8075-324-5

Investigation of the Hysteretic Phenomena in RHEED Intensity Change in the Study of Surface Reconstruction

Ákos Nemcsics[1], Jenő Takács[2]

[1] Institute for Microelectronics and Technology, Óbuda University
Tavaszmező u. 17, H-1084 Budapest, Hungary;
Research Institute for Technical Physics and Materials Science
P.O.Box 49, H-1525 Budapest, Hungary
E-mail: nemcsics.akos@kvk.uni-obuda.hu

[2] Department of Engineering Science, University of Oxford
Parks Rd., Oxford OX1 3PJ, UK

Abstract: This paper describes a study of the RHEED intensity change against temperature in case of GaAs and InAs surfaces. RHEED as a technique is a widely used monitoring method for observing molecular-beam-epitaxial (MBE) growth. The reconstruction and other changes of the surface can be investigated by observing the RHEED pattern. Both the static and the dynamic RHEED-s are very complex phenomena, but these effects can be used as versatile tools for in-situ monitoring of the growth of the epitaxial layer, in spite of the fact that we do not know much about the details of its nature. Our observations showed that the specular beam intensity of RHEED had changed with the change of the surface temperature. We investigated the changes of the GaAs and InAs (001) surfaces by using this effect. The change in intensity follows the observed surface reconstruction. This change in the RHEED intensity against temperature shows hysteretic properties, with a different character for each material. So far, the explanations for these phenomena were different in both cases. Here, we explain these hysteretic phenomena in general terms with the T(x) hyperbolic model for coupled hysteretic systems, which is applicable to both materials. Experimental results presented in the paper are in good agreement with the model predictions.

Keywords: RHEED; GaAs; InAs; hysteresis; surface reconstruction

1 Introduction and Experimental Preliminaries

The compound semiconductor structures grown by Molecular Beam Epitaxial (MBE) technology play an important role in the construction of semiconductor devices. Out of the compound semiconductors the most important group is the one III-V based. In this technology, the polar surfaces with (001) orientation are

fundamentally important. For the growth of low-dimensional nano structures it is vital to know the growth kinetics of the process. The MBE growth can be observed in-situ by monitoring the surface condition of the crystal (i.e. the surface reconstruction) by Reflection High-Energy Electron Diffraction (RHEED), which helps to understand the growth kinetics. In the case of exact and near layer-by-layer growth, the mostly observed surface reconstruction is (2x4), although other surface reconstructions are also present. Earlier investigations have been done at constant temperature [1]. At a given temperature the ratio between As and the metallic component was changed and the surface construction was monitored [2]. The results of these experiments were presented in temperature versus reconstruction phase diagrams. We found that the phase limits are often ambiguous. We can extract further information by changing not only the ratio between As and the metallic component but also the temperature. By changing the temperature we observed a change in reconstruction and specular spot intensity variation. We also observed hysteresis in the intensity change of the specular spot against the changing temperature [3].

In the following we are going to investigate the changes in the behaviour of GaAs and InAs (001) surfaces against temperature variation, based on the experiments of Yamaguhi and Horikoshi [3]. This intensity variation against temperature shows hysteretic properties. During the experiment, the change in temperature was slow, so every point could be regarded as being in the state of thermal equilibrium. During the experiments, As4 were used for the source of As. Shown by experimental results, the temperature dependence of the intensity of the specular spot depends neither on the incident azimuth angles nor on the energy of the electron beam [3]. We can say, therefore, that the intensity change of the specular spot is basically not the result of diffraction.

The RHEED specular spot intensity versus temperature diagrams are depicted in Fig. 1 and Fig. 2 for InAs and GaAs respectively. The results show that at lower temperature the specular spot intensity is high. With a raise in temperature the intensity gradually diminishes. Both in the case of GaAs and InAs, the surface at lower temperature shows arsenic-terminated (2×4) surface reconstruction. At higher temperature, however, In/Ga-terminated (4×2) surface reconstruction can be observed. The directional change of the temperature shows that the process is subject to hysteresis. In the case of both semiconductors tested, the observed hysteresis loops fall within approximately a 50 $^{\circ}$C temperature range. In the case of InAs, we had two distinct hysteresis loops. At a lower temperature the observed wide loop is the indication of smaller intensity variation. At a higher temperature however we see a narrower loop with large and rapid intensity change. In the case of GaAs there is only one real loop at the lower temperature and a assumed degenerate pseudo loop at the higher temperature. In the second loop the ascending and the descending branches seemingly overlap. We will apply the general description of the phenomenon to both materials. In our present work we will consider two loops in both cases, giving a qualitative explanation for this

inverse spin-valve like, coupled loop structure. For the quantitative investigation we applied the *T(x)* hyperbolic hysteresis model, developed for general description of hysteretic phenomena and which can be used to model other natural phenomena with hysteretic character, e.g. in biology, chemistry etc. [4]. It must be emphasized that although the RHEED intensity changes, due to MBE crystal growth, analyzed here, it is a non-magnetic process, and its character is analogous to and carries all the characteristic hallmarks of an inverse spin valve.

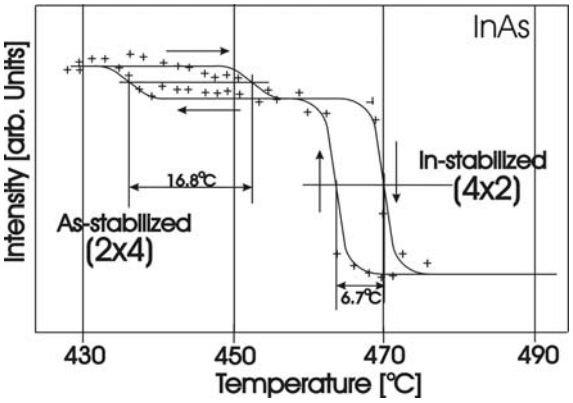

Figure 1
Temperature dependence of the specular beam intensity in the case of InAs (001) surface

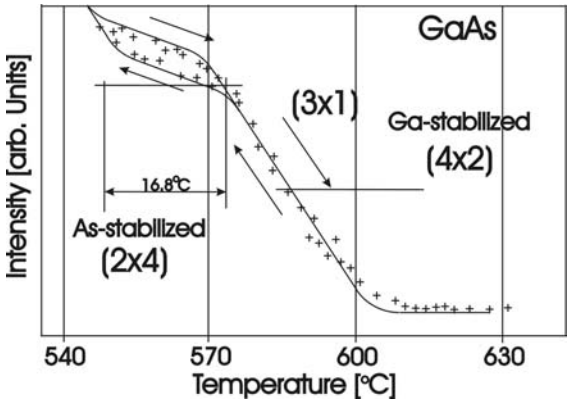

Figure 2
Temperature dependence of the specular beam intensity in the case of GaAs (001) surface

2 Discussion

2.1 Factors the Specular Spot Intensity of RHEED Depends on

As we know from the experimental results, the temperature dependence of the specular spot intensity is independent from the incidental and azimuth angles, as well as from the energy of the electron beam. This shows that it is not caused by diffraction but rather caused by a more complex phenomenon. The intensity of the specular spot also depends on the morphology of the surface. A surface with a perfect monolayer on top has high reflectivity, and therefore has a high specular spot intensity. The imperfect surface disperses the electrons, which results in a lower specular spot intensity. Changing temperatures cause the As components to leave the surface. This, by causing surface roughening, contributes to the lowering of the specular spot intensity, in addition to other causes nearly independent of diffraction. (The interaction between the electron beam and the surface, observed at a constant temperature, shows that the specular spot intensity is dependent on the incident and azimuth angle of the beam [1]. This is an indication that the diffraction also plays an important role in the process. When we observed the temperature dependence at fixed incident and azimuth angles, then we found the same relations [3]. The change in the angles was followed by the same pattern in the intensity change. From this we have concluded that specular intensity change versus temperature in not a diffraction phenomenon. The dispersion from the roughened surface is high and therefore the specular spot intensity will be low. With increasing temperature the crystal components begin to leave the surface, leaving a rougher surface behind.

The upper part of Fig. 3 depicts a simplified model of a semiconductor. Since the metallic component has a sticking coefficient near to unity (S_{III}~1) it is expected that with higher temperature As will leave the surface. The incorporation of As takes place in three steps. The first step is the physisorption of the arsenic species, followed by the second, the dimeralization of the arsenic to be finally chemisorbed in this form to the surface. The dimers will split at this third stage and the arsenic atom will finally be incorporated in the lattice. These processes represent three different energy levels. In our experimental temperature range, however, we only need to deal with the last two processes [5-12].

B. A. Joyce provided a graphic description of the RHEED specular spot intensity variation, resulting from the growth of layers, which leads to intensity oscillations following the growth layer by layer [13]. The starting point of this description is that the surface is perfect to begin with; therefore the reflection of the electron beam is high from the surface, resulting in high specular spot intensity. During the process of growth, crystalline seeds form, which in time grow into islands. When these islands coalesce, they then form a complete new surface. During growth, the initial surface loses its smoothness and becomes rougher. This results in larger electron dispersion and reduced specular spot intensity.

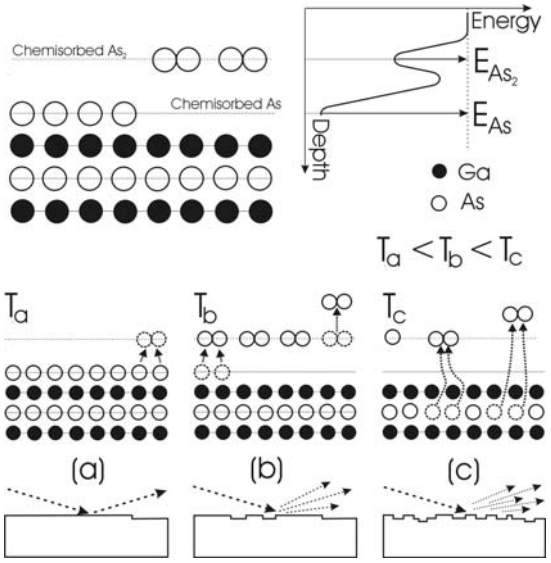

Figure 3

The chemisorbed As is incorporated in the surface in two stages. It is bound to the surface in the first stage in dimer and then in the second stage in atomic form.

The smooth surface gradually becomes rougher until it reaches maximum roughness, at which point it starts becoming smoother again. This change in surface morphology leads to specular spot intensity variation and eventually intensity oscillation. In spite of the simplicity of this model, it explains the decay of the RHEED intensity oscillation and confirms its quantitative description [14, 15]. The model of course is a gross simplification of the complex interaction between the electron beam and the surface. The specular spot intensity depends on the incidental angle and the electron beam direction, which is the cause of the phase shift of the intensity oscillation [16]. A number of researchers have already investigated and tried to explain this phenomenon [17-23]. The surface is always different from the bulk material because it tries to relax by getting to an energy minimum state and involving various surface reconstructions [24-31]. These reconstructions are dependent on the substrate temperature and the flux of the components. The reconstructions have very complicated phase diagrams. In first approximation there are two reconstruction phases to be considered. The first phase is when an As rich surface forms at a lower temperature and the second is when a surface, rich in Ga/In, forms at a higher temperature. In case of GaAs, the As rich formations are (2x4), c(2x8), C(4x4) or Ga-rich are (4x2), c(8x2), (6x6), (4x6). Between them there are transitory reconstructions such as (3x1), (1x6). Due to symmetry, one particular reconstruction may represent different atomic arrangements. For growing GaAs, the most widely used reconstruction is the β2(2x4), which in the direction of [-110] forms lines, made of As dimer pairs with trenches between them of depleted Ga. This surface is called As terminated after

this particular structure. During growth, this represents the perfect surface with maximum reflectivity, although the surface is obviously not flat. For the Ga induced growth the starting surface is (2x4), formed in an As atmosphere [14, 16] (see Fig. 4). As layers are grown one after the other, the surfaces of the successive layers become rougher, the oscillation decays and the secular spot intensity drops to minimum. In that case, the Ga rich surface shows (4x2) reconstruction [16]. Tempering of the surface, for maximizing intensity, is carried out by heat treatment in As atmosphere. With the increase of the secular spot intensity the (2x4) reconstruction reappears again [16]. The various surface reconstructions are associated with different surface stoichiometry, which is closely linked to the RHEED intensity. [32]. Although a large amount of information has already been compiled on the subject of surface reconstruction and its effect on the intensity and growth, there are still no acceptable comprehensive explanations of the phenomenon.

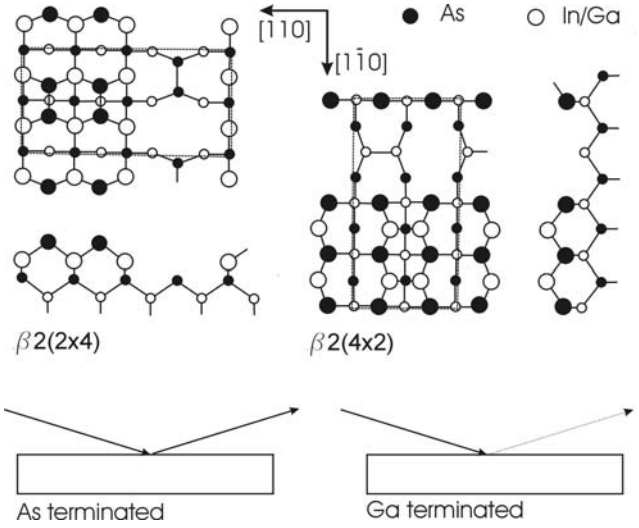

Figure 4

The surface reconstructions in As rich and in Ga rich cases. The relation between secular spot intensity and reconstruction. The reconstructed surface shows domain structure.

It is obvious that the explanation for the link between the roughened surface and the RHEED specular spot intensity covers only part of the truth. The surface, producing the maximum intensity, is not without imperfections, due to relaxation. At the same time the surface stoichiometry is changing all the time. A crystal surface with high content of As is associated with higher RHEED specular spot intensity, while a surface with high Ga/In content produces lower intensity. This is supported by observations of the phenomena at droplet-epitaxy, which shows that an As rich stripy RHEED picture becomes diffused, when the atoms of the Ga beam combine with the As atoms on the surface, they bind the Ga down and Ga settles on the surface [33].

As shown before, the specular spot intensity depend on the surface morphology and the surface construction. The increase in temperature causes primarily arsenic to leave the surface; therefore a perfect surface with high reflectivity is rich in arsenic. Any surface rich in metallic components has low reflectivity, disperses electrons and is the subject of droplet formation. Both the InAs and the GaAs crystallize in face-centered-cubic structure, with covalent binding, where four identical bindings can form due to sp^3-hybridisation. The four equivalent bindings represent identical electron distribution in different directions. At the surface this symmetry breaks up and the surface relaxes. In the case of the arsenic terminated surface, the probability of the presence of the electrons is higher, due to the distorted electron distribution caused by the missing binding, perpendicular to the surface. When the surface is Ge terminated, then the effect is the opposite. The arsenic terminated surface becomes marginally negative, repelling the electrons, making the specular spot intensity higher. When, however, the surface is In/Ga terminated, then the electrons of the incident beam are neutralized and the specular spot intensity is reduced. The composition and also the morphology of the surface is linked to the surface reconstruction, and this reconstruction is the function of the temperature as well as of the arsenic pressure. The various reconstructions are periodically roughing up the surface.

2.2 Qualitative Description of the Chemisorbtion Induced Hysteresis in RHEED Intensity

As we said before, the secular spot intensity depends strongly on the surface stoichiometry. The high As coverage (less metallic components on the surface) represents higher intensity, whilst the low coverage of As represents lower intensity. In the intensity description we cannot disregard the effect of the surface morphology (see Section 2.3). The absorption-desorbtion phenomena in general always show hysteresis. The absorption-desorbtion depends on the state of the surface. Due to this dependence, the species bound at the surface, facing different conditions at the beginning, than later on when they leaving the surface towards the end of the process. This is of course true when the process is reversed. The absorption-desorbtion process of the materials falling into the III-V group is very complex.

The peculiar residing properties of the As, described in Section 2.1, has been the subject of investigation by a number of researchers using different methods [34-39]. In our case the As turned out to be in tetramer form (As_4). The As tetramer splits up on the arrival to the surface and settles in as one or two As dimmers, depending on the availability of free locations. Following that, it resides into its final location in the atomic state. The process is depicted in Fig. 5 where activation energy of the dimmer is marked with E_{AS2}, while the residing energy of As is represented by E_{As}. When the As is leaving the surface then the process is reversed. The As can leave the surface directly without going through the dimmer state; therefore the two processes do not mirror each other.

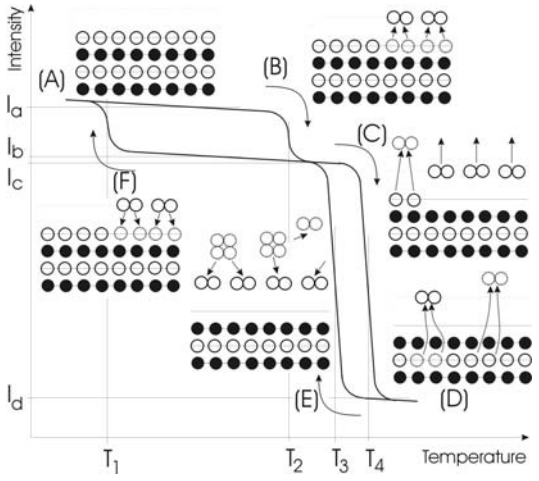

Figure 5
The qualitative explanation of the hystetesis in InAs with the absorption–desorption process

The roughening of the surface and the surface V/III ratio is closely linked during the heat treatment. The lower part of Fig. 3 shows this ratio change against temperature: In the case of (a): At low temperature (T_a) the surface is As terminated. The crystal surface is perfect to start with and the specular spot intensity is high. A small variation in the temperature changes the As at the surface to chemisorption 2 state or causes it to leave directly. This decomposition in the lower layers is less probable, and therefore the surface roughening is less likely. In the case of (b): Any further increase in temperature (T_b) chemisorbed As goes into chemisorption-2 state or leaves the surface. The layer of chemisorped As tends to provide a shield against decomposition in the deeper layers. The departure of As from the deeper layers is less likely, so the roughing effect on the surface is small. As a result, the specular spot intensity will drop. In the case of (c): At high temperature the As coverage on the surface is zero; therefore likelihood of the surface decomposition will increase, since As can leave the crystal from the deeper layers as well. It results in further roughening of the surface and a drop in the specular spot intensity to minimum, due to Ga coming to the surface.

Let us consider the As surface coverage (Θ), the surface roughness and the change in the specular spot intensity as the function of the temperature for an idealized semiconductor surface. The As surface coverage can be the result of the presence of chemisorbed atomic As (Θ_c) or the arsenic dimmer species (Θ_{c2}). In our model we will consider the near equal presence of the two form of As, in order to avoid further roughening of the surface. The resultant coverage therefore is the sum of the two coverages ($\Theta = \Theta_c + \Theta_{c2}$). Fig. 5 shows the intensity as a function of temperature. The curve follows the A-B-C-D path for increasing temperature, while it goes on the D-E-F-G path when the temperature decreases. Let us investigate now the surface in a few strategic places and the reason for the

hysteresis. In the state of (A) the temperature is low (T_1) and the As terminated surface reconstruction is (2x4). The surface is perfectly smooth and the specular spot intensity is at maximum (I_a). Between (A) and (B) the temperature grows (T_1-T_2), and therefore for the chemically bonded As atoms, is more difficult to leave the As terminated surface, due to the strong bond. (E_{As}). The minimum loss of arsenic results in minimum loss surface roughening. As a result the drop in specular spot intensity is minimal (~I_a). Due to the high activation energy of chemisorbtion, a noticeable change in the surface condition can only be the result of a significant increase in the temperature. In the A-B region, therefore, no significant change will occur ($\Theta = \Theta_c$). It should be noted that the chemisorbed As sticking coefficient is dependent on the coverage ($S_{cAs}(\Theta)$), which explains the noticeable intensity drop in the A-B region. In stage (B) the chemisorbed arsenic species can convert into dimerized state in large quantities ($\Theta = \Theta_{c2}$). The arsenic coverage does not change significantly, and therefore the intensity only changes slightly. Between (B) and (C) the chemisobtion state become vacant ($\Theta_c = 0$). In the (C) state and in the C-D range, small temperature variations can cause large sudden changes in the intensity. The dimer state can easily become vacant due to the low activation energy. The disappearance of most of the As from the surface represents a large change in the V/III ratio. As we have shown above this also results in a drop in the intensity of the specular spot (maximum surface roughness). The dimerisation sticking coefficient is a function of the coverage ($S_{c2As}(\Theta)$). In (D) the dimerized state becomes vacant (Θ_{c2}) and therefore the RHEED specular intensity is minimal.

Returning from (D) position, by reducing the temperature, the dimmers start setting in at a lower temperature, marked (E), due to the fact that the setting in process for As is far more complicated than the process of leaving the surface. The dimmers set in through the splitting of the tetramers, causing the hysteresis in the process. This is amplified by the shift, resulting from the recovery from the roughening of the surface. The second hysteresis loop has a similar explanation for the return leg.

2.3 Qualitative Description of the Reconstruction Induced RHEED Intensity Hysteresis

As we have shown before, the RHEED secular spot intensity has a strong relation to the surface stoichiometry. Less concentration of As and more metallic components represent higher, whilst the opposite brings lower spot intensity. In observing the intensity, however, we cannot neglect the surface morphology either. Generally speaking the absorption-desorption processes show hysteretic properties. The absorption-desorption depends on the state of the surface, therefore the species bound to the surface and leaving the surface first, face conditions substantially different to those leaving the surface last. This is applicable to the opposite process as well. The absorption-desorption processes of

the III-V materials are complex. The change in the secular spot intensity cannot be attributed entirely to the absorption-desorbtion process, although the surface coverage of As has a vital role in the phenomenon.

We can observe the change in the RHEED pattern during the temperature cycle. By observing a surface in quenched state through Atomic Force Microscopy (AFM) we can see that the surface is composed of domains of different states of reconstructions [30]. With changing temperature these domains will change their size at each other's expense. As a result, not only the distribution of the reconstructed domain will change but the composition map as well, all contributing to the change in the specular spot intensity.

Looking at the *I(T)* diagram (see Fig. 1) of InAs, we can find two hysteresis loops. One is at lower, another one at higher temperature. In case of GaAs one loop exists at lower temperature, while the other is a single line, which however can be regarded as a degenerated loop (see Fig. 6).

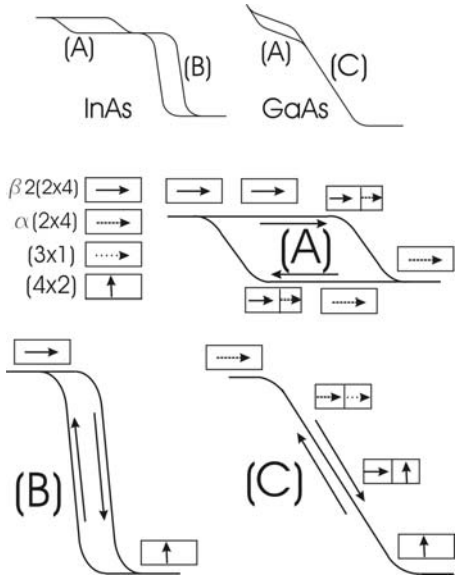

Figure 6
The qualitative explanation of the hystetesis in GaAs with the absorption –desorption process

Experimental evidence supports the view that in case of the higher temperature loop, the mid-temperature of the loop decreases with dropping As pressure, while its width increases at the same time. The experiments were carried out at different temperature settings but at the same pressure for both InAs and GaAs. It is quite possible that for GaAs, a second loop also exists at lower temperature. This leaves the question unanswered whether the comparison between GaAs and InAs was made at optimum conditions (temperature, As pressure, etc.) and how far these results are from optimum.

We saw that the *I(T)* diagram has two hysteresis loops, and in both cases, if we regard one, in the case of GaAs, as a degenerate loop. It is evident that each of the loops corresponds to one different surface process and these processes are coupled to one another. A spin valve has similar characteristics. The loop at low temperature has higher intensity; therefore it is linked to surfaces with higher As content and processes. In both regions the RHEED indicates (2x4) type surface reconstructions. With the (1x1) surfaces, with no reconstruction, the dangling bonds are pointing in [-110] direction [30].

The As rich reconstruction lines are forced to run in this direction. This surface symmetry can come in a number of reconstruction types: α(2x4), α2(2x4), β(2x4), β2(2x4), β3(2x4), γ(2x4) [30]. The transformation of these domain structures into each other is the cause of the hysteresis loops. The (2x4) domain energy levels are very close to each other. The high As content β2(2x4) type reconstruction forms first at lower temperature and this is followed gradually by the formations of the lower As content α(2x4), α2(2x4) type domains. The β2(2x4) type reconstructions are more stable than any of the previous ones, and therefore its lifetime is longer; it only transforms at higher temperatures and at a faster rate. This represents the upper part of the intensity curve. At decreasing temperatures, the reconstructions of low As content will materialize first, followed by the β2(2x4) reconstruction at the appropriate temperature. Because it is a more favorable atomic arrangement it accelerates the dominant process on the surface. The path of the intensity curve will be different, forming the lower branch of the hysteresis loop. The changes are not only the result of the variation in the temperature but also of the delay caused by the transformation of the phases into one another. In other words, during the spontaneous transformations between equal energy states the stable states will stay; therefore the growth of the domains will not be dependant solely on temperature. (The transformation takes up energy). The loop at lower temperature for GaAs is similar to that of InAs, because the polar surfaces in both cases are solely determined by the behaviour of the As. The process around the loop of InAs at higher temperature (and the pseudo loop of GaAs) is determined mostly by the metallic component, so the difference is greater.

We can observe the (4x2) reconstruction at higher temperatures, where the dimmer lines of the In/Ga propagate in [110] direction [39, 40]. It is obvious that for the InAs the [110] direction represents the pinned structure, causing the As rich “hard” hysteresis. As the temperature increases the pinning is destroyed, the surface transforms quickly into an In rich (2x4) surface, resulting in a sudden intensity drop. This is what causes the double loop “soft” branch. The intensity change in this loop is much greater than in the previous one, because the sudden disappearance of the As, against the gradual drop in As before.

The procedure for GaAs is different. The As rich (2x4) reconstruction is followed by another As rich (3x1) reconstruction [32], which overlaps with the Ga rich (4x2) reconstruction. This is why we can assume the domain like transformations. The transformations here are not at all like those of the two state systems of InAs.

This is rather similar to the loop at lower temperature. Because the reconstructions here differ greatly energy wise as well as structurally, the speed up and the slow down effects of the domain interactions are not present. We can also assume that, the roughness of the surface plays an important role in the intensity change due to the varying structure and layering. It is possible therefore that the temperature sweep in both directions would result in the same intensity versus temperature curve.

2.4 Modeling of the Hysteresis in the RHEED Intensity

Although hysteresis has been known for a long time and well documented, coupled hysteretic systems spin–valves were only discovered forty years ago [41]. Its counterpart, the inverse spin–valve, is less than ten years old [42]. Although the phenomenon described in this paper is far removed from the physical mechanism of inverse spin-valves, its general character is strikingly similar. In general terms, the spin-valve effect involves two coupled hysteretic processes and is characterized by two hysteresis loops flowing into each other as the excitation varies periodically. Although there are a number of known models for describing hysteresis in magnetism, e.g. Preisach, Jiles, Stoner-Wohlfart, etc. [43-45], so far it is only the *T(x)* hyperbolic model which can describe this rather complex phenomenon of two coupled hysteretic processes, forming a spin-valve character, on non magnetic terms [46]. The hyperbolic model has successfully been applied in several cases [47, 48].

The model is based on the Langevin's theory of ferromagnetism and well described in literature [41]; therefore here only a brief reminder will be given to the reader. For further information the reader is referred to the literature.

In the hyperbolic model each of the independent constituent components are identified and formulated by their separate hyperbolic functions. The components are separately analyzed and then linearly superimposed using Maxwell's superposition principle. The fundamental equations are shown in normalized canonic form:

$$y_{+n} = \sum_{k=1}^{n} (A_k f_{+k} + b_k) \tag{1}$$

$$y_{-n} = \sum_{k=1}^{n} (A_k f_{-k} - b_k) \tag{2}$$

$$b_k = \frac{A_k}{2}[f_{-k}(x_m) - f_{+k}(x_m)] \tag{3}$$

$$f_{\pm k} = \tanh \alpha_k (x \mp a_{0k}) \tag{4}$$

Here y is the RHEED specular spot intensity in normalized form, A is the intensity amplitude (maxima), is the speed of the process or reaction, a_0 is the measure of the hysteresis, x_m is the maximum temperature swing used in the experiment and n is the number of components present in the process (for spin-valve like systems n=2 for both the ascending and the descending branch). The positive and the negative sign represent the ascending and the descending branch within a single loop respectively. In spin-valve like processes the two coupled loop has opposite hysteretic rotation, represented by the opposite sign of their a_0 parameter.

The model leads to the calculation of the activation energy of each of the constituent processes involved in the surface reconstruction. Following Boltzman's relations [49, 50] the . activation energy involved in each leg of the hysteresis loop can be calculated as $\varepsilon = \alpha(x - a_0)kT$, where is the inclination of the leg of the loop in K^{-1}, representative of the speed of the process or reaction at $x = a_0$ temperature (in K) including hysteresis, k is the Boltzman constant and T is the mid temperature of the processes in K [4, 51].

During calculations we assumed a linear relationship between the surface process and the RHEED specular spot intensity. In order to refine our results, presented here, further tests are planned to check the influence of the method of detection and the linearity of the instrumentation used, on the experimental results.

2.4.1 The Hysteretic Phenomenon in Case of InAs

The hysteresis in the RHEED specular spot intensity occurs between 425 °C and 475 °C for InAs surface. This temperature range is low relative to other substances like GaAs, indicating lower binding forces, supported by the lower thermo-stability [6]. With gradually increasing temperatures, the desorption of the As will increase, changing the ratio on the surface between As and the III/As in favour of the metallic component. It is known from observations that, during heat treatment, the As background will vanish and after a time a continuous layer of Ga will form on the surface. As a result the RHEED picture becomes diffused and the specular spot blends into the background [25]. The same happens when the surface is subjected to metallic flux without the presence of As. We can assume a strong relation between the intensity of the specular spot and the presence of the metallic substance in the upper surface layer. This is supported by the ongoing (2x4) and (4x2) reconstructions. Within the investigated temperature range there are two interactive hysteresis loops, as depicted in Fig. 7, showing the measured loop and the one predicted by the model. The parameter values (normalized and in physical units) used in the calculations, representing the best fit to the experimental data, are tabulated in Table 1. This table also includes the energies involved in the individual processes.

Table 1
The numerical parameters of InAs hysteresis loop calculated from the model

		Amplitudes in arbitrary units		Speed of process normalized		Speed of process in /C^0 units		Hysteresis T normalised		Hysteresis T in C^0 units		Energy in eV	
	T C	A_1	A_2	$_1$	$_2$	$_1$	$_2$	a_{01}	a_{02}	a_{01}	a_{02}	$_1$	$_2$
Up	440	1.5	0.2	25	17.5	0.4	0.28	0.25	-0.17	15.62	-10.65	-1.00	-0.24
Down		1.5	1.5	25	17.5	0.4	0.28	-0.1	0.65	-6.25	40.62	-0.76	0.26
Up	471.5	1.5	0.2	25	17.5	0.4	0.28	0.25	-0.17	15.62	-10.65	-0.16	0.381
Down		1.5	1.5	25	17.5	0.4	0.28	-0.1	0.65	-6.25	40.62	0.112	0.92

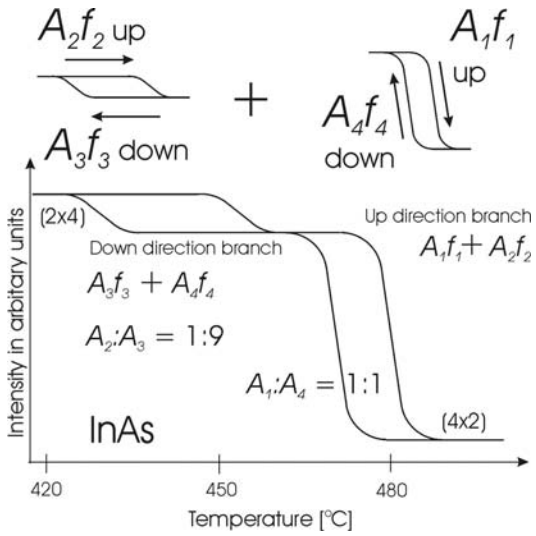

Figure 7
Measured and modeled InAs *I(t)* loops showing the inverse spin-valve effect involving two coupled hysteretic processes, characterized by two hysteresis loops

This first successful modeling of the phenomenon has far reaching implications. The model predicts that there are two separable, simultaneous coupled processes taking place on the surface of InAs crystals at a given time. In one temperature cycle, in both cases, the up and down processes involves two single simultaneous physical processes, namely the surface morphology and the surface stoichiometry. Each of the four processes is described by one separate function in the model. In the phase of up-going temperature the dominant process is stoichiometric, representing nearly 85% of the RHEED intensity changes. The rest is due to the changes in morphology. However, when the temperature is decreasing, the

contributions of the two processes are equal (50%-50%). This finding strengthens the physical explanation given before and the results of the RHEED studies carried out on InAs.

2.4.2 The Hysteretic Phenomenon in Case of GaAs

The hysteresis in the RHEED specular spot intensity occurs between 545 °C and 610 °C for GaAs surface. This temperature range is higher than that of InAs, as shown before, indicating higher binding forces. The (2x4) and (3x1) surface reconstructions as well as the (3x1) and (4x2) dominating the process are the same as before for the InAs. This represents a temperature shift in the region where the same surface forces come into play at higher temperature. The first loop of 16.8 °C wide appears at the lower end of the range. The loop at higher temperatures is degenerative. This is a phenomenon which is not uncommon in the spin-valve character. The loop, predicted by the model, gives a good fit to the measured specular spot intensity versus temperature *I(T)* curve as shown in Fig. 8.

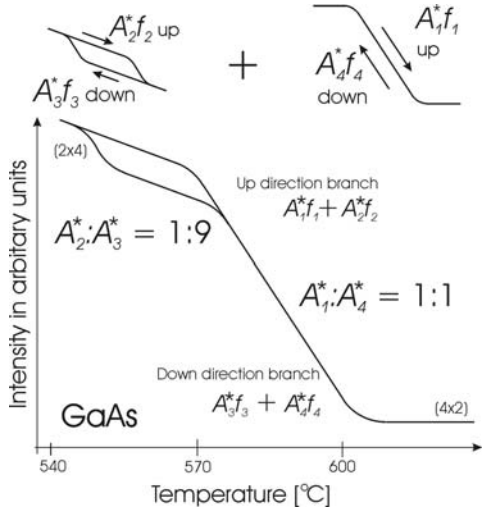

Figure 8

Measured and modeled GaAs *I(t)* loops showing the inverse spin-valve effect involving two coupled hysteretic processes, characterized by two hysteresis loops

Although the model predicts the presence of a very narrow loop in the GaAs intensity plot at higher temperatures as well, its width is probably within the experimental error. It is interesting to note that while the physical parameters used in modeling are different for the two substances the approximate ratios between the amplitudes (A_n) remained nearly the same. This is a good indication that although the range of temperature shifted, the surface reactions are the same for the two experimental substances as we have initially assumed. The best fitting numerical parameters and the appropriate energy values are tabulated in Table 2.

Table 2
The numerical parameters of GaAs hysteresis loop calculated from the model

GaAs	T C^0	Amplitudes in arbitrary units		Speed of process normalized		Speed of process in /C^0 units		Hysteresis ΔT normalised		Hysteresis ΔT in C^0 units		Energy in eV	
		A1	*A2*	$\alpha 1$	$\alpha 2$	$\alpha 1$	$\alpha 2$	*a01*	*a02*	*a01*	*a02*	ε1	ε2
Up	562	1.5	0.2	4	6	0.0246	0.037	0.1	0.1	16.21	16.21	-0.065	-.0108
Down		1.5	1.5	6	5.5	0.037	0.0339	0.52	0.1	84.32	16.21	-0.0898	0.19
Up	588	1.5	0.2	4	6	0.0246	0.037	0.1	0.1	16.21	16.21	0.007	0.1
Down		1.5	1.5	6	5.5	0.037	0.0339	0.52	0.1	84.32	16.21	0.01	0.309

Conclusion

In former literature, the RHEED intensity variation in InAs es a GaAs has a completely different interpretation, attributed to different physical processes [1]. The one in InAs is described as a first order phase transition, whilst the one in GaAs is regarded as a second order phase transition. We propose in this paper that the driving force in this kind of surface phenomenon is the same for both of the investigated substances with only a different emphasis on its constituent components. The model predicted the presence of two hysteresis loops in both cases, showing the two processes involved. (At higher temperatures, in the case of GaAs the second loop is present but narrow or degenerate). The model describes in both cases with identical formulation using the same physical parameters with different numerical values. This shows a logical approach and points towards a unified way of describing the phenomena without introducing different interpretations in each individual case. We also pointed out that the double hysteresis loop is due to the absorption-desorption process and the changing, domain-structured surface morphology (surface reconstruction). The explanations, given for the intensity change, are the stoichiometry, polarization and surface roughness. We can distinguish between a soft and a hard loop, which also characterizes the spin-valve configuration. The constituent processes causing the double hysteresis loop (absorption-desorption and the changing reconstructions) affect the phenomenon in a different way when the temperature increases or decreases. The model showed that whilst the two processes play an equal role (approximately1:1) when the temperature decreases, this ratio is substantially different (approximately 3:1) when the temperature is on the increase, due to the kinetics of As incorporation.

References

[1] B. A. Joyce, J. H. Neave, J. Zhang, P. J. Dobson: RHEED Intesity Osscillations during MBE Growth of III-V Compounds; in Reflection High-Energy Electron Diffraction and Reflection Electron Imaging of Surfaces (Eds. P. K. Larsen and P. J. Dobson) Plenum Press, New York (1987) pp. 397-417

[2] B. A. Joyce, D. D. Vvedensky: Quantum Dots in the InAs/GaAs System; in Quatum Dots: Funtamentals, Applications and Frontiers, Springer, Dorndrecht (2005) pp. 1-26 (Eds.: B. A. Joyce, P. C. Kelires, A. G. Naumovets, D. D. Vvedensky)

[3] H. Yamaguchi, Y. Horikosi: Surface Structure Transitions on InAs and GaAs (001) Surfaces; PRB, Vol. 51 (1995), pp. 9836-9854

[4] J. Takács: Mathematics of Hysteretic Phenomena – The T(x) Model for the Description of Hysteresis; Wiley-VCH Verlag GmbH & Co, Weinheim (2003)

[5] C. T. Foxon, B. A. Joyce: Interaction Kinetics of As_4 and Ga on (001) GaAs Surfaces Using Modulated Molecular Beam Technique; Surf. Sci. 50 (1975) 434-450

[6] C. T. Foxon, B. A. Joyce: Interaction Kinetics of As_2 and Ga on (100) Surfaces; Surf. Sci. 64 (1977) 293-304

[7] J. H. Neave, P. K. Larsen, J. F. van der Veen, P. J. Dobson, B. A. Joyce: Effect of Arsenic Species (As_2 or As_4) on the Crystalographic and Electronic Structure of MBE-Grown GaAs(001) Reconstructed Surfaces; Surf. Sci. 133 (1983) 267-278

[8] Y. Fukunishi, H. Nakatuji: Cluster Model Study on GaAs Epitaxial Crystal Growth by Arsenic Molecular Beam, As_2 Adsorption on GaAs Surface; Surf. Sci. 291 (1993) 271-280

[9] E. S. Tok, J. H. Neave, F. E. Allegretti, J. Zhang, T. S. Jones, B. A. Joyce: Incorporation Kinetics of As_2 and As_4 on GaAs(110); Surf. Sci. 371 (1997) 277-288

[10] E. S. Tok, J. H. Neave, J. Zhang, B. A. Joyce, T. S. Jones: Arsenic Incorporation Kinetics in GaAs(001) Homoepitaxy Revisited; Surf. Sci. 374 (1997) 397-405

[11] R. Venkatasubramanian, V. K. Pamula, D. L. Dorsey: Influence of Physisorbed on RHEED Intensity Oscillations during Low-Temperature GaAs Molecular Beam Epitaxy; Appl. Surf. Sci. 104/105 (1966) 448-454

[12] A. Suda, N. Otsuka: Surface Atomic Process of Incorporation of Excess Arsenic in Molecular-Beam Epitaxy of GaAs; Surf. Sci. 458 (2000) 162-172

[13] B. A. Joyce; in Two Dimensional Systems: Physics and New Devices, G. Bauer, F. Kucher, H. Heinrich eds. (Springer Ser. In Solid State Sci. 67, Springer-Verlag, Heidelberg (1986)

[14] Á. Nemcsics, J. Olde, M. Geyer, R. Schnurpfeil, R. Manzke, M. Skibowski: MBE Growth of Strained InGaAs on GaAs(001); Phys. Stat. Sol. A 155 (1996) 427-437

[15] Á. Nemcsics: Behaviour of RHEED Oscillation during LT-GaAs Growth; Acta Politechn. Hung. 4 (2007) 117-123

[16] B. A. Joyce, J. H. Neave, J. Zhang, P. J. Dobson: RHEED Intensity Oscillation during MBE Growth of III-V Compounds; in Reflection High-Energy Electron Diffraction and Reflection Electron Imaging of Surfaces; NATO ASI Ser. 188, Plenum Press New-York (1988) 397-417

[17] W. Braun, L. Däweritz, K. H. Ploog: Origin of Electron Diffraction Oscillations during Crystal Growth; Phys. Rev. Lett. 80 (1998) 4935-4938

[18] W. Braun: Applied RHEED, Reflection High-Energy Electron Diffraction during crystal growth; Springer-Verlag, Berlin (1999)

[19] Z. Mitura, S. L. Dudarev, M. J. Whelan: Phase of RHEED Oscillations; Phys. Rev. B 57 (1998) 6309-6312

[20] Z. Mitura: Interactive Method of Calculating Reflection High-Energy-Electron-Diffraction Intensities; Phys. Rev. B 59 (1999) 4642-4645

[21] Z. Mitura, S. L. Dudarev, M. J. Whelan: Interpretation of Reflection High-Energy Electron Diffraction Oscillation Phase; J. Cryst. Growth 198/199 (1999) 905-910

[22] J. M. McCoy, U. Korte, P. A. Maksym, G. Meyer-Ehmsen: Multiple Scattering Evaluation of RHEED Intensities from the GaAs(001)-(2x4) Surface; Phys. Rev. B 48 (1993) 4721-4728

[23] Á. Nemcsics: The Initial Phase Shift Phenomenon of RHEED Oscillations; J. Cryst. Growth 217 (2000) 223-227

[24] Q.-K. Xue, T. Hashizume, T. Sakurai: Scanning Tunneling Microscopy of III-V Compound Semiconductor (001) Surface; Prog. Surf. Sci. 56 (1997) 1-137

[25] M. Witte, G. Meyer-Ehmsen: RHEED Structure Analysis of the GaAs(001)2x4 Surface for Azimuths [110] and [010]; Surf. Sci. 326 (1995) L449-L454

[26] J. M. McCoy, U. Korte, P. A. Maksym: Determination of the Atomic Geometry of the GaAs(001)2x4 Surface by Dynamical RHEED Intensity Analysis: the β2(2x4) Model; Surf. Sci. 418 (1998) 273-280

[27] F. Bastimann, A. G. Cullis, M. Hopkinson: GaAs(001) (2x4) to c(4x4) Transformation Observed in-situ by STM during As flux Irradiation; Surf. Sci. 603 (2009) 2398-2402

[28] K. Shiraishi, T. Ito: Atomic and Electronic Structures of Surface Kinks on GaAs(001) Surfaces; Appl. Surf. Sci. 121/122 (1997) 98-101

[29] S. Tsukamoto, N. Koguchi: Magic Numbers in Ga clusters on GaAs(001) Surface; J. Cryst. Growth 209 (2000) 258-262

[30] A. Ohatke: Surface Reconstruction on GaAs(001); Surf. Sci. Rep. 63 (2008) 295-327

[31] B. A. Joyce, D. D. Vvedensky: Self-organized Growth on GaAs Surfaces; Mat. Sci. Eng. R 46 (2004) 127-176

[32] C. Deparis, J. Massies: Surface Stochiometry Variation Associated with GaAs (001) Reconstruction Transitions; J. Cryst. Growth 108 (1991) 157-172

[33] Á. Nemcsics, Ch. Heyn, A. Stemmann, A. Schramm, H. Welsch, W. Hansen: The RHEED Tracking of the Droplet Epitaxial Grown Quantum Dot and Ring Structures; Mat. Sci. Eng. B (2009) in press

[34] J. F. van der Veen, L. Smir, P. K. Larsen, J. H. Neave: Core Level Binding Energy Shift for Reconstructed GaAs(001) Surfaces; Physica B 117 (1983) 822-824

[35] C. Sasaoka, Y. Kato, A. Usui: Temperature Programmed Desorption Study of GaAs(100)-c(4x4) and As_4 Exposed (2x4) Surfaces; Surf. Sci. Lett. 265 (1992) L239-L244

[36] R. Kaspi, S. A. Barnett: Analysis of GaAs(001) Surface Stochiometry using Monte Carlo Simulations; Surf. Sci 241 (1991) 146-156

[37] I. Chizov, G. Lee, R. F. Willis, D. Lubysev, D. L. Miller: Scanning Tunneling Microscopy Study of the Evolution of the GaAs(001) Surface during the (2x4)-(4x2) Phase Transition; Appl. Surf. Sci. 123/124 (1998) 192-198

[38] M. Larive, G. Jezequel, J. P. Landesman, F. Soal, J. Nagle, B. Lépine, A. Taleb-Ibrahimi, G. Indelkofer, X. Marchadet: Photoelectron Spectroscopy Study of Ga 3d and As 3d Core Levels on MBE-Grown GaAs Surfaces; Surf. Sci. 304 (1994) 298-308

[39] J. Behrend, H. Wassermeier, K. H. Ploog: Different As Desorption Behaviour at Steps Edges on InAs(001) and GaAs(001) Surfaces; Surf. Sci. 372 (1997) 307-311

[40] I. Chizov, G. Lee, R. F. Willis, D. Lubisev, D. Miller: Scanning Tunneling Microscopy Study of the Evolution of the GaAs(001) Surface during the (2x4)-(4x2) Phase Transition; Appl. Surf. Sci. 123/124 (1998) 192-198

[41] J. Takács: A Phenomenological Matematical Model of Hysteresis; COMPEL Int. J. Comp. El. 20 (2000) 2002-2014

[42] L. K. Varga, Gy. Kovacs, J. Takacs: Modelling the Overlapping, Simultaneous Magnetization Processes in Ultrasoft Nanocrystalline Alloys; J. Magnetism & Magn. Mat. 320 (2008) L26-L29

[43] F. Preisach: Über die magnetische Nachwirkung; Z. Phys. 94 (1935) 227-230

[44] D. C. Jiles, D. L. Atherton: Theory of Ferromagnetic Hysteresis; J. Appl. Phys. 55 (1984) 2115-2119

[45] E. C. Stoner, E. P. Wohlfarth: Hysteresis Modeling of Recording Media with as Interacting; IEEE Trans. on Magn. 27 (1991) 3475-3479

[46] J. Takács, I. Mészáros: Separation of Magnetic Phases in Alloys; Physica B 403 (2008) 2293-2297

[47] I. Mészáros: Magnetic Characteization of Phase Transformations in Trip Steels; J. El. Eng. 59 (2008) 1-4

[48] I. Mészáros: Hyperbolic Model Based Data Evaluation for Magnetic NDE Measurements; Mat. Sci Forum 589 (2008) 251-256

[49] L. Boltzman: Vorlesungen über Gastheorie; J. A. Burth, Leipzig, (1896)

[50] E. H. Kennard: Kinetic Theory of Gases; McGraw-Hill, New York (1938)

[51] J. Takács: Energy Consideration of the T(x) Model of Hysteresis; COMPEL Int. J. Comp. El. 24 (2005) 220-228

Gray-Box Modeling of a Pneumatic Servo-Valve

Farhad Toorani, Hosein Farahmandzad

Moghtader Engineering Company
Tehran, Iran
E-mail: toorani.farhad@gmail.com, h.farahmandzad@gmail.com

Mojtaba Aghamirsalim

Department of Electrical Engineering
Amirkabir University of Technology
Tehran, Iran
E-mail: mirsalim@aut.ac.ir

Abstract: This paper presents the evaluation as well as the combined analytical and experimental identification (gray box identification) of a servo-valve torque motor as the directional valve applied in a pneumatic actuator. Based on analytical modelling, a simple linear parametric model with transfer function and block diagram is developed. Next, the static and dynamic characteristics of the torque motor are obtained from experimental observations. The characteristics confirm the desired linear behaviour of the torque motor. Hence, linearized coefficients from a best curve fitting of static characteristics can be derived. Classical methods of identification are applied on the frequency and step responses obtained from a set of tests on the torque motor. Obtained tests results based on parsimony principle and model order of analytical investigations are then implemented to derive the best identified transfer function to describe the performance of the servo-valve torque motor. Design parameters are estimated with the comparison of the experimental and analytical models. These parameters can be implemented with acceptable accuracy for servo control studies of pneumatic actuators.

Keywords: pneumatic actuator; servo-valve; limited angle torque motor; gray box modeling

1 Introduction

Several advantages of pneumatic actuation systems over hydraulic and electromechanical actuation systems in positioning applications have caused their

wide application in industrial automation, motion control of materials and part handling, packaging machines, and in robotics. The advantages include low cost, cleanliness, ease of maintenance, and high power to weight ratio. The drawback is due to the compressible nature associated with gases and the high speeds, which make it more difficult to control.

An electro-pneumatic control valve plays an important role in a pneumatic actuator. Its characteristics influence remarkably the performance of the actuator. This power element with small-amplitude, the low power electrical signal provides a high response modulation in pneumatic power. The dynamic response, null shift, threshold, and hysteresis are the most critical parameters that strongly influence the dynamic and static characteristics of the pneumatic actuators [1]. Limited angle torques motors (LATMs) are one of the electromechanical transducers which, when integrated with nozzles, can be used as servo-control valves in either pneumatic or hydraulic actuators. They can serve as proportional displacement, force output, or both.

Hydraulic servo-valves as a vital part of hydraulic actuation systems have been studied in literature. In [2, 3], the influence of magnetic fluids on the dynamic characteristics of a hydraulic servo-valve has been simulated and tested. LATMs are implemented as limited-motion rotary actuators in many areas of measurement, control, and energy conversion applications through an angle of less than ±180º. In [4], [6] a form of LATM, which is based on Laws' relay principle [5], has been evaluated and analyzed. The performance of this kind of torque motor is based on polarized reluctance principle in which torque and EMF are produced based on flux-switching action of rotor saliencies on a permanent magnet flux. Many complex problems of Laws' relay in rotary and rectilinear versions [7, 8], have been restricted to design problems which contain static and dynamic characteristics, e.g. stiffness of permanent magnets and torque sensitivity with respect to current.

The design and control of a two-pole toroidally wound armature brushless direct-current LATM with application in the fuel control of gas-turbine engines has been presented in [9]. To achieve a robust position control of the motor, a PID controller with a closed-loop fuel controller has been implemented using DSP.

The construction of servo-valve studied in our research is a type of Laws' relay which contains two windings set up on two bobbins placed around the rotor as control coils. This structure lowers the physical size, and the bobbins play the role of position limiters. The stator contains two separated soft iron yokes and two permanent magnets with high flux densities. The main characteristics of the motor are its miniature size, the capability of the rotor to revolve only up to ±3º, short dynamic response time due to its low inertia and the high magnetic stiffness that is desirable in servo-valves, high reliability due to its simple construction and the high quality of magnetic material.

This paper presents a combined analytical (white box) and experimental (black box) modeling of a pneumatic servo-valve torque motor, based on an approximate mathematical model developed from design data and experimental measurements. The black box modeling approach is the basis of system identification which estimates dynamic response and transfer function parameters. This approach is simpler than solving the nonlinear partial differential equations of the structure, and is especially suitable for design studies of the control loop of the pneumatic actuator when used as an accurate position tracker. Based on classical methods of identification, the frequency and step responses of the tested motor have been fitted by a continuous transfer-function response. The unknown parameters of a mathematical model are derived according to the presented models. The experimental results show that the proposed models provide an accurate prediction of the behavior of servo-valve torque motors.

2 Laws' Relay Principles

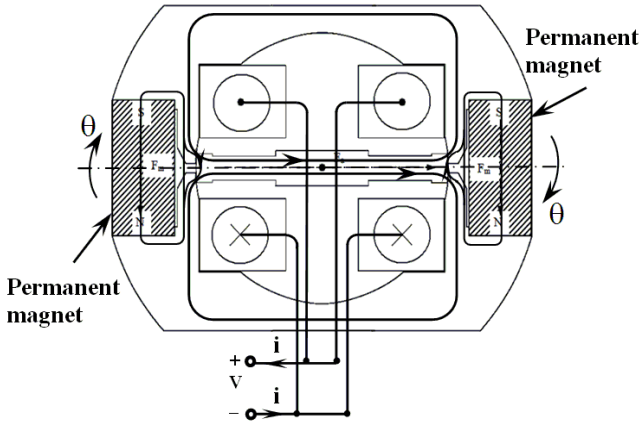

Figure 1
The schematic of Laws' relay servo-valve

A schematic of the tested torque motor is shown in Figure 1. It contains armature, two parallel coils, two permanent magnets, and yokes. Four core teeth overlap with armature and cause four variable air-gap reluctances, which make the motor act as a switch reluctance type. The two magnets tend to keep the armature in a null position ($\theta = 0$). With no external excitation, the flux density under each of the four teeth is equal and the low inertia of the rotor bridge poles causes a magnetic balance in the four air-gaps. By connecting a power source that can supply either unidirectional or bipolar current to the motor, an unbalance of flux density in the air-gaps is produced, which results in a new equilibrium of rotor

position. Inherently, the high stiffness of the magnet makes it like a spring with a stiffness torque proportional to the angular position. Since the torque produced by the flux of the control winding is proportional to the current (under non-saturated conditions), theses two components of the torque make the motor suitable for servo control systems and accurate positioning of a load connected to an actuator. A pneumatic nozzle is linked to the armature of the torque motor and the whole system acts as a directional-proportional valve that guides compressed air to cylinder chambers.

3 Mathematical Model of a LATM

The mathematical model of the Laws' relay system is based on the dynamic equations of motor which are described by the following differential equations.

$$\begin{aligned} & v-\left(\frac{\partial\lambda(i,\theta)}{\partial\theta}\right)\frac{d\theta}{dt}-\left(\frac{\partial\lambda(i,\theta)}{\partial i}\right)\frac{di}{dt}-Ri=0 \\ & \Rightarrow i(t)=\int\left[\left(\frac{\partial\lambda(i,\theta)}{\partial i}\right)^{-1}\left(v-Ri-\left(\frac{\partial\lambda(i,\theta)}{\partial\theta}\right)\frac{d\theta}{dt}\right)\right].dt \end{aligned} \tag{1}$$

$$T_m = J\frac{d^2\theta}{dt^2}+K_f\frac{d\theta}{dt}+T_s(\theta)$$

$$v-\left(\frac{\partial\lambda(i,\theta)}{\partial\theta}\right)\frac{d\theta}{dt}-\left(\frac{\partial\lambda(i,\theta)}{\partial i}\right)\frac{di}{dt}-Ri=0$$

$$\Rightarrow i(t)=\int\left[\left(\frac{\partial\lambda(i,\theta)}{\partial i}\right)^{-1}\left(v-Ri-\left(\frac{\partial\lambda(i,\theta)}{\partial\theta}\right)\frac{d\theta}{dt}\right)\right].dt$$

$$n(t)\triangleq\frac{d\theta}{dt}\Rightarrow n(t)=\int\left(J^{-1}(T_m-K_f n-T_s)\right).dt \tag{2}$$

Here, flux linkage, $\lambda(i,\theta)$, is a nonlinear function of current i and angular position θ . T_m , T_s and K_f denote the motor developed torque, the stiffness torque, and the frictional coefficient of air, respectively. $n(t)$ is the motor speed, and finally J is the moment of inertia of bundle of rotor and nozzle, [2].

Because of the small range of operation of θ (±3º), it can be assumed that T_m is directly proportional to current i, stiffness torque T_s is directly proportional to

position θ, and the differential term $\partial\lambda/\partial\theta$ is approximately constant. If the other differential term $\partial\lambda/\partial i$ is approximated to a constant value, then an acceptable linear model can be defined by the following equations:

$$v - K_b \frac{d\theta}{dt} - L\frac{di}{dt} - Ri = 0 \tag{3}$$

$$T_m = J\frac{d^2\theta}{dt^2} + K_f \frac{d\theta}{dt} + T_s \tag{4}$$

Where,

$$T_s = K_s\theta \tag{5}$$

$$T_m = K_t i \tag{6}$$

Substituting T_s and T_m from eqns. (5) and (6) into eqn. (4) gives

$$K_t i = J\frac{d^2\theta}{dt^2} + K_f \frac{d\theta}{dt} + K_s\theta \tag{7}$$

By substituting *i* from eqn. (7) into eqn. (3), the following equation is obtained:

$$\begin{aligned} &v - K_b\frac{d\theta}{dt} - L\frac{d}{dt}\left(\frac{J}{K_t}\frac{d^2\theta}{dt^2} + \frac{K_f}{K_t}\frac{d\theta}{dt} + \frac{K_s}{K_t}\theta\right) \\ &-R\left(\frac{J}{K_t}\frac{d^2\theta}{dt^2} + \frac{K_f}{K_t}\frac{d\theta}{dt} + \frac{K_s}{K_t}\theta\right) = 0 \end{aligned} \tag{8}$$

Consequently, the parametric transfer function of Laws' relay as a system input system output (SISO) can be derived in a third order form as in the following:

$$\begin{aligned} G(s) &= \frac{\theta(s)}{V(s)} \\ &= \frac{K_t/JL}{S^3 + \left(K_f/J + R/L\right)S^2 + \left((RK_f + K_bK_t + K_sL)/JL\right)S + RK_s/JL} \end{aligned} \tag{9}$$

4 Torque Motor Performance

Because of the low working frequency of 1 Hz for this servo-valve, the static characteristics have more important effect on dynamic performance compared to the typical ones used in aerospace equipment and optical scanning systems.

The measured magnitude of the magnetic stiffness torque for each position of shaft deflection in the range of ±3º is shown in Figure 2. It is obvious that this characteristic with a good approximation has a linear behavior, which confirms the linear coefficient of K_s. From the best linear curve fitting, the following value is obtained for this coefficient:

$$K_s = 1.1\,Nm/rad = 0.01921\,Nm/\deg \tag{10}$$

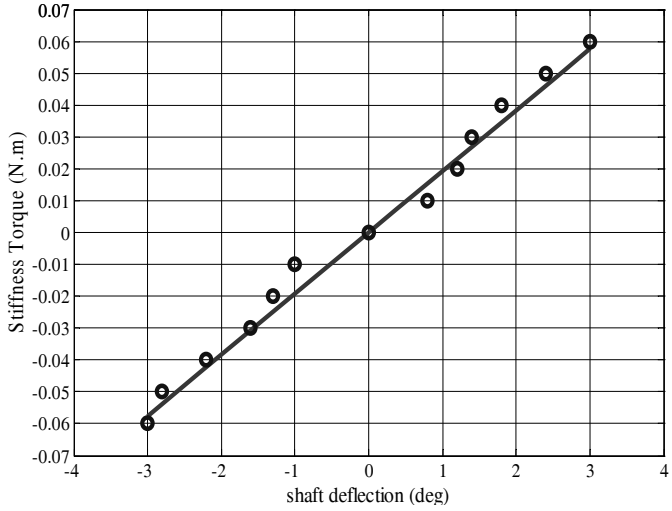

Figure 2
The measured stiffness torque characteristic and the best fit curve

The torque-current characteristic of the motor shown in Figure 3 has been obtained by exciting its coil with a variable DC source. The figure shows a good linear trend which again confirms the linear coefficient of K_t. From the best linear curve fitting, the following value is obtained for this coefficient:

$$K_t = 6.432\,Nm/A \tag{11}$$

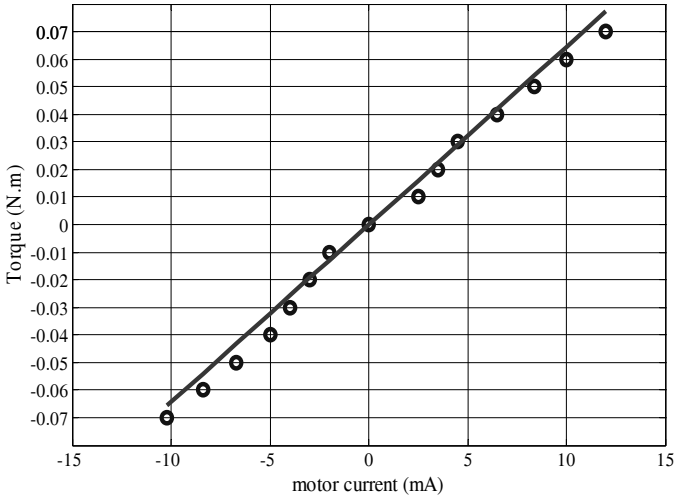

Figure 3
The measured torque-current characteristic and the best fit curve

Figure 4 presents the steady-state characteristic of the experimental LATM operating in the open loop conditions. The voltage-position characteristic demonstrates that with a desirable linear performance, the motor can be implemented in servo control systems.

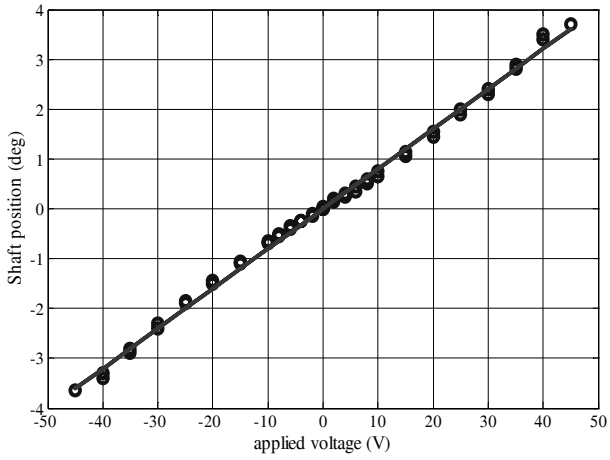

Figure 4
The measured voltage-position characteristic and the best fit curve

The approximately ideal characteristics of the designed parameters in Figures 3 and 4 present a good linear model for the controller design procedure. The measured parameters are summarized in Table 1.

Table 1
Measured parameters of available LATM

Torque constant $K_t\left(Nm/A\right)$	6.432
Back EMF constant $K_b\left(V.s/rad\right)$	0.08
Winding resistance $R(\Omega)$	3630
Winding inductance $L(H)$	34
Rotor inertia $J\left(kg.m^2\right)$	7.246×10^{-7}
Frictional coefficient $K_f\left(Nm.s/rad\right)$	2.7×10^{-4}
Magnetic stiffness $K_s\left(Nm/rad\right)$	1.1

A block diagram representation of the torque motor is shown in Figure 5 to illustrate the dynamic performance of its linear model. In this figure, the resistance R is measured directly from voltage and current measurements, the moment of inertia J is calculated accurately by SolidWorks software, and the winding inductance is approximately calculated based on analysis of the current flow of motor when excited with low frequency sinusoidal voltage. Figure 6 shows the sinusoidal input voltage and time-response waveforms of current and the position of motor at a frequency of 10 Hz.

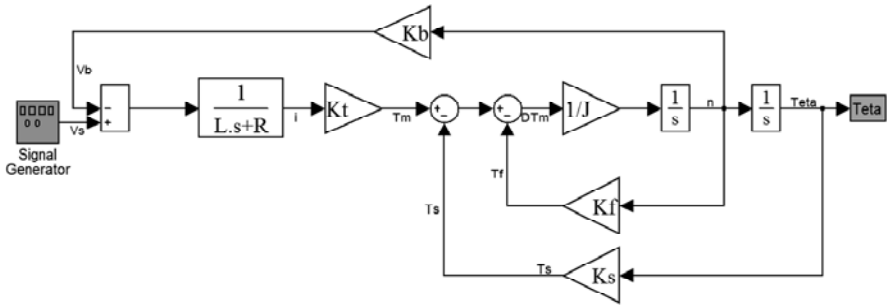

Figure 4
Block diagram of a LATM

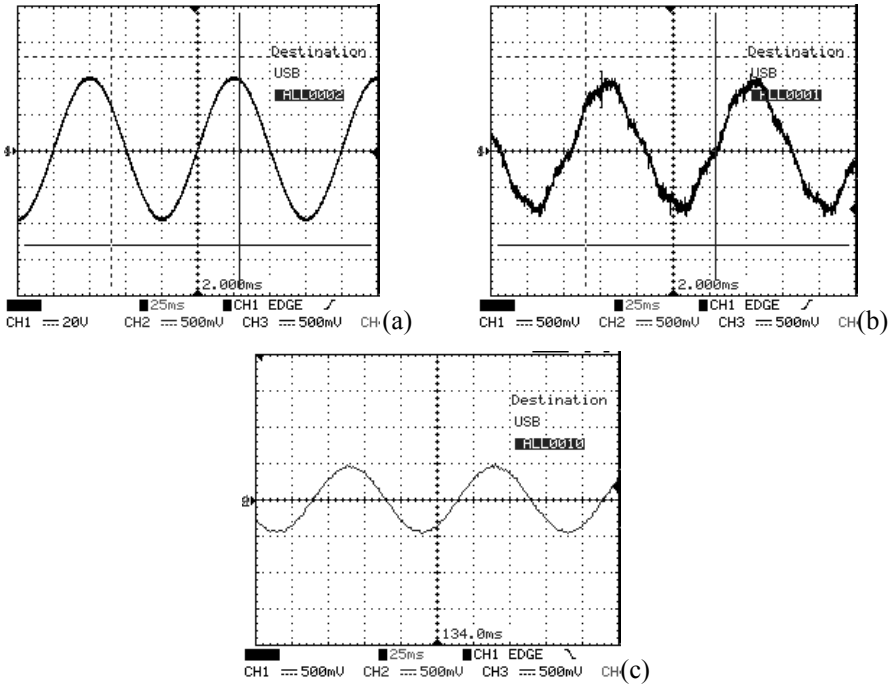

Figure 6

(a) 10Hz sinusoidal input, 40V peak (b) Time-response waveform of current (c) Time-response waveform of position

The frictional constant K_f, and back EMF coefficient K_b are difficult to measure directly. Hence, they are estimated from the predicted transfer function in the next section.

The experimental test system, consisting of the torque motor, a function generator with its output signal amplified by a voltage amplifier circuit, current sensor, and an arc type potentiometer fed by ±500 mV voltage with its wiper (contact arm) soldered to an arm linked to the motor shaft is shown in Figure 7.

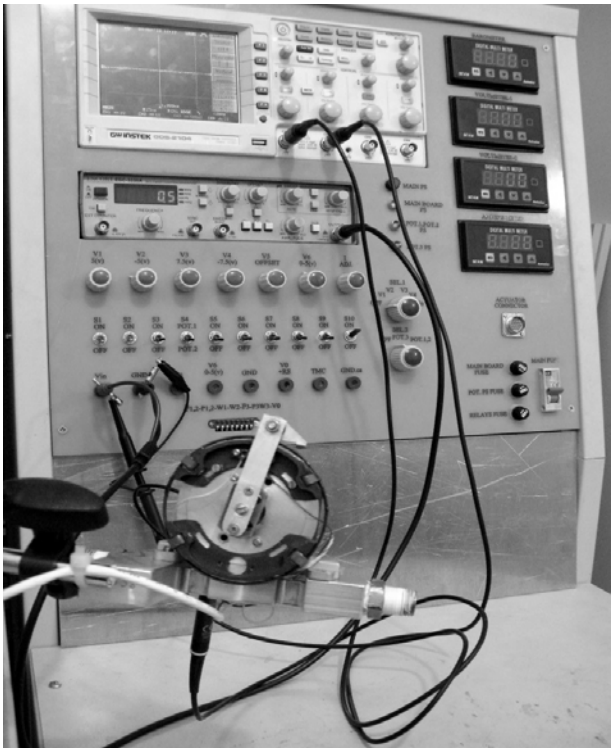

Figure 7
The experimental measurement system

5 Classical Identification

In linear time-invariant SISO dynamic systems, it is possible to derive the linear transfer function model by analyzing the response of the system to any forcing input. The step and frequency response tests are two common practical methods in classical identification [10]. The step response of a third-order system closely resembles to that of a first-order system with just tracking swings. According to the parsimony principle of model order determination [11], the simpler model can be chosen between two models with orders n_1 and n_2 ($n_1 > n_2$), if it adequately and accurately describes the system. However, in this case, because we consider the combined analytical and experimental models, it is necessary to choose the third-order model. Hence, by simultaneous analysis of step and frequency responses combined with trial and error procedure, the best third-order transfer function is obtained.

Figure 8 shows the variations of the rotor position in response to a step input voltage of 50 V in order to sweep the entire range of shaft deflection.

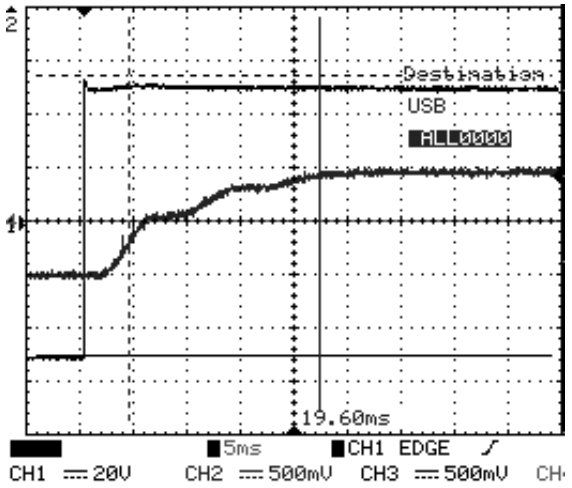

Figure 8
Variation of shaft deflection to a step input voltage of 50 V peak

Figures 9 and 10 show the measured characteristics of frequency and normalized step responses in comparison to the response of the estimated transfer function.

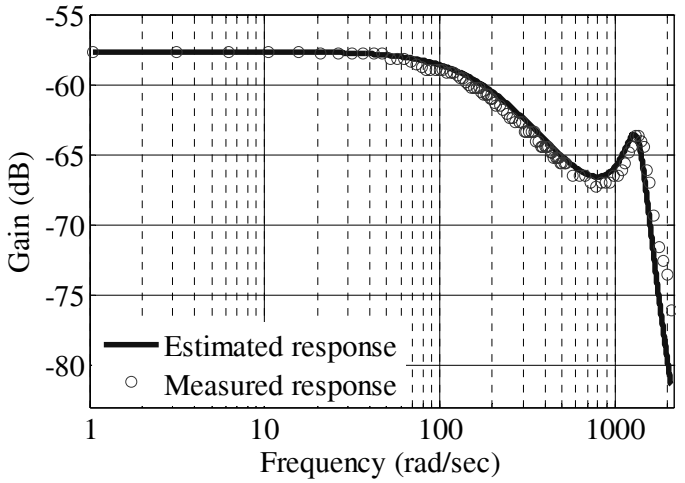

Figure 9
Measured and estimated frequency response chracteristics with input 40 V peak

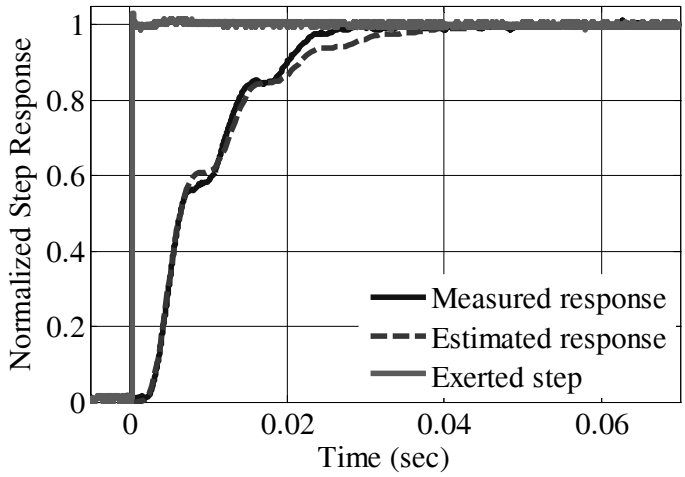

Figure 10
Normalized Measured and estimated step response chracteristics with input 40 V peak

Taking into account the response delay, the estimated transfer function is obtained as follows:

$$G(s)=\frac{\theta(s)}{V(s)}=\frac{241560.e^{-0.0011S}}{(S+120)\left(S^2+3356.5S+1537600\right)}$$

$$=\frac{241560.e^{-0.0011S}}{\left(S^3+492S^2+1582240S+184512000\right)} \qquad (12)$$

Assume that K_s, J and R are predetermined parameters. The remaining parameters, which are difficult to determine experimentally, are obtained by the comparison of the estimated transfer function of eqn. 12 with the parametric one from eqn. 9, and by solving the four linear equations. The estimated values of these parameters are shown in Table 2.

Table 2
Estimated values of the parameters by classical identification

$K_t\left(Nm/A\right)$	5.23
$K_b\left(V.s/rad\right)$	0.08
$L(H)$	29.9
$K_f\left(Nm.s/rad\right)$	2.7×10^{-4}

As is shown in Figure 11, the discrepancy between frequency responses of the system modeled by the estimated parameters and the measured parameters is adequately acceptable.

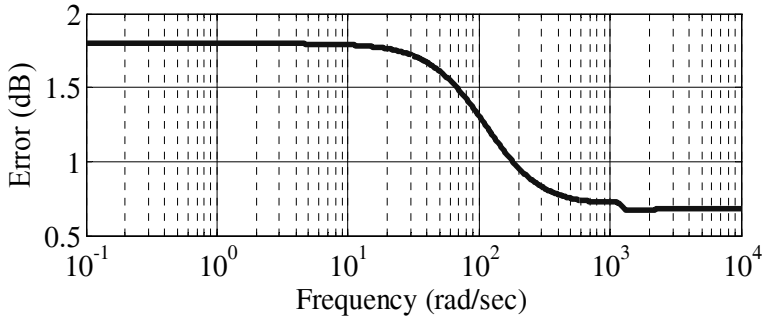

Figure 11

The error between the frequency responses of the system modeled by estimated and measured parameters

Conclusions

From a series of linear mathematical equations, a parametric third-order transfer function was achieved in order to model a pneumatic servo valve as a linear time-invariant SISO system. The static and dynamic performance characteristics of the torque motor were obtained by a test system. The results showed a remarkably good linear trend, which made it suitable for servo applications. Based on classical methods of identification, including frequency and step responses, an acceptable estimated model was fitted to the measured results. Finally, with the comparison of estimated and parametric third-order transfer functions, the design parameters of the servo-valve were obtained. The results were very close to the design specifications of the manufactured servo-valve, which validated the gray-box modeling.

References

[1] Igor L. Krivts, G. V. Krejnin: ’Pneumatic Actuating Systems for Automatic Equipment Structure and Design’ CRC Press, 2006

[2] S. Li, Y. Song: ’Dynamic Response of a Hydraulic Servo-Valve Torque Motor with Magnetic Fluids’, Mechatronics, Vol. 17, pp. 442-447, 2007

[3] Songjing Lia, W. Bao, "Influence of Magnetic Fluids on the Dynamic Characteristics of a Hydraulic Servo-Valve Torque Motor," Mechanical Systems and Signal Processing, Vol. 22, pp. 1008-1015, 2008

[4] I. R. Smith, J. G. Kettleborough, Y. Zhang: ’Simplified Modelling and Dynamic Analysis of a Laws' Relay Actuator’, Mechatronics, Vol. 9, pp. 463-475, 1999

[5] Y. Zhang, I. R. Smith, J. G. Kettleborough: 'Performance Evaluation for a Limited-Angle Torque Motor', IEEE/ASME Transactions on Mechatronics, Vol. 4, pp. 335-339, September 1999

[6] H. R. Bolton, Y. Shakweh: 'Performance Prediction of Laws' Relay Actuator', in IEE Conference on Electric Power Application, Vol. 137, Issue 1, 1990, pp. 1-13

[7] S. A. Evans, I. R. Smith, J. G. Kettleborough: 'Static and Dynamic Analysis of a Permanent Magnet Rectilinear Laws' Relay Actuator', in IEE Conference on Electric Power Application, Vol. 146, Issue 1, 1999, pp. 11-16

[8] S. A. Evans, I. R. Smith, J. G. Kettleborough: 'Permanent-Magnet Linear Actuator for Static and Reciprocating Short-Stroke Electromechanical Systems', IEEE/ASME Transactions on Mechatronics, Vol. 6, pp. 36-42, March 2001

[9] Ching Chih Tsai, Shui-Chun Lin, Hsu-Chih Huang, Yu-Ming Cheng: 'Design and Control of a Brushless DC Limited-Angle Torque Motor with its Application to Fuel Control of Small-Scale Gas Turbine Engines', Mechatronics, Vol. 19, Issue 1, 2009, pp. 29-41

[10] Ngoc Dung Vuong, Marcelo H. Ang Jr: 'Dynamic Model Identification for Industrial Robots', Acta Polytechnica Hungarica, Journal of Applied Sciences, Hungary, Vol. 6, Issue 5, pp. 51-68, 2009

[11] J. P. Norton: 'An Introduction to Identification' Academic Press Inc., 1986

Laboratory Investigation on the Saturation and Initial Structure Effects on the Undrained Behavior of Granular Soil Under Static Loading

Noureddine Della, Ahmed Arab

Laboratory of Material Sciences and Environment
Civil Engineering Department, University of Chlef
Sendjas Street, PO Box 151, Chlef 02000, Algeria
E-mail address: nour_della@yahoo.fr

Abstract: The effects of the initial state of the samples and the saturation evaluated in terms of Skempton's pore pressure B on the behavior of Chlef sand were studied in this article. For this purpose, the results of two series of undrained monotonic compression tests on medium dense sand (RD= 50%) are presented. In the first test series, the influence of the specimens' fabric and confining pressure is studied. Triaxial specimens containing Chlef sand with 0.5% non plastic silt content were isotropically consolidated to 50 kPa, 100 kPa and 200 kPa. The specimens were formed using both dry funnel pluviation and wet deposition. The results indicate that the confining pressure and the method of sample preparation have a significant influence on the liquefaction resistance of the sand. In the second series of tests, the saturation influence on the resistance to the sand liquefaction is realized on samples at an effective stress of 100 kPa for Skempton's pore pressure coefficient varying between 32% and 90%. It was found that an increase in the Skempton' S pore pressure coefficient B reduces the soil dilatancy and amplifies the phase of contractancy.

Keywords: liquefaction; sand; dry funnel pluviation; wet deposition; confining pressure; pore pressure; compression; undrained; saturation

1 Introduction

The region of Chlef, situated in the North of Algeria about 200 km to the west of the capital Algiers, due to its proximity to the continental European and African plates, as is shown in Fig. 1, is constantly a very instable zone, subjected to intense seismic activity. Over the last centuries, it underwent destructive earthquakes (ex Orléansville, ex El-Asnam) in 1922, 1934, and 1954. This last earthquake, of magnitude 6.7, and which has been described well by Rothé [26], Thevenin [29] and Mckenzie [18], caused the deaths of 1340 people and significant damage to different civil engineering structures, as well as causing and the appearance of soils sliding and the liquefaction phenomenon.

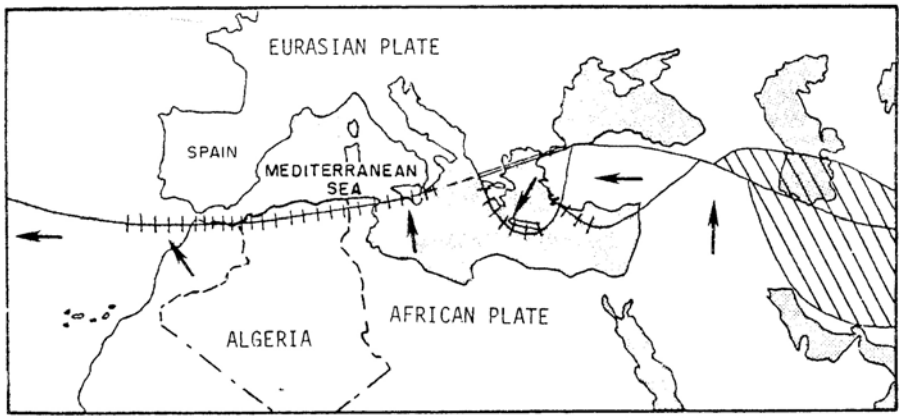

Figure 1
Movement of Europe-Afrique plate

On October 10, 1980 at 13h25 (local time), the region was the theater of a strong earthquake of a magnitude of 7.3 according to Papastamatiou's calculations [23], followed by two significant jolts of magnitudes 6 and 6.1 within an interval of several hours and by numerous shocks over the following months [22]. The main shock generated an significant inverse fault of about 40 km long in the surface [1]. The epicenter of this earthquake was located in the North East of El-Asnam around the village of Beni Rached.

The disaster of October 10, 1980 caused the loss of numerous lives (about 3000 deaths) and caused the destruction of a great number of buildings, and damage to the connecting infrastructures and to public equipment. If we put aside the merely tectonic demonstrations, as the spectacular fault appeared near El-Asnam. The seismic vibration also generated a number of geodynamic phenomena within the surface of the soil: movements of the ground of varied nature and size, and especially the liquefaction of the sandy soils following a loss of resistance to shearing.

According to Durville and Méneroud [8], the phenomenon of liquefaction appeared at a vast alluvial valley crossed by the Chlef river and at the zone of confluence of this river with the Fodda river, as is shown in Fig. 2.

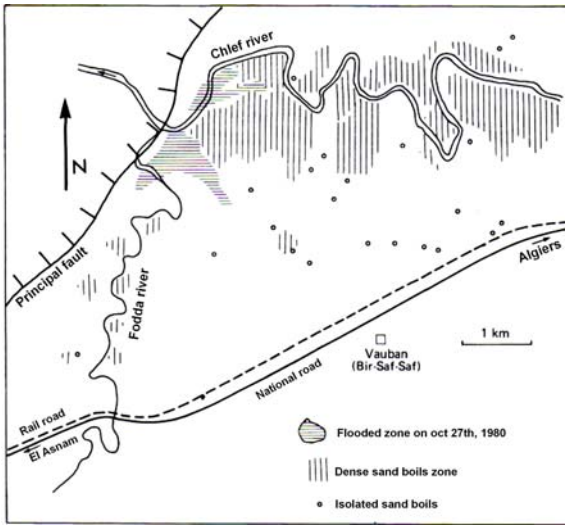

Figure 2
Valley of the Chlef river and location of the sand boils due to the liquefaction phenomenon

2 Literature Review

During earthquakes, the shaking of the ground may cause saturated cohesionless soils to lose their strength and behave like a liquid. This phenomenon is called soil liquefaction and will cause the settlement or tipping of buildings, as well as failures of earth dams, earth structures and slopes. The modern study of soil liquefaction was triggered by the numerous liquefaction-induced failures during the 1964 Niigata, Japan earthquake.

Numerous studies have reported that the behavior of sands can be greatly influenced by the initial state and the saturation of the soil. Polito and Martin [25] asserted that the relative density and the skeleton void ratio were factors that seemed to explain the variation in different experimental results. Yamamuro and Lade [33], [34] and Yamamuro and Covert [32] concluded that complete static liquefaction (zero effective confining pressure and zero effective stress difference) in laboratory testing is most easily achieved in silty sands at very low pressures. Kramer and Seed [13] also observed that liquefaction resistance increased with increased confining pressure.

Several specimen reconstitution techniques, tamping and pluviation being the most common, are in use in current practice. The objective in all of these cases is to replicate a uniform sand specimen at the desired void ratio and effective stresses in order to simulate the sand mass in-situ. However, the effect of the preparation method of the samples has been subject of conflicting research. Many studies have

reported that the resistance to the liquefaction is more elevated for samples prepared by the method of sedimentation than for samples prepared by dry funnel pluviation and wet deposition [41]; other studies have found that the specimens prepared by the dry funnel pluviation method tend to be less resistant than those reconstituted by the wet deposition method [19], [35]. Other researchers indicated that the tests prepared by dry funnel pluviation are more stable and dilatant than those prepared by wet deposition [3], [6]. Vaid et al. [30] confirm this result while showing that wet deposition encourages the initiation of liquefaction in relation to preparation by pluviation under water. Yamamuro et al. [36] concluded after their laboratory investigation that the method of dry pluviation supports the instability of the samples, contrary to the method of sedimentation. Wood et al. [31] found that the effect of the method of deposition on the undrained behavior decreases when the density increases. They also found that this influence decreases with an increase in the fines content, particularly with lower densities. The focus of this study is to identify the differences in undrained triaxial compression behavior that can result from using different reconstitution techniques to create silty sand specimens.

Additionally, in the neighborhoods of the town of Chlef (Algeria), unsaturated zones exist on top of phreatic ground, which underwent a significant folding back following the dry conditions which have affected the area since the 1980s. Over the past decades, advanced research has helped us better understand the liquefaction of the grounds based on experiments carried out in laboratory, on physical modeling and on numerical analysis. The majority of these investigations of the liquefaction of granular soils were based on completely saturated material. The study of the influence of the degree of saturation on the liquefaction of soils is of practical interest, because we often find structures built on top of phreatic ground; which implies the presence of partially saturated grounds. The incidence of partial saturation on cyclic resistance was approached theoretically by Martin et al. [16]. Mulilis et al. [20] examined the effect of the saturation degree on the liquefaction of Monterrey sand. They noted that a variation of Skempton's coefficient B between 0.91 and 0.97 does not significantly affect the liquefaction of this sand. This influence depends on the type of soil, the density and the initial confining pressure. However, recent results of in-situ tests include the measurements of the velocity of the compression waves (Vp) and indicate that the condition of partial saturation can exist above the level of the phreatic ground for a few meters due to the presence of bubbles of air [11], [21] or the presence of gas bubbles in the marine sediments and sands containing oils, as noted by Mathirobanand Grozic [17]. The effects of a condition of partial saturation on liquefaction were approached by several researchers [2], [17], [24],[38]. The condition of the saturation of soil samples in laboratory can be evaluated by measuring the value of Skempton's pore pressure (B) coefficient, as suggested by Ishihara et al. [11]. The results of laboratory tests showed that resistance to the liquefaction of sands increases when the saturation degree decreases [16], [40], [11], [12], [37],[39], [5].

Mullilis et al. [20] and Tatsuoka et al. [28] showed that in the case of loose sands, a good saturation requires high values of the coefficient B .On the other hand, for stiffer materials, the problem seems less critical. Sheriff et al. [27] showed that a fine or clayey sand can be considered saturated if the value of B exceeds 0.8. Chaney [7] more precisely noted that the coefficient B must exceed 0.96 so that the soil is well saturated. Giroud and Cordary [9] noted that for values of B superior to 0.85, the degree of saturation is very close to 1. Tests of liquefaction were carried out by Yoshimi et al. [40] on medium dense Toyoura sand with various degrees of saturation. The results show that the degree of saturation significantly affects the resistance to liquefaction: With a coefficient B higher than 0.8, it is enough to apply three cycles to achieve liquefaction of the sample; whereas we need eight cycles to obtain liquefaction of specimens having a coefficient B close to 0.5.

This literature survey reveals a real need for experimental data concerning the behavior of unsaturated soils under undrained monotonic loading. Such data improves our understanding of the influence of the saturation degree on the response of soils to undrained monotonic loading. This paper includes a contribution to existing experimental data. It presents results of undrained monotonic triaxial tests performed on Chlef sand for various values of Skempton's pore-pressure coefficient.

3 Laboratory Testing

3.1 Tested Material and Procedures

The current laboratory investigation was carried out in order to study the influence of initial state and saturation on the undrained behavior of silty sand. For this purpose, a series of tests of undrained triaxial compression under monotonic loading conditions were performed on reconstituted samples of natural Chlef sand containing 0.5% of non plastic (PI= 5.81%) silt of the Chlef River. The samples were prepared at the same relative density of undisturbed ones to represent a medium dense state (RD= 50%) using two different techniques: dry funnel pluviation and wet deposition (a detailed summary of the procedure for each method is provided in the following section) and consolidated isotropically at an initial confining pressure of 50 kPa, 100 kPa and 200 kPa. Sand samples were collected from a liquefied layer of the deposit area close to the epicentre of the Chlef earthquake (October 10, 1980). Fig. 3 shows the craters of liquefied ground on the banks of the Chlef River. Fig. 4 illustrates the typical subsidence locations of the liquefied soil. The index properties of the soil used in the study are summarized in Table 1. The grain size distribution curve for the tested material is shown in Fig. 5.

Figure 3
Sand boils due to the liquefaction phenomenon in the Chlef region

Figure 4
Subsidence of the Chlef River banks due to liquefaction

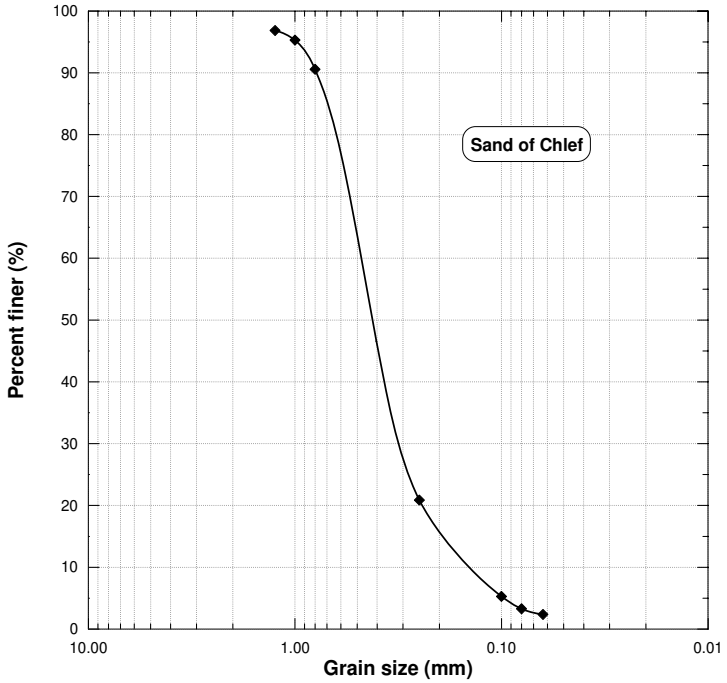

Figure 5
Grain size distribution of the tested soil

Table 1
Index properties of sand

Material	e_{min}	e_{max}	γ_{dmin} g/cm^3	γ_{dmax} g/cm^3	γ_s g/cm^3	Cu D_{60}/D_{10}	D_{50} mm	D_{10} mm	Grains shape
O/Chlef	0.54	0.99	1.34	1.73	2.67	3.2	0.45	0.15	Rounded

The samples were 70 mm in diameter and 140 mm in height with smooth lubricated end-plates. After the specimen was been formed, the specimen cap was placed and sealed with O-rings, and a partial vacuum of 20 kPa was applied to the specimen to reduce the disturbances. In the Saturation phase, the technique of Lade and Duncan [14] was used by purging the specimen with carbon dioxide for approximately 30 min. De-aired water was then introduced into the specimen from the bottom drain line. The degree of saturation was controlled during a triaxial compression test by Skempton's coefficient, which can be related to the degree of saturation by the following relation (Lade and Hermandez [15]):

$$B = \frac{1}{1 + nk_s\left(\frac{S_r}{k_w} + \frac{(1 - S_r)}{U_a}\right)} \quad (1)$$

where Ks and kw indicate the bulk modulus of the soil skeleton and the water, respectively; n=the soil porosity, u_a= water pore pressure.

All test specimens were isotropically consolidated at a mean effective pressure of 50 kPa, 100 kPa and 200 kPa, and then subjected to undrained monotonic triaxial loading.

3.2 Depositional Techniques

Wet deposition and Dry funnel pluviation were used to reconstitute the specimens. The first method consists of mixing with the highest possible homogeneous manner, the sand previously having been dried, with a small quantity of water fixed at 3%, and the deposition of the humid soil in the mold with control of the content in water. The soil was placed finely by successive layers. A constant number of strokes was applied to get a homogeneous and isotropic structure. In the dry funnel pluviation method, the dry soil was deposited in the mold with the help of a funnel with the height controlled. This method consists of filling the mold by tipping in a rain of the dry sand.

3.3 Equipment

An advanced automated triaxial testing apparatus was used to conduct the monotonic tests (see Fig. 6).

Figure 6
The experimental device used

4 Experimental Results

4.1 Effect of Confining Pressure

The effect of varying the effective confining pressure on the liquefaction resistance of sand is shown in Figs. 7 and 8. As the confining pressures increased, the liquefaction resistance of the sands increased for both the dry funnel pluviation and the wet deposition methods. The results in Figs. 7a and 7b with an initial density of 50% (medium dense state) for specimens reconstituted by the first method at a confining pressure of 50 kPa show a weaker resistance than those shown at a confining pressure of 100 kPa and 200 kPa. Its resistance increases at the beginning of the loading up to a value of 25 kPa, corresponding to an axial strain of 0.5%, then it decreases up to an axial distortion strain of 5% to stabilize passing nearly a quasi steady state (QSS); then the sample mobilizes a residual strength increasing the resistance of the sample in the steady state. The stress path diagram (Fig. 7b) presents a reduction of the effective mean stress until a value of 10 kPa, then a migration towards higher values, characterizing a dilating state. The same trends are signaled for the samples at confining pressures of 100 and 200 kPa, with peak deviatoric stresses of 48 kPa and 90 kPa respectively.

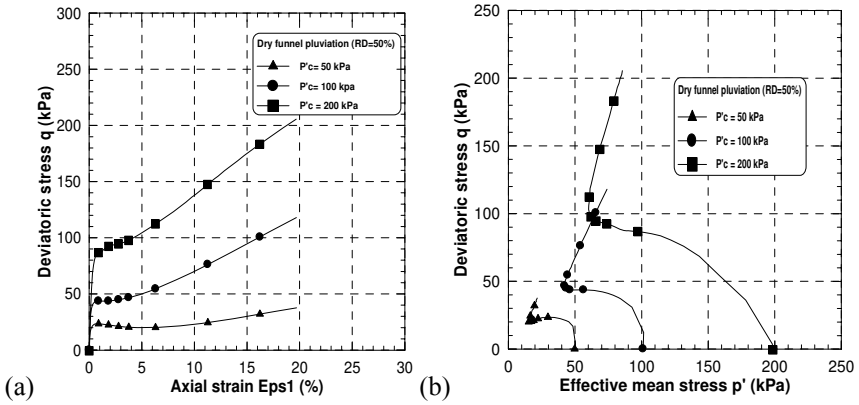

Figure 7
Undrained tests for samples prepared by the dry funnel pluviation method:
(a) deviatoric stress-strain curve, (b) stress path

Effective stress paths for undrained triaxial compression tests on Chlef sand for samples prepared by the wet deposition method with initial relative densities of 50% are plotted on the p'-q diagrams shown in Fig. 8b. As can be seen, complete static liquefaction occurred in the test with the lowest confining pressure (50 kPa). Static liquefaction was coincidental with the formation of large wrinkles in the membranes surrounding the specimens.

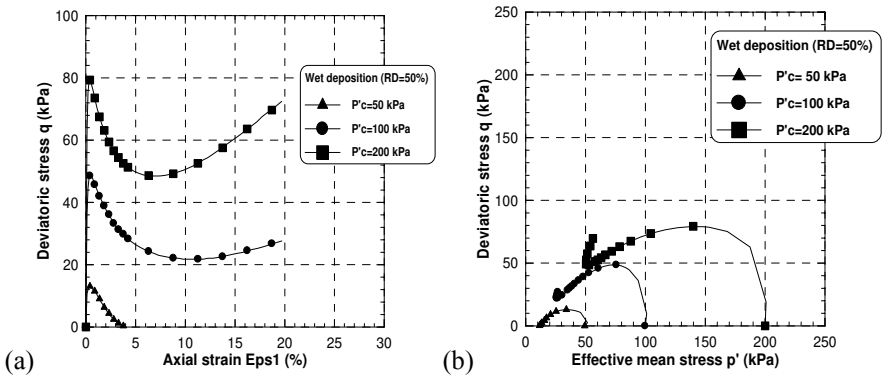

Figure 8
Undrained tests for samples prepared by the wet deposition method:
(a) deviatoric stress-strain curve, (b) stress path

Fig. 8b also shows that when the initial confining pressure is increased beyond 50 kPa, the effective stress paths exhibit behavior that is characterize by increasing stability or increasing resistance to liquefaction. This is demonstrated by examining the stress-strain curves in Fig. 8a. The initial confining pressures and densities are shown for each test. The stress-strain curves of the 100 and 200 kPa initial confining pressure tests show that the stress difference does not reach zero as in the test indicating complete liquefaction, but decreases to a minimum before increasing to levels well above the initial peak, or, with progressive stabilization, around an ultimate stationary value very weak. This is the condition of temporary liquefaction. The effect of increasing the confining pressure is to increase the dilatant tendancies in the soil.

4.2 Influence of Sample Reconstitution Method

The effect of the specimens' reconstitution method on maximal deviatoric stress is shown in Fig. 9a. It can be noticed from the results of these figures that the dry funnel pluviation method (DFP) gives more significant values of the maximal deviator, and therefore a much higher resistance to liquefaction, in contrast with the wet deposition method (WD), where some weaker values of the maximal deviator were noted, with progressive stabilization around a very weak or nil ultimate stationary value, meaning the liquefaction of the sample.

The same tendencies are noted for the variations of the values in the peak deviatoric stress given in Fig. 9b. As can be seen, the samples formed by the dry funnel pluviation method exhibit a resistance to monotonic shearing, superior to those made by the wet deposition method.

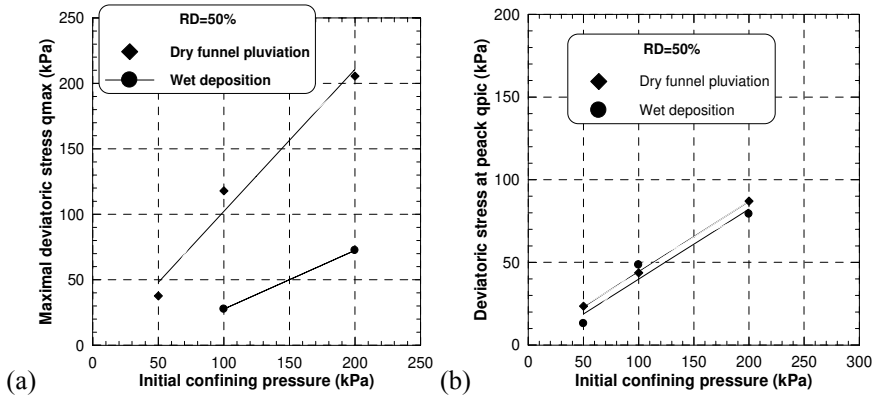

Figure 9

Effect of the depositional method on the maximal deviatoric stress (a) and the peak deviatoric stress (b)

The influence of the sample preparation methods on excess pore pressure is illustrated in Fig. 10. As shown in Fig. 10a, for the dry funnel pluviation method, the variation of the pore pressure curves presents two phases: the first shows a very high initial rate of generation, giving account of the strongly contracting character of the Chlef sand. In the second phase, this rate decreases progressively with the axial strain, reflecting the dilating character of the material. The developed excess pore pressure in the samples prepared by the wet deposition method is presented in Fig. 10b. It can be seen that the samples exhibit a very high contracting character, with an expansion rate highly elevated from the beginning of the shearing and progressive stabilization toward an ultimate value, associated to the stabilization of the deviatoric stress.

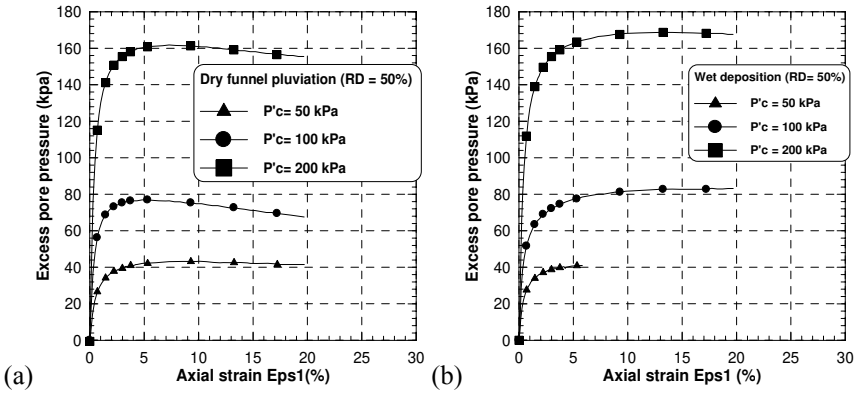

Figure 10

Effect of sample reconstitution methods on excess pore pressure: (a) Dry funnel pluviation method, (b) Wet deposition method

The results of Figs. 9 and 10 are in perfect agreement with those of the Figs. 7 and 8, showing that the method of dry funnel pluviation encourages the increase of resistance to the monotonic shearing of the samples, in contrast to the wet deposition method, which accelerates the instability of the samples, which show a very weak resistance, and even provokes the phenomenon of liquefaction of the sand for the weak confinements, leading to the collapse of the sample.

4.3 Effect of the Saturation Degree

Fig. 11 shows the results of the undrained triaxial compression tests performed in this study for various values of coefficient of Skempton (B) between 32% and 90% with an initial confining pressure of 100 kPa. As can be seen, increases in the degree of saturation characterized by the coefficient of Skempton (B) lead to a reduction in the resistance of deviatoric stress (Fig. 11a) and an increase in water pressure (Fig. 11b). The increase in the water pressure results from the role of the degree of saturation in the increase in the phase of contractance observed during the drained tests. The increase in the pore water pressure leads to a reduction in the effective confining pressure and consequently with a reduction of resistance as Fig. 10a illustrates. The stress path curve in the plan (p', q) shows well the role the degree of saturation plays in the reduction of the effective mean stress and the maximal deviatoric stress (Fig. 11c).

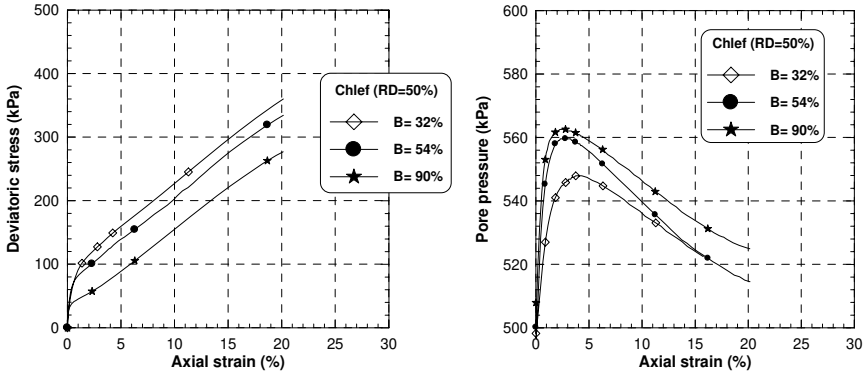

(a) (b)

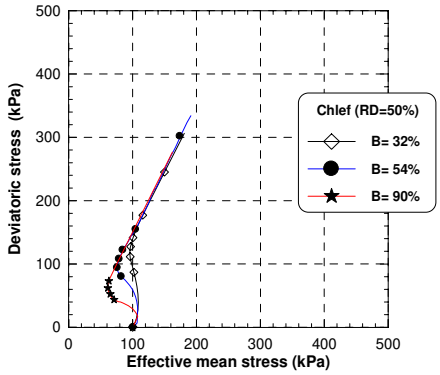

(c)

Figure 11

Influence of the coefficient of Skempton (B) on undrained behavior of Chlef sand

(a) Deviatoric stress, (b) excess pore ressure, (c) stress path

Fig. 12 shows the evolution of the maximal deviatoric stress versus the coefficient of Skempton (B). We note that the resistance to monotonous shear decreases in a linear manner with the increase of the coefficient of Skempton (B); the maximal deviator passes from a value of q=360 kPa for B= 32% to a value q=276.73 kPa for B=90%. Fig. 13 shows the evolution of the pore water pressure to the peak versus the the coefficient of Skempton (B). We note that the pore water pressure to the peak increases with the increase in the coefficient of Skempton (B); the pore water pressure to the peak passes from 547.90 kPa for B=32% to a value of 562.53 kPa for B= 90%.

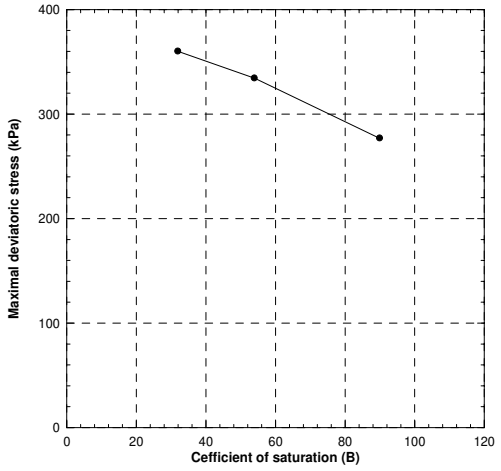

Figure 12

Evolution of maximal deviatoric stress versus Skempton's coefficient (B)

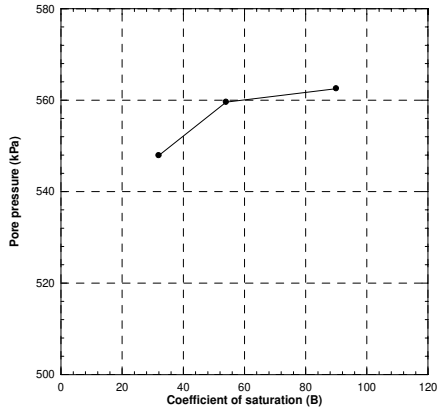

Figure 13
Evolution of peak pore pressure versus Skempton's coefficient (B)

4.4 Variation of the Residual Strength

When sands are subjected to an undrained shearing, following the peak of deviatoric stress, the resistance to the shearing falls with an almost constant value on a broad deformation. Conventionally, this resistance to shearing is called residual strength, or the shearing force at the quasi steady state (Qss). The residual strength is defined by Ishihara [10] as:

$$S_{us} = (q_s/2)\cos\phi_s \quad (2)$$

where qs and ϕ_s indicate the deviatoric stress and the mobilized angle of interparticle friction at the quasi steady state.

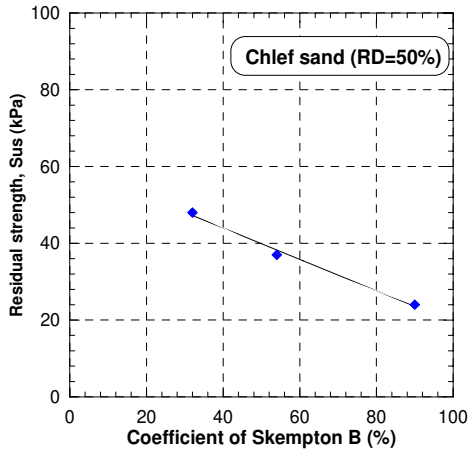

Figure 14
Influence of the coefficient of Skempton (B) on the Residual strength at the quasi steady state

Fig. 14 shows the evolution of the residual strength with Skempton's coefficient (B).We note that the residual strength decreases in a significant and linear way with the increase in Skempton's coefficient (B) resulting from the role of saturation as for the amplification of the contractance of the studied soil.

Conclusion

A comprehensive experimental program to study the effects of initial state and saturation on the undrained monotonic behavior of sandy soil was undertaken, in which two series of tests were performed. All the tests were carried out on medium dense specimens. Based on the results from this investigation, the major conclusions are as follows:

1 Complete static liquefaction occurred at low confining pressure (50 kPa) for the wet deposition method.

2 As the confining pressure increased, the liquefaction resistance of the sand increased. This observation correlates with most historic cases of apparent static and earthquake-induced liquefaction. The results reveal as well that the method of reconstitution has a detectable effect on the undrained behavior. The dry funnel pluviation method appeared to indicate a more volumetrically dilatant or stable response, while the wet deposition method appeared to exhibit a more contractive or unstable behavior.

3 The saturation has a detectable effect on the undrained behavior. The results showed that an increase in the Skempton's pore pressure coefficient (B) induces a reduction in the initial stiffness and the resistance of the soil (maximal deviatoric stress); and increases the phase of contractance. This, results in a significant effect on the volumetric response inducing an amplification of the phase of contractance when the coefficient of Skempton B increases.

4 The residual effort (Sus) decreases in a significant and linear way with the increase in the Skempton's pore pressure coefficient (B) resulting from the role of saturation as for the amplification of the contractance.

References

[1] Ambraseys, N. N. The El-Asnam Earthquake of 10 October 1980: conclusions drawn from a field study. Q. J. Eng. Geol., London 14, 1981, pp. 143-148

[2] Atigh, E., Byrne, P. M.: Liquefaction Flow of Submarine Slopes under Partially Undrained Conditions: an Effective Stress Approach. Can. Geotechnical J., 41, 2004, pp. 154-165

[3] Benahmed, N., Canou, J., Dupla, J. C.: Structure initiale et propriétés de liquéfaction statique d'un sable, Comptes Rendus Mécanique 332, 2004, pp. 887-894

[4] Bishop, A. W., Wesley, L. D.: A Hydraulic Triaxial Apparatus for Controlled Stress Path Testing, Geotechnique, 4, 1975, pp. 657-670

[5] Bouferra, R., Benseddiq, N., Shahrour, I.: Saturation and Preloading Effects on the Cyclic Behaviour of Sand, International Journal of Geomechanics, ASCE, 2007, pp. 396-401

[6] Canou, J.: Contribution l'étude et à l'évaluation des propriétés de liquéfaction d'un sable, Thèse de Doctorat de l'Ecole Nationale Des Ponts et Chaussées, Paris, 1989

[7] Chaney, R. C.: Saturation Effects on the Cyclic Strength of Sand, Proc., Earthquake Engineering and Soil Dynamics, Vol. 1, ASCE, New York, 1978, pp. 342-359

[8] Durville, J. L., Méneroud, J. P.: Phénomènes géomorphologiques induits par le séisme d'El-Asnam, Algérie: *Bull. Liaison Labo. P. et Ch*., No. 120, juillet-août 1982, pp. 13-23

[9] Giroud, J. P., Cordary, D.: Prevision du tassement initial et du tassement différé des fondations superficielles, Annales de l'Institut Technique du Bâtiment et des Travaux Publics, 135, SP 127, Janvier, 1976, pp. 105-135

[10] Ishihara, K.: Liquefaction and Flow Failure during Earthquakes, Geotechnique, Vol. 43, N°3, 1993, pp. 351-415

[11] Ishihara, K., Tsuchiya, H., Huang, Y. and Kamada, K.: Recent Studies on Liquefaction Resistance of Sand Effect of Saturation. Proc. 4th Conf. Recent Advances in Geotech. Earth. Engg., Keynote Lecture, 2001

[12] Ishihara, K., Tsukamoto, Y., Kamada, K.: Undrained Behavior of Near-saturated Sand in Cyclic and Monotonic Loading, Proc. Conf., Cyclic Behavior of Soils and Liquefaction Phenomena, 2004, pp. 27-39

[13] Kramer, S. L. and Seed, H. B.: Initiation of Soil Liquefaction under Static Loading Conditions, J. Geotech. Eng. 114, No. 4, 1988, pp. 412-430

[14] Lade, P. V., Duncan, J. M.: Cubical Triaxial Tests on Cohesionless Soil, Journal Soil Mechanics and Foundations Division ASCE 99, No. SM10, 1973, pp. 793-812

[15] Lade P. V., Hermandez, S. B.: Membrane Penetration Effects in Undrained Tests, Journal of Geotechnical Engineering Division, ASCE, GT2, 1977, pp. 109-125

[16] Martin, G. R., Finn, W. D. L., Seed, H. D.: Effects of System Compliance on Liquefaction Tests, Journal of Geotechnical Engineering Division, ASCE, GT4, 1978

[17] Mathiroban, S., Grozic, J., 2004. A Model to Predict the Undrained Behaviour of Loose Gassy Sand. Proceeding 57th Geotech. Conf., Session 6G, 16-22

[18] McKenzie, D.: Active Tectonics of the Mediterranean Region, Geophysical Journal of the Royal Astronomical Society, 1972

[19] Mulilis, J. P., Seed, H. B., Chan, C. K., Mitchell, J. K., Arulanadan, K.: Effects of Sample Preparation on Sand Liquefaction, *Journal of Geotechnical Engineering Division, ASCE* 103, GT2, 1977, pp. 91-108

[20] Mulilis, J. P., Townsend, F. C., Horz, R. C.: Triaxial Testing Techniques and Sand Liquefaction, ASTM STP 654, Dynamic Geotechnical Testing, 1978, pp. 265-279

[21] Nakazawa, H., Ishihara, K., Tsukamoto, Y., Kamata, T.: Case Studies on Evaluation of Liquefaction Resistance of Imperfectly Saturated Soil Deposits, Proc., Conf., Cyclic Behavior of Soils and Liquefaction Phenomena, Germany, 2004

[22] Ouyed, M.: Le tremblement de terre d'El-Asnam du 10 octobre 1980: étude des répliques, Thèse de 3ème Cycle, Université de Grenoble, 1981

[23] Papastamatiou, D.: El-Asnam, Algéria Earthquake of October 10, 1980: Field Evidence of Ground Motion in the Epicentral Region, Geognosis Ltd., London, 1980

[24] Pietruszczak, S., Pande, G., Oulapour, M. A.: Hypothesis for Mitigation of Risk of Liquefaction, Geotechnique, 9, 2003, pp. 833-838

[25] Polito, C. P., Martin II J. R.: A Reconciliation of the Effects of Non-Plastic Fines on the Liquefaction Resistance of Sands Reported in the Literature. *Earthquake Spectra* 19, No. 3, 2003, pp. 635-651

[26] Rothé, J. P.: Le tremblement de terre d'Orléanville et la séismicité de l'Algérie, La nature, 3237, Paris, 1955, pp. 1-9

[27] Sherif A. M., Tsuchiya, C., Isibashi, I.: Saturation Effects on Initial Soil Liquefaction, Journal of Geotechnical Engineering Division, Vol. 103, n° 8, 1977, pp. 914-917

[28] Tatsuoka, F., Molenkamp, F., Torii, T., Hino, T.: Behavior of Lubrication Layers of Platens in Element Tests. Soils and Foundations, 1, 1984, pp. 113-128

[29] Thevenin, J.: Les effets du seisme de septembre 1954 sur les ouvrages hydrauliques de la region d'Orléanville, Revue Terre et Eaux, N° 24, 1st Trimestre, Paris, 1955

[30] Vaid, Y. P., Sivathayalan, S., Stedman, D.: Influence of Specimen Reconstituting Method on the Undrained Response of Sand, Geotechnical Testing Journal 22, No. 3, 1999, pp. 187-195

[31] Wood, F. M., Yamamuro, J. A., Lade, P. V.: Effect of Depositional Method on the Undrained Response of Silty Sand. Canadian Geotechnical Journal 45, No. 11, 2008, pp. 1525-1537

[32] Yamamuro, J. A., Covert, K. M.: Monotonic and Cyclic Liquefaction of Very Loose Sands with High Silt Content, J. Geotech. Geoenvironmental Engineering ASCE 127, N° 4, 2001, pp. 314-324

[33] Yamamuro, J. A., Lade, P. V.: Static Liquefaction of Very Loose Sands. Canadian Geotechnical J. 34, No. 6, 1997, pp. 905-917

[34] Yamamuro, J. A., Lade, P. V.: Steady State Concepts and Static Liquefaction of Silty Sands, J. Geotech. Geoenv. Eng. ASCE 124, No. 9, 1998, pp. 868-877

[35] Yamamuro, J. A., Wood, F. M.: Effect of Depositional Method on the Undained Behavior and Microstructure of Sand with Silt, Soil Dynamics and Earthquake Engineering, 24, 2004, pp. 751-760

[36] Yamamuro, J. A., Wood, F. M., Lade, P. V.: Effect of Depositional Method on the Microstructure of Silty Sand. Canadian Geotechnical Journal 45, No. 11, 2008, pp. 1538-1555

[37] Yang, J.: Liquefaction Resistance of Sand in Relation to P-Wave Velocity, *Geotechnique,* 4, 2002, pp. 295-298

[38] Yang, J., Sato, T.: Analytical Study of Saturation Effects on Seismic Vertical Amplification of a Soil Layer, Geotechnique, 2, 2001, pp. 161-165

[39] Yang, J., Savidis, S., Roemer, M.: Evaluating Liquefaction Strength of Partially Saturated Sand, Journal of Geotech. and Geoenviron.Engg., ASCE,9, 2004, pp. 975-979

[40] Yoshimi, Y., Tanaka, K., Tokimatsu, K.: Liquefaction Resistance of Partially Saturated Sand Soils and Foundations, 3, 1989, pp. 157-162

[41] Zlatovic, S., Ishihara, K.: Normalized Behavior of Very Loose Non-Plastic Soils: Effects of Fabric, Soils and Foundations 37, No. 4, 1997, pp. 47-56

Optimized Fuzzy Logic for Motion Control

Radhesham Gayakwad

Dept. of PG Studies and Research in Applied Electronics, Gulbarga University, Gulbarga, Karnataka, India, E-mail: radheshamgg@gmail.com

Abstract: For any fuzzy logic application the first and foremost task is to select the optimum number and shape of membership functions such as bell shape, singleton, triangular, etc. for fuzzification; then it is equally essential to select the appropriate defuzzification method, such as COG, COM, MOM, etc. The sampling rate to execute the given command is another important parameter. If these three parameters are optimally selected then the output response of motion controller will have a shorter rise time, less settling time, minimized overshoots/undershoots and negligible steady state error. Hence, the systematic study on selection of number and shape of membership function, selection of defuzzification methods and sampling time for speed control of PMDC micro motor is studied experimentally by applying LabVIEW software. The experimental results reveal that 7 numbers of triangular membership functions, COG defuzzification method and 1 millisecond (msec) sampling rate for labVIEW program execution are the optimum parameters for motion control.

Keywords: fuzzy logic; pmdc motor; labVIEW

1 Introduction

Conventional controllers such as microprocessors or microcontrollers are suitable for parameter measurements such as pressure, temperature, liquid flow, displacement motor speed, etc. Such controllers are reliable only when the measuring parameters are linear and time invariant and when the mathematical model of these parameters are available, because conventional controllers work only on mathematical models of the parameters. If the system is complex and the associated parameters are ill-defined, imprecise, or time variant, then the mathematical models of such complex parameters are difficult to formulate, and hence conventional controllers fail to control such systems effectively. The Fuzzy Logic Controller (FLC) is a controller which can control the said systems and associated parameters because the design and development of FLC is relatively very easy and less time consuming, and it is robust, flexible and adaptive. To control the processing parameters, the designers need not be experts on the system or sub-system. The most important feature of FLC is that the mathematical model of the controlling parameters is not required at all. Moreover, the parameters can

be described by linguistic variables (like warm, fast, medium, etc.) which can be controlled using simple IF-THEN rules.

Li Zhang proposed a fuzzy controller with easier and faster-tuning techniques. He reported a practical computer-aided tuning technique for fuzzy control. He employed triangular membership functions for fuzzification and centre of gravity (COG) for defuzzification. [1-2]. Xie kanglin and Fu Jin Yu reported the determination of membership functions and fuzzy rules of a neural network FLC system. The problem of how to find the most optimal fuzzy rules and input/output membership functions in developing a fuzzy control system and a study of neural networks has been presented in [3]. Castro reported on how many rules are necessary to get a good fuzzy controller. He used triangular membership functions and weighted sum of centroid defuzzification method [4]. An overview of the general class of parameterized defuzzification methods were employed by Filev and Yager [5-6]. Yager and Filev also reported a simple adaptive defuzzification method and a discussion on the issue of defuzzification methods and the selection of fuzzy sets [7-8]. An interesting strategy for dealing with the defuzzification problem based on sensitivity analysis was developed by Mabuchi [9].

The survey of available literature survey shows that so far there is no report of an experimental study of PMDC micro-motor speed characteristics by applying various numbers of triangular membership functions and different types of defuzzification methods and critical aspect of sampling time of FLC and associated with LabVIEW program. Hence we have studied this case.

2 Experimental Set-up

The block diagram for the speed control of PMDC micro motor (Model: 2230 U015S; rating: 15V, 7 mA and 8400 rpm) is shown in Fig. 1.

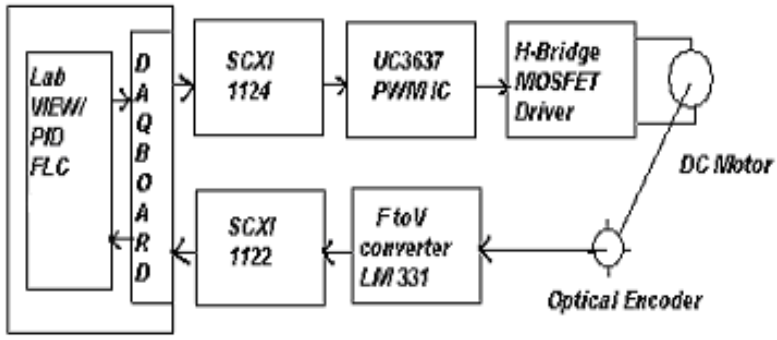

Figure 1
Diagram for speed control of PMDC micro-motor

The PWM signal generated by UC3637 Switched Mode PWM controller chip is fed to the H-bridge MOSFET driver circuit, which in turn drives the motor. The optical encoder attached to the shaft of the motor generates the TTL pulses; these pulses are converted into analog voltage using LM331 F/V converter IC. This analog voltage is fed to the PC through SCXI1122 card. After the execution of the velocity command through LabVIEW*6i,* the analog output voltage is available through DAQ (Data acquisition) board at 1124 card, which is given as input command to the UC3637, where the complete closed loop feedback control is established between the PC and the motor driving circuit.

3 Fuzzy Logic Controller (FLC)

A general FLC consists of four modules; a fuzzification module, a fuzzy rule base, a fuzzy inference engine and a defuzzification module. The interconnections of these modules are shown Figure 2. A fuzzy controller operates by repeating a cycle involving the following steps:

a) Measurements are taken of all variables that represent the relevant conditions of the controlling process.

b) These measurements, which are in crisp form (analog voltage or current), are converted into appropriate fuzzy sets to express measurement uncertainties. This is called fuzzification.

c) These fuzzified measurements are then used by the decision-making logic to evaluate the control rules stored in the fuzzy knowledge base. The result of this evaluation is a fuzzy set, defined by the universe of possible action.

d) This fuzzy set is then converted into a single crisp value (i.e. analog voltage or current), which in some sense is the best representative of the fuzzy set. This conversion is called defuzzification. The defuzzified value represents the final action taken by the fuzzy controller.

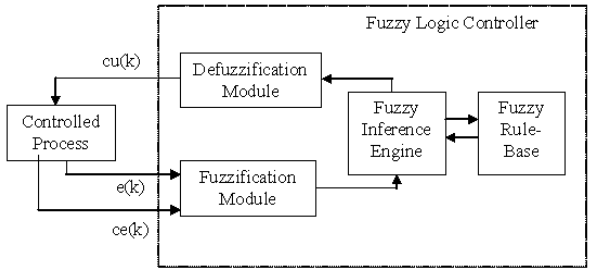

Figure 2
Basic block diagram of fuzzy logic controller

3.1 Membership Functions

Membership functions characterize the fuzziness in a fuzzy set, whether the elements in the set are discrete or continuous in a graphical form for eventual use in the mathematical formalism of fuzzy set theory [10]. The rules used to describe fuzziness graphically are also fuzzy. Since all the information contained in a fuzzy set is described by its membership functions, it is useful to develop a lexicon of terms to describe various special featured functions, such as low temperature, high speed, medium pressure, etc. There are several ways to graphically depict the membership functions that describe fuzziness. The most popular choices of the curves/shapes of the membership functions include: triangular, S, Z, bell-shape and singleton. The important character of these curves/shapes for purpose of use in fuzzy operation is the fact that they overlap. The precise shapes of these curves are not so important in the utility. Rather, it is the number of curves (partitions) used and their overlapping regions that are the most important ideas. Fig. 3 shows the lexicon of terms to describe speed characteristics of PMDC micro-motor for the speed range from 1000 rpm to 3000 rpm.

3.2 Defuzzification

Defuzzification is the conversion of a fuzzy quantity into a precise or crisp (like voltage or current) quantity. In the present work, three types of defuzzification methods are used:

a) Mean of Maxima (MOM) Method

In this method, defuzzification is made of the average of the two selected values.

b) Centre of Maxima COM) method

This method uses the overall output or union of all individual output fuzzy sets.

c) Centre of Gravity (COG) Method

This method uses the algebraic integrated value of the fuzzy sets, and it is most prevalent and physically appealing of all the defuzzification methods. In the present work, the COG defuzzification method is used.

3.3 Sampling Rate

In digital control systems, the sampling rate is the number of times per second a controller reads in sensor data and produces a new output value. The slower the sampling rate, the less responsive the system is, because the controller would always be working with that old data that were present when the last sample was taken. Hence, in the present work we have used three different sampling rates, i.e. 1 sec, 0.1 sec and 1 msec to check the response of speed of a DC motor. These three sampling rates were formulated and studied using LabVIEW software.

4 Description of the VI Diagram

As shown in Fig. 3, the input voltage from F/V through SCXI 1122 is accessed by analog input (Ai) channel. This analog voltage is converted into the corresponding speed using adders and multipliers. First DBL (double precision floating point) represents the set value of 3000 rpm. The error and change in error are found using two subtractors. These two signals are fed to the FLC. The FLC gives the control voltage through analog output (Ao) channel. The motor rpm is then controlled through UC3637 IC and H-Bridge MOSFET driver circuit. The measured speed status is displayed on the waveform chart monitor. All these events are carried out in a feedback loop (labelled as while-loop).

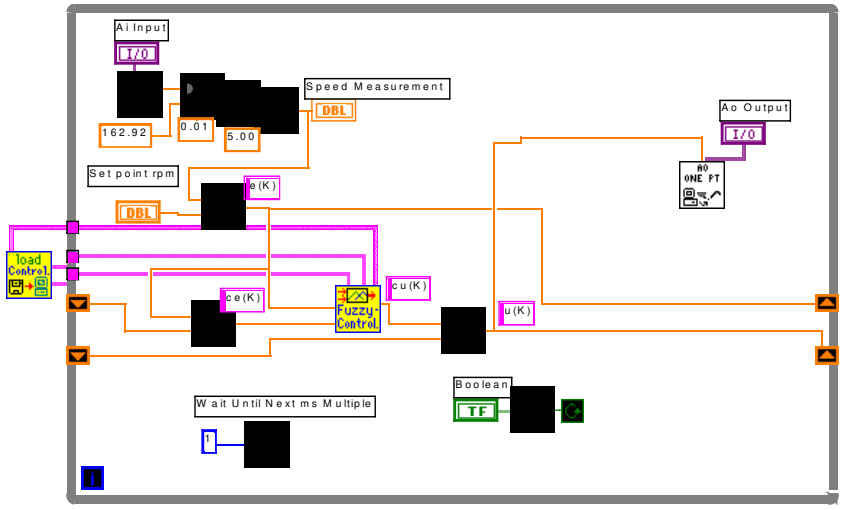

Figure 3
VI Diagram for speed control of PMDC Micro motor

5 Experimental Results

Here the effect of various numbered triangular membership functions, defuzzification methods and different sampling rates related to speed control of PMDC micro-motor are discussed.

5.1 Effect of Membership Functions

The FLC has been successfully implemented for the real time speed control of a PMDC micro-motor at 3000 rpm. First, 3-number triangular membership functions are chosen and the transient response is obtained. Similarly 5 and 7-number triangular membership functions are applied and their transient responses

are observed. The experimental transients of these three functions are shown in Fig. 4. It is observed that for the 3-number triangular membership function, the settling time is 3.5 sec and steady state error is ±40 rpm. For the 5-number triangular membership function, a settling time of 2.7 sec and a steady state error of ±25 rpm oscillations are observed. The response of the 7-number triangular membership function exhibited no overshoots and undershoots and shorter settling time of 1.8 sec was obtained.

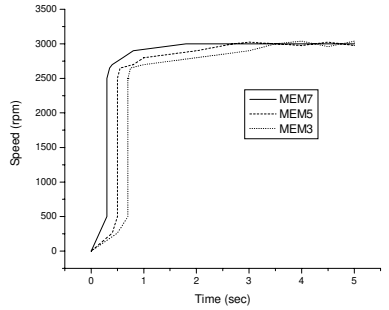

Figure 4

Experimental transient response for 3, 5, and 7-number triangular membership functions [MEM7= 7 number triangular membership functions, etc]

5.2 Effect of Defuzzification Methods

The three defuzzifications, i.e. COM, MOM and COG, are implemented and their effect on the transient response of PMDC micro-motor at 3000 rpm observed. The experimental results (Fig. 5) show that: for the MOM defuzzification method, the settling time is 2.8 sec with overshoots and undershoots of ±25 rpm; the COM defuzzification method has the settling time of 2.5 sec with steady state error of ±10 rpm; and in the case of the COG defuzzification method, the settling time is 2.0 sec without overshoots and undershoots and zero steady state error.

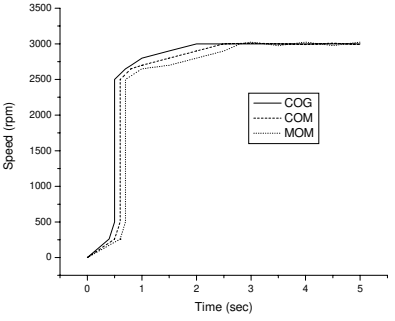

Figure 5

Experimental transient response for defuzzification methods for FLC using three different defuzzification methods

5.3 Effect of Loop-Time Variation

The present system consists of a feedback control system as shown in the VI diagram (Fig. 3). We define the loop-time for this feedback control system as a time for the entire loop. This loop-time is adjustable in the present system with only three possible values, namely 1 msec, 0.1 sec and 1.0 sec. This loop-time is entirely different from the sampling time of the ADC and sample and hold (S/H) circuit in the SCXI 1122 analog input card.

As the SCXI 1122 analog input card works at a sampling rate of 150 kS/s, the sampling period is 1/150, 000 sec (6.7 μsec). This sampling frequency of 150 kS/s is much higher than the frequency of the band limited signal representing the speed of the dc motor (3.3 msec). The sampling frequency is approximately 1000 times the frequency of the band limited signal. The aliasing errors, if any, are taken care of by the anti-aliasing filter in the SCXI 1122 analog input card. The Nyquiste sampling theorem requirement is duly satisfied.

When a 1 msec loop-time is selected, hardly 1000 samples are encountered. The excursions of the speed about the set-point will be very few. Hence the fuzzy logic controller is able to take appropriate decisions and generate corresponding control signals to help the dc motor to run at the set-point speed.

When a loop-time of 0.1 sec and 1.0 sec are chosen, there are approximately 10 Lakhs samples in each loop-time respectively. In such situations, there will be a very large number of excursions about the set-point. Consequently the fuzzy logic controller is utterly confused as to which rule is to be fired in such chaotic conditions. Consquently the fuzzy logic controller takes a long time to control the speed of the dc motor at the desired set-point speed. This is the reason for shortest settling time when we choose 1 msec as the loop-time. The comparison of these three sampling rate is shown in Fig. 6.

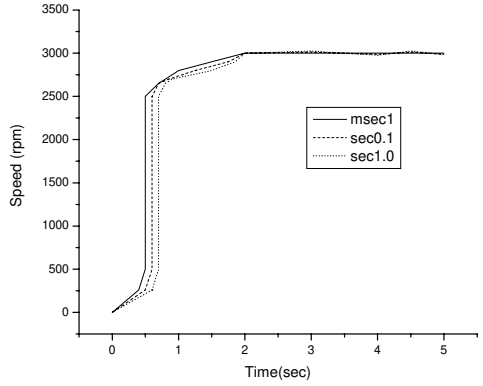

Figure 6

Experimental transient response of speed control for PMDC micro motor using three different sampling rates [m sec1 = 1 m sec sampling time etc]

Conclusions

The FLC has been successfully designed and implemented for the real time speed control of PMDC micro motor for a desired speed of 3000 rpm. The results for the best choices of number of triangular membership functions for fuzzification, defuzzification methods and different sampling rates were obtained. From the experimental transient response, we conclude that for robust, flexible, faster and real time speed control of PMDC micro motor using FLC technique, the best choices are 7-number triangular membership functions for fuzzification, a COG method for defuzzification and a sampling time of 1 msec.

References

[1] Li Zhang., "A Practical Guide to Tune Proportional Integral (PI) Like Fuzzy Controllers", IEEE Int. Conf. on Fuzzy Systems, **2**, 1992, pp. 630-640

[2] Li Zhang., "A Practical Computer-aided Tuning Technique for Fuzzy Control", IEEE Int. Conf Fuzzy Systems **3**, 1993 pp. 702-707

[3] Xie-Kanglin, J. Fu, "Determination of Membership Functions and Fuzzy Rule of Neural Network FLLC System", Journal of Shanghai Jiaotong Uni, **31(8)**, 1997, pp.28-33

[4] J. L. Castro, "How Many Rules are Necessary to Get Good Fuzzy Controller for a Control Problem?" Proc. of the 6th Int. Conf on Fuzzy Systems, **2**, 1997 pp.749-754

[5] D. P. Filev, R. R. Yager, "A Generalized Defuzzification Method via Bad Distributions", Int. J. of Intelligent System, **6(7)**, 1991 pp. 687-697

[6] D. P. Filev, R. R. Yager, "An Adaptive Approach to Defuzzification Based on Level Sets", Fuzzy Sets and Systems, **54(3)**, 1993, pp. 355-360

[7] R. R. Yager. D. P. Filev, "SLIDE: A Simple Adaptive Defuzzification Method", IEEE Trans. on Fuzzy Systems, **1(1)**, 1993, pp. 69-78

[8] R. R. Yager, D. P. Filev, "On the Issues of Defuzzification and Selection Based on a Fuzzy Sets", Fuzzy Sets and Systems, **55(3)**, 1993, pp. 255-272

[9] S. Mabuchi, "A Proposal for a Defuzzification Strategy by the Concept of Sensitivity Analysis", Fuzzy Sets and Systems, **55(1)**, 1993, pp. 1-14

[10] W. Pedrycz, "Fuzzy Control and Fuzzy Systems Research Studies", John Wiley and Sons, N.Y. 1989

2010 Reviewers

Béda, Péter
Bugár, Gyöngyi
Fehér, Gyula
Fodor, János
Goda, Tibor
Gottschalk, Klaus
Győri, Erzsébet
Harmati, István
Jánosi, László
Kádár, Péter
Katona, Tamás János
Kelemen, Jozef
Kiss, Jenő
Kovács, Roland
Kovács, Szilveszter
Kucsera, Péter
Lenkey-Bíró, Gyöngyvér
Maros, Dóra
Nádai, László
Nagy, Lóránt
Precup, Radu-Emil
Radeleczki, Sándor
Radosav, Dragica
Reskó, Barna
Ruszinkó, Endre
Schuster, György
Seller, Rudolf
Szabó, József
Szabó, Péter
Szakács, Tamás
Takács, Márta
Tar, József
Tuzson, Tibor
Vámossy, Zoltán
Varga, Lajos
Vas, László Mihály
Vásárhelyi, József